Graduate Course in Physics

University of Pisa

The School of Graduate Studies in Basic Sciences "Galileo Galilei"

Ph.D. Thesis

Radiation reaction effects in superintense laser-plasma interaction

Candidate
Matteo Tamburini

Supervisors
Dr. Andrea Macchi
Prof. Francesco Pegoraro

September 2011

Contents

Notation

In this paper, the following notations and conventions for common physical quantities are used: e is the electron's charge with its sign, m is the electron's mass unless otherwise specified, c is the speed of light, $\omega = 2\pi/T = 2\pi c/\lambda$ is the laser frequency (T is the laser period and λ is the laser wavelength), n is the electron numerical density, $\omega_p^2 = 4\pi n e^2/m$ is the plasma frequency, $\alpha = e^2/\hbar c \approx 1/137$ is the fine-structure constant, $r_e = e^2/mc^2 \approx 2.82 \times 10^{-13}\,\mathrm{cm}$ is the classical electron radius, $\lambda_C = \hbar/mc = r_e\alpha^{-1} \approx 3.86 \times 10^{-11}\,\mathrm{cm}$ is the Compton wavelength, $E_{Cr} = B_{Cr} = m^2c^3/\hbar|e| \approx 4.4 \times 10^{13}\,\mathrm{G} \approx 1.32 \times 10^{16}\,\mathrm{V\,cm^{-1}}$ is the critical field of quantum electrodynamics and $a_0 \equiv |e|E/m\omega c$ is the normalized laser amplitude where E is the peak of the laser field. In 'practical' units $a_0 \approx 8.5\times10^{-10}\lambda_{\mu\mathrm{m}}\sqrt{I_{\mathrm{W\,cm^{-2}}}}$ for a linearly polarized monochromatic plane wave and $a_0 \approx 6\times10^{-10}\lambda_{\mu\mathrm{m}}\sqrt{I_{\mathrm{W\,cm^{-2}}}}$ for a circularly polarized monochromatic plane wave.

Gaussian units or normalized units are used. When employing normalized units, time is in units of ω^{-1}, space is in units of $k^{-1} = c\omega^{-1}$, velocities in units of c, momenta in units of mc, fields in units of $mc\omega/|e|$ and densities in units of the critical density $n_c = m\omega^2/4\pi e^2 \approx 1.1 \times 10^{21}\,\lambda_{\mu\mathrm{m}}^{-2}\,\mathrm{cm^{-3}}$.

Greek tensorial indices indicate four-dimensional quantities $\mu = \{0, 1, 2, 3\}$, Latin tensorial indices indicate three-dimensional quantities $i = \{1, 2, 3\}$. The metric is $g_{\mu\nu} = (+, -, -, -)$ and the total antisymmetric tensor of the fourth-rank $\varepsilon^{\alpha\beta\gamma\delta}$ is defined such that $\varepsilon^{0123} = +1$ (therefore $\varepsilon_{0123} = -1$).

Introduction

The past twenty years have witnessed a six orders of magnitude increase in available laser intensity (Fig. 1). The record intensity of 2×10^{22} W cm^{-2} has been obtained [1] and intensities of the order of $10^{24} - 10^{26}$ W cm^{-2} are envisaged at the Extreme-Light-Infrastructure [2] (ELI).

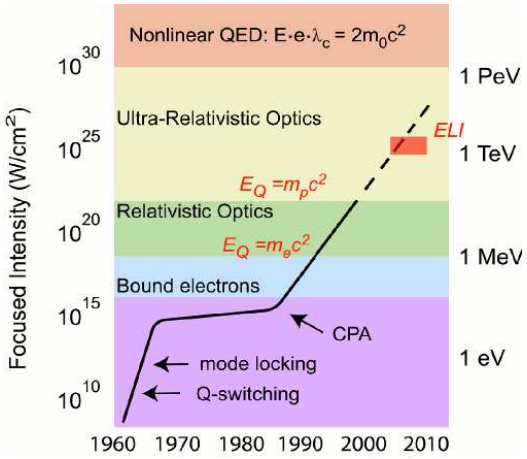

Figure 1: Sketch of the evolution of the maximum achievable laser intensity, from Ref. [2]. The expected scaling for the last decade turned out to be over-optimistic. The present record intensity is 2×10^{22} W cm^{-2} [1].

The great interest in laser-matter interaction at superintense laser intensities is justified both by their importance for fundamental physics, where new exotic regimes can be tested [4, 5], and by their applications ranging from new avenues for particle acceleration suitable e.g. for oncology treatment [6], medical imaging and fast ignition [3, 5] or for the reproduction on the laboratory scale of extreme processes typical of astrophysical plasmas [5, 9]. Enter-

ing the relativistic regime $I \gtrsim 10^{18}\,\mathrm{W\,cm^{-2}}$, several novel physical effects has been already observed such as relativistic self-focusing, high-harmonic generation [7] and acceleration of macroscopic quantities of electrons and ions [8]. Approaching the ultra-relativistic regime $I \gtrsim 10^{23}\,\mathrm{W\,cm^{-2}}$ as foreseen with the ELI project, many other exotic phenomena such as strong radiation reaction (RR) effects [10, 11, 18], copious electron-positron pair production [14] and nonlinear quantum electrodynamic (QED) effects are expected [2, 5].

Of special importance for a number of foreseen applications, ion acceleration driven by superintense laser pulses has attracted an increasing interest in the last decade [8]. The unique features of laser produced ion beams such as large number of accelerated ions, ultrashort duration, high brilliance and high collimation has generated enormous interest and stimulated both theoretical and experimental research on new promising ion acceleration regimes using different laser and plasma parameters [8]. In particular, a theoretical study by Esirkepov *et al.* [19] has shown that at ultra-high intensities ($I > 10^{23}\,\mathrm{W\,cm^{-2}}$ for 'optical' laser wavelengths $\lambda \sim \mu$m) the radiation pressure of a laser pulse can efficiently drive the acceleration of a thin foil[1] up to relativistic (GeV) energies. This new ion acceleration mechanism was named as the Radiation Pressure Dominated Acceleration (RPDA) (or "laser-piston") regime and its promising features such as its foreseen high efficiency[2], linear scaling with the laser intensity[3], and the quasi-monoenergetic features expected in the ion energy spectrum have stimulated a growing number of studies aimed to control such features and to improve the expected qualities of the generated beams [8]. In this thesis, we mainly focus our studies on the case of interaction of a superintense laser-pulse with a thin plasma slab in the RPDA regime.

[1]For a thin foil we mean that the foil thickness ℓ is smaller or comparable with the laser wavelength λ i.e. $\ell \lesssim \lambda$.

[2]The acceleration efficiency tends to 100% in the relativistic limit as the laser pulse and the thin foil become almost phase-locked and the intensity of the wave reflected by the thin foil tends to vanish with a significant transfer of momentum from the laser pulse to the foil.

[3]For instance, in the previously studied ion acceleration mechanism named Target Normal Sheath Acceleration (TNSA), the ion energy roughly scales with the square root of the laser intensity, see Ref. [8].

At the extremely high optical laser intensities needed for relativistic (GeV) ion production and radiation pressure dominance $I \gtrsim 10^{23}\,\mathrm{W\,cm^{-2}}$, the laser field performs a work hundreds of times larger than the electron rest energy mc^2 in a single laser period. Electrons therefore become ultra-relativistic within a fraction of the wave period experiencing superstrong accelerations and emitting large amounts of electromagnetic radiation. Such emission may affect the dynamics of the electron itself and, in the *classical framework*, can be conveniently described by the so called radiation reaction (RR) force. The RR force therefore describes the back-action of the radiation emitted by an accelerated electron on the motion of the electron itself and accounts for the loss of the electron energy and momentum due to the emission of such radiation. Some proposals have been put forward to test RR effects experimentally and are in principle possible with currently available laser technology [10, 17, 15]. For the first time, RR effects may play a dominant role in the electron dynamics providing an opportunity to test this old and controversial prediction of classical electrodynamics experimentally.

As discussed above, RR effects are expected to strongly affect the electron dynamics in next generation laser-matter interaction experiments at extreme intensities such as those foreseen with the ELI project. A comprehension of the features of the RR force and of its effects on the collective dynamics of a many-body system i.e. a plasma is therefore crucial to both test this important prediction of classical electrodynamics experimentally and above all to plan and design next generation laser-matter experiments. To this aim and in particular to unfold the strongly non-linear dynamics of a plasma where a *macroscopic* number of electrons and ions interact through their collective self-consistent fields, a statistical approach for the description of the system with RR effects included and large scale computer simulations are mandatory. In fact, the collective dynamics of a plasma is described by the coupled system of kinetic and Maxwell equations for the distribution function and the self-consistent mean fields and RR effects have therefore to be accounted including the RR force into a new 'generalized' coupled system of kinetic and Maxwell equations. This system of partial differential equations is strongly non-linear and a new numerical approach compatible with existing numerical schemes is needed to solve such equations efficiently

with large scale computer simulations which, at least for three-dimensional simulations, often require the use of thousands of processors and terabytes of memory to obtain reliable results.

A widely used approach suitable to efficiently simulate laser-plasma interactions with high-performance computer facilities has been developed in the past decades and was named as the particle-in-cell (PIC) approach [65]. In some sense the PIC approach reduces the laser-plasma simulation to the simplest possible model: Maxwell's equations plus Newton's equations for 'computational' particles (see Ref. [65] for details). One may think that PIC is the most straightforward and 'elementary' description of a plasma in terms of individual charged particles moving under the action of self-consistent electromagnetic fields. However, in almost any physical system of interest, the total number of electrons and ions exceeds by many orders of magnitude the number of 'computational' particles that can be included in a feasible simulation. The PIC approach therefore consists in assuming a discrete representation of the unknown statistical distribution function i.e. the distribution function is assumed to be a sum of large number of overlapping and spatially extended 'clouds' or 'computational' particles each representing a large number of the actual physical particles [65]. Once inserted this discrete representation of the distribution into the kinetic equations, the problem of solving the kinetic equation reduces to the problem of solving a set of 'equations of motion' for the computational particles which are formally identical to the usual Newton's equation of motion except that the force is averaged on the size of the computational particle (see appendix B.3). After introducing a suitable discretization of space and time i.e. an appropriate lattice, a numerical integrator (in jargon, a "pusher") that solves the finite difference approximation of Newton's and Maxwell's equations is used to advance computational particles and self-consistent fields respectively. The problem of including RR effects into the kinetic description of a plasma therefore reduces to develop a suitable pusher for the RR force that have to be compatible with well-tested existing numerical schemes such as the pusher for the Lorentz force.

The problem of finding a satisfactory equation of motion that accounts for RR effects has been a controversial and much disputed subject in clas-

sical electrodynamics from the beginning of the twentieth-century (see the review [28] and the recent books [29, 30]). This issue has grown in importance in light of recent progresses in the achievable laser intensity that makes possible to test it experimentally [10, 17, 15] and for its foreseen relevance in next generation laser-matter experiments [24, 11, 12, 13, 25, 27, 26]. Recently, literature has emerged that offers a satisfactory equation of motion with RR both from the physical [30, 31, 32] (see also Refs. [33, 34] for a different approach) and from the mathematical point of view (see Refs. [35, 29] and in particular the recent Ref. [36]). In the *classical framework*, the so called Landau-Lifshitz [37] (LL) equation describes the motion of an electron in the presence of an external electromagnetic field accounting for RR effects. Moreover, exact analytical solutions of the LL equation have been found for many important cases, from constant and uniform magnetic fields [29], Coulomb field [38], constant crossed fields [39], and for the motion in a plane wave of arbitrary shape and polarization [39]. It is therefore possible to test and validate proposed numerical approaches to the inclusion of the RR force into PIC codes with such exact solutions.

The main purpose of this thesis is to develop an understanding of RR effects in superintense laser-thin plasma foil interactions in the RPDA regime mainly by multi-dimensional PIC simulations. PIC simulations are used to investigate the basic physical processes, establish when RR effects become important and to identify the relevant parameters. To this aim, a simple suitable approximation of the LL force and a novel and efficient particle pusher for the LL force have been developed and tested comparing the numerical prediction with the analytical solution for the plane wave case. From the analytical side, the general properties of the fully relativistic kinetic equations of an optically thin plasmas including RR effects have been studied and it was shown that the RR force leads to a contraction of the available phase-space. The physical interpretation of this property is that the RR force acts as a cooling mechanism for the system: part of the energy, momentum and entropy are radiated away and the spread in both momentum and coordinate space may be reduced. This prediction is in agreement with the results of our multi-dimensional PIC simulations where we found that RR effects lead to both an increased bunching in space and to a noticeable cooling of

high-energy electrons.

In this thesis, we limit our study to the classical framework. The role of quantum effects and the conditions of validity of classical mechanics are briefly discussed. A final a posteriori check of the validity of the classical approach to RR effects has been performed in 1D PIC simulations. Similar trends have been observed in 2D and 3D simulations confirming that 1D results are reliable.

Chapter 1

Electron dynamics with radiation reaction

Since the beginning of the twentieth-century, a considerable amount of literature has been published on the equation of motion of a single particle subject to its own electromagnetic field [28, 29]. The purpose of this chapter is to review the recent attempts conducted to obtain a physically satisfactory and self-consistent equation of motion with RR effects and to briefly discuss the restrictions to a classical treatment due to the onset of quantum effects.

The basic problem when we deal with self-fields of elementary particles is that classical electrodynamics becomes patently insubstantial at the point limit (more precisely, at sizes below 2/3 the classical electron radius $r_e \equiv e^2/mc^2 \approx 2.82\times10^{-13}$ cm [48, 52]). In fact, classical electrodynamics ceases to be valid at sizes of the order of the Compton wavelength $\lambda_C \equiv \hbar/mc \approx 3.86\times 10^{-11}$ cm where QED effects such as creation of electron-positron pairs yield an effective extended charge distribution. Many typical problems of classical electrodynamics of point particles disappear in the quantum framework as shown in Ref. [52] where the *quantum* point particle has been studied.

The problem of RR has been rigorously addressed in the classical framework by Gralla et al. in Ref. [36] and we briefly summarize their arguments here after a rapid survey of other results with a particular emphasis on the Landau-Lifshitz argument which has been made mathematically rigorous by Spohn using geometric perturbation theory [35].

1.1 The equation(s) of motion with RR

In classical electrodynamics, Maxwell's equations

$$\partial_\beta F_{\mu\nu} + \partial_\mu F_{\nu\beta} + \partial_\nu F_{\beta\mu} = 0 \tag{1.1}$$

$$\partial_\alpha F^{\alpha\mu} = \frac{4\pi}{c} j^\mu \tag{1.2}$$

have a well-posed initial value formulation provided that the charge current source j^μ is a specified function of the space-time coordinates $x^\mu = (ct, \mathbf{x})$ which satisfies the local conservation law

$$\partial_\mu j^\mu = 0 \tag{1.3}$$

In particular, solutions to Maxwell's equations exist for an arbitrary point particle source

$$j^\mu = e u^\mu c\, \delta^3(\mathbf{x} - \mathbf{r}(t)) \frac{d\tau}{dt} \tag{1.4}$$

where $u^\mu = (\gamma, \gamma\mathbf{v}/c)$ is the four-velocity and τ is the proper time, provided only that the worldline is timelike and that e is constant along the worldline.

The complementary problem of the motion of a point particle in a given external field $F^{\mu\nu}$ by the Lorentz force equation

$$mc\frac{du^\mu}{d\tau} = eF^{\mu\nu}u_\nu \tag{1.5}$$

has also a well-posed initial value formulation being a system of second-order ordinary differential equation that admits a unique solution for any $F^{\mu\nu}$. However, it is easily seen that the coupled system of equations (1.1), (1.2) and (1.4) together with the equation of motion

$$mc\frac{du_\mu}{d\tau} = eF^T_{\mu\nu}u^\nu \tag{1.6}$$

where $F^T_{\mu\nu}$ is the *full* electromagnetic field i.e. the sum of the external fields and of the particle's self-fields, do not make neither physical nor mathematical sense. From the physical point of view, both energy and momentum diverges and we have to proceed formally by introducing a renormalized mass that makes the observable mass a finite quantity.

In classical electrodynamics, matter must be modeled as a continuum and self-interactions depend on the internal composition, internal forces[1], structure and initial state of the body. These difficulties are usually avoided assuming a rigid charge distribution in the instantaneous rest frame. This approximation is consistent if the variation of the velocity, in the time it takes a light ray to cross the diameter of the particle's charge distribution, is much smaller than c in the instantaneous rest frame. In general, this extended rigid charge models lead to a self-force that is expressed as an infinite series [53] that cannot be summed except for the case of a spherical charged shell [48]. It has been shown that the self-force for this extended charge distributions does not lead neither to self-acceleration nor to preacceleration solutions provided that the radius r of the charge distribution in the instantaneous rest frame is larger than $2/3$ the classical electron radius r_e [51, 52]. It may be worth noticing that the point particle limit of the expectation value of the *quantum* mechanical equations provides an equation of motion that is formally equivalent to the equation of motion of a classical charge distribution with an effective size of the order of the Compton wavelength $\lambda_C \sim 137 r_e$ and is therefore free of the drawbacks of the Lorentz-Abraham-Dirac (LAD) equation [52] (see below for details). From the physical point of view, this picture is a rather natural result as we expect that QED effects strongly modify the classical picture of a point particle when we probe distances below the Compton wavelength.

Returning to our original aim of getting a physically well-founded and self-consistent equation of motion for a classical charged particle, from a fundamental point of view the previous results provide a quite satisfactory answer. We may think that we just need to couple the Maxwell's equation with an extended charge distribution choosing a radius of the order of the Compton wavelength. However, it is at least unpractical and almost in every physical situation impossible to have a full control of physical quantities such as position and time from the laboratory scale deep into the Compton scale. Furthermore, we want to derive universal properties of the motion of small bodies that do not depend upon the details of any particular matter model. When all the distances involved are large compared to the radius

[1] In order to avoid the stability problem, see Ref. [53].

r of a charged distribution, the result ought to be independent of r. The usual approach is therefore to take a limit to zero size of the extended charge distribution at fixed charge and mass. This approach leads to the LAD equation [53, 37, 30, 48]

$$\frac{du^\beta}{d\tau} = \frac{e}{mc}F^{\beta\alpha}u_\alpha + \frac{2e^2}{3mc^3}\left(\frac{d^2u^\beta}{d\tau^2} + \frac{du_\alpha}{d\tau}\frac{du^\alpha}{d\tau}u^\beta\right) \tag{1.7}$$

with its associated difficulties. In fact, the LAD equation (1.7) is a third-order differential equation and has well known serious drawbacks such as preacceleration and runaway solutions [53, 37].

Landau and Lifshitz pointed out [37] that the inequality

$$\tau_0\frac{d}{d\tau} \ll 1 \tag{1.8}$$

where $\tau_0 \equiv 2e^2/3mc^3 = 2r_e/3c \approx 6.27\times10^{-24}\,\mathrm{s}$ is strictly satisfied in the classical framework. The inequality (1.8) implies that all the relative changes of physical quantities must be small on a time scale of order τ_0 in the *instantaneous rest frame* of the electron. This is a basic restriction for the dynamics of a classical charged particle because quantum effects become important on scales of the order of $\lambda_C/c \approx 1.29\times10^{-21}\,\mathrm{s}$. In the classical framework, the problem of what happens outside the boundaries of (1.8) is physically meaningless and also the possible presence of physically absurd solutions [63, 64] when (1.8) is violated do not question the validity of a *classical* equation of motion.

As a consequence of (1.8), the Lorentz force $\mathbf{f}_L = e\mathbf{E} + e(\mathbf{v}/c\times\mathbf{B})$ must satisfy the inequality

$$\left|\tau_0\frac{d}{dt}\mathbf{f}_L\right| \ll |\mathbf{f}_L| \tag{1.9}$$

in the instantaneous rest frame of the electron or, with the same accuracy (see Ref. [37])

$$\tau_0\left|e\dot{\mathbf{E}} + \frac{e^2}{mc}\mathbf{E}\times\mathbf{B}\right| \ll |e\mathbf{E}| \tag{1.10}$$

For the fields, (1.10) implies that the wavelength of the incident or emitted radiation λ must satisfy $\lambda \gg c\tau_0 \approx 1.88\times10^{-13}\,\mathrm{cm}$ and the strength of the

fields must satisfy $|\mathbf{B}| \ll 3m^2c^4/2|e|^3 \approx 9 \times 10^{15}\,\mathrm{G}$ in the instantaneous rest frame of the electron[2].

It is convenient to recast the restriction (1.9) in a manifestly Lorentz-invariant form replacing τ_0 with $\lambda_C/c = \hbar/mc^2$ in order to account for the stronger bounds from QED effects. Introducing the projector on the four-velocity $P^{\mu\nu} = g^{\mu\nu} - u^\mu u^\nu$ and the four-dimensional Lorentz force f_L^μ, then we have[3]

$$\frac{\lambda_C^2}{c^2}\left|P^\mu{}_\alpha \frac{df_L^\alpha}{d\tau} P_{\mu\beta} \frac{df_L^\beta}{d\tau}\right| \ll |f_L^\mu f_L^\nu g_{\mu\nu}| \tag{1.11}$$

The restriction (1.8) allows to perform a perturbative reduction of order of the LAD equation, i.e. the zero order equation

$$\frac{du^\beta}{d\tau} = \frac{e}{mc} F^{\beta\alpha} u_\alpha + \mathcal{O}\left(\tau_0 \frac{d}{dt}\right) \tag{1.12}$$

is used to estimate $du^\beta/d\tau$ and $d^2u^\beta/d\tau^2$ in the right hand side of the LAD equation (1.7) leading to the Landau-Lifshitz (LL) equation [37]

$$\frac{du^\mu}{d\tau} = \frac{e}{mc} F^{\mu\nu} u_\nu + \frac{2e^3}{3m^2c^3} \partial_\alpha F^{\mu\nu} u_\nu u^\alpha + \frac{2e^4}{3m^3c^5}\left(F^{\mu\nu} F_{\nu\alpha} u^\alpha + (F^{\nu\beta} u_\beta F_{\nu\alpha} u^\alpha) u^\mu\right) \tag{1.13}$$

The LL equation has a standard second-order initial value formulation and it is free from the preacceleration and runaway solutions that plague the LAD equation. Moreover, it differs from the LAD equation by terms of order $\mathcal{O}\left(\tau_0^2\, d^2/dt^2\right)$ which are insignificant in the classical domain.

The LL approach has been made mathematically rigorous by Spohn [35, 29] who derived the LL equation from the LAD equation through geometric perturbation theory. Spohn proved that the physical solutions[4] of the LAD equation lie on a critical surface which is repelling, i.e. any slight deviation from it is amplified and as a result the solution runs away. Moreover,

[2]The actual bounds from QED are $\lambda \gg \hbar/mc \approx 3.86 \times 10^{-11}\,\mathrm{cm}$ and $|\mathbf{B}| \ll m^2c^3/\hbar|e| \approx 4.4 \times 10^{13}\,\mathrm{G}$.

[3]The four-velocity is $u^\mu = (\gamma, \gamma\mathbf{v}/c)$ where $\gamma = 1/\sqrt{1 - \mathbf{v}^2/c^2}$ is the relativistic factor, $f_L^\mu = (\gamma \mathbf{f}_L \cdot \mathbf{v}/c, \gamma \mathbf{f}_L)$ is the four-dimensional Lorentz force and $\mathbf{f}_L = e(\mathbf{E} + \mathbf{v}/c \times \mathbf{B})$ is the three-dimensional Lorentz force.

[4]The Dirac's asymptotic condition $\lim_{t\to\infty} \dot{\mathbf{v}}(t) = 0$ is used to identify the critical manifold of the physical solutions of the LAD equation.

the physical solutions lying on the critical surface can be singled out by an effective second-order equation which is exactly the LL equation.

Recently, the issue of particle motion including self-fields has been addressed in a new and rigorous way by Gralla et al. in Ref.[36]. In short, they start arguing that the attempt to couple classical Maxwell's equations (1.1) and (1.2) together with point particle sources (1.4) and the Lorentz equation of motion (1.6) fails on both mathematical and physical grounds. Thus, they remove from any fundamental status both the point charge source (1.4) and the Lorentz force equation (1.6) and assume only the existence of a matter stress-energy tensor $T^M_{\mu\nu}$ which couples to the electromagnetic field via conservation of the total stress-energy tensor

$$\partial^\nu \left(T^M_{\mu\nu} + T^{EM}_{\mu\nu}\right) = 0 \tag{1.14}$$

where the electromagnetic stress-energy tensor $T^{EM}_{\mu\nu}$ is

$$T^{EM}_{\mu\nu} = \frac{1}{4\pi}\left(-F_{\mu\alpha}F_{\nu}{}^{\alpha} + \frac{1}{4}g_{\mu\nu}F_{\alpha\beta}F^{\alpha\beta}\right) \tag{1.15}$$

The coupled system of Maxwell's equations (1.1) and (1.2) together with the conservation law (1.14) is assumed as the fundamental description of all realistic bodies composed of continuum matter thus every result must be derived from these equations solely. In their approach, the charge distribution is *not* assumed to be rigid in the instantaneous rest frame. In order to obtain a simple and universal description of the motion of small bodies, they considered a modified point particle limit where not only the size of the body goes to zero but its charge e and mass m also go to zero while their ratio e/m is fixed. Using this modified limit they found *no divergent* physical quantities. In their approach, the Lorentz force equation emerges as a lowest order description of the bulk motion of a small but extended body whereas self-force effects (i.e. RR effects) as well as the dipole force and spin force effects arise as a first-order correction to the motion of the body. As a result of their derivation, they got the LL equation (1.13) as the correct approximation of the equation of motion with RR for a particle with negligible magnetic and electric dipole momentum.

For completeness, we mention that several other possible equation of motion with RR effects have been proposed, which have been derived in very

different ways but lead to nearly the same results within the boundaries of classical mechanics. Among these, the most popular are the Eliezer [62] or Ford-O'Connell [33, 34] equation and the Sokolov [20] equation.

The Eliezer or Ford-O'Connell equation is

$$\frac{du^\mu}{d\tau} = \frac{e}{mc}F^{\mu\nu}u_\nu + \frac{e\tau_0}{m}\partial_\alpha F^{\mu\nu}u_\nu u^\alpha + \frac{e\tau_0}{mc}\left(F^{\mu\nu}\frac{du_\nu}{d\tau} + (F^{\nu\alpha}u_\alpha\frac{du_\nu}{d\tau})u^\mu\right) \quad (1.16)$$

This equation can be obtained substituting in the right hand side of the LAD equation (1.7) the estimate (1.12) only once and it therefore differs from the LAD and LL equations for terms of the order $\mathcal{O}\left(\tau_0^2\, d^2/dt^2\right)$. As pointed out by Ford and O'Connell, who derived Eq.(1.16) with an approach based on the use of the generalized quantum Langevin equation [33], this equation does not lead to either runaway solutions or acausal behavior.

Recently, Sokolov *et al.* proposed a different couple of classical equations of motion that are derived phenomenologically [20]. The phenomenological equations proposed by Sokolov *et al.* are (see Eqs. (6, 7) in Ref. [20])

$$\frac{d\mathcal{P}^\mu}{ds} = \frac{e}{c}F^{\mu\nu}\frac{dx_\nu}{ds} - \frac{I\mathcal{P}^\mu}{mc^2} \quad (1.17)$$

$$\frac{dx^\mu}{ds} = \frac{\mathcal{P}^\mu}{m} + \tau_0\frac{I}{I_E}\frac{eF^{\mu\nu}\mathcal{P}_\nu}{m^2c} \quad (1.18)$$

where $\mathcal{P}^\mu$ is a generalized momentum[5], s is the time in the "momentarily comoving Lorentz frame (MCLF) such that the spatial components of $\mathcal{P}^\mu$ vanish"[6], I is the "total emission intensity" and I_E is the "dipole emission intensity" (see Ref. [20]). In Ref. [20], it is suggested that I can be chosen phenomenologically i.e. I "can be a random function with its average equal to I_E in order to trace the quantum theory limit or to include emission with large photon energy" (see Ref. [20] for details). Anyway, at least for the single electron dynamics in the classical framework, the value $I = I_E$ should be chosen. In this latter case, the system of equations (1.17, 1.18) differs from the LL equation for small terms. In section 1.2, it is shown that the LL

[5]This generalized momentum is *not* collinear with the four-velocity $u^\mu = c^{-1}dx^\mu/d\tau$.

[6]In general, since $\mathcal{P}^\mu$ is *not* proportional to the four-velocity u^μ, the time in the MCLF s is *not* the proper time τ i.e. it is *not* the time measured in the instantaneous rest frame of the electron where the spatial components of u^μ vanish.

equation (1.13) and the Sokolov equation (with $I = I_E$ in Eqs. (1.17, 1.18)) have nearly the same leading term even for fields well beyond the classical framework such as $|\mathbf{E}|, |\mathbf{B}| \sim m^2c^3/\hbar|e|$.

Substituting Eq. (1.18) in Eq. (1.17) we get the momentum equation for an electron[7]

$$\frac{d\mathcal{P}^\mu}{ds} = \frac{e}{mc}F^{\mu\nu}\mathcal{P}_\nu + \frac{\tau_0 e^2}{m^2c^2}\frac{I}{I_E}F^{\mu\nu}F_{\nu\alpha}\mathcal{P}^\alpha - \frac{I\mathcal{P}^\mu}{mc^2} \tag{1.19}$$

and multiplying Eq. (1.19) for $\mathcal{P}_\mu$ and recalling that

$$I_E = \frac{\tau_0 e^2}{m^3c^2}\left(\mathcal{P}_\nu F^{\nu\mu}F_{\mu\alpha}\mathcal{P}^\alpha\right) \tag{1.20}$$

we get

$$\mathcal{P}_\mu\frac{d\mathcal{P}^\mu}{ds} = mI\left(1 - \frac{\mathcal{P}_\mu\mathcal{P}^\mu}{m^2c^2}\right). \tag{1.21}$$

When the electron is free (i.e. $F^{\nu\mu} = 0$) from Eqs. (1.17, 1.18)) we have $\mathcal{P}_\mu\mathcal{P}^\mu = m^2c^2$, then from Eq. (1.21) we get that the condition $\mathcal{P}_\mu\mathcal{P}^\mu = m^2c^2$ is preserved. We mention that while the LL equation (1.13) preserves the on-shell condition on the four velocity $u^\mu u_\mu = 1$, the Sokolov equations (1.17, 1.18)) preserve the condition on the generalized momentum $\mathcal{P}_\mu\mathcal{P}^\mu = m^2c^2$ (see also the discussion in section 4 on page 4 of Ref. [21]).

Finally, we point out that the condition $u_\mu du^\mu/d\tau = 0$ is identically fulfilled by the LL equation (1.13) while from Eq. (1.21) we get that the condition $\mathcal{P}_\mu d\mathcal{P}^\mu/ds = 0$ is fulfilled only when $\mathcal{P}_\mu\mathcal{P}^\mu = m^2c^2$. In a computer simulation of a laser pulse interacting with a plasma such as those performed using the particle-in-cell (PIC) method, numerical effects may lead to small deviations from $\mathcal{P}_\mu\mathcal{P}^\mu = m^2c^2$. Since from Eq. (1.21) $\mathcal{P}_\mu d\mathcal{P}^\mu/ds \neq 0$ if $\mathcal{P}_\mu\mathcal{P}^\mu \neq m^2c^2$ then a small deviation due to numerical effects may be enlarged during the simulation.

1.2 The physical picture

In order to investigate the physical properties of the RR force as well as to determine the relative importance of each term and to develop possible

[7] Compare with Eq.(5) in Ref. [20].

suitable approximations, it is useful to consider the components of the four-dimensional LL equation (1.13). From the temporal component of the four-dimensional LL equation we get the rate of change of the electron's energy

$$\frac{d\gamma}{dt} = \frac{e}{mc^2}\left(\mathbf{v}\cdot\mathbf{E}\right) + \frac{2e^3}{3m^2c^4}\gamma\left[\frac{\partial\mathbf{E}}{\partial t} + (\mathbf{v}\cdot\nabla)\mathbf{E}\right]\cdot\frac{\mathbf{v}}{c} + \\ + \frac{2e^4}{3m^3c^5}\left[\left(\mathbf{E}+\frac{\mathbf{v}}{c}\times\mathbf{B}\right)\cdot\mathbf{E} - \gamma^2\left[\left(\mathbf{E}+\frac{\mathbf{v}}{c}\times\mathbf{B}\right)^2 - \left(\frac{\mathbf{v}}{c}\cdot\mathbf{E}\right)^2\right]\right] \tag{1.22}$$

while from the spatial components we get the three-dimensional form of the LL equation

$$\frac{d\mathbf{p}}{dt} = e\Big(\mathbf{E}+\frac{\mathbf{v}}{c}\times\mathbf{B}\Big) + \frac{2e^3}{3mc^3}\gamma\Big[\Big(\frac{\partial}{\partial t}+\mathbf{v}\cdot\nabla\Big)\mathbf{E} + \frac{\mathbf{v}}{c}\times\Big(\frac{\partial}{\partial t}+\mathbf{v}\cdot\nabla\Big)\mathbf{B}\Big] \\ + \frac{2e^4}{3m^2c^4}\Big\{\Big(\mathbf{E}+\frac{\mathbf{v}}{c}\times\mathbf{B}\Big)\times\mathbf{B} + \Big(\frac{\mathbf{v}}{c}\cdot\mathbf{E}\Big)\mathbf{E} \\ - \gamma^2\Big[\Big(\mathbf{E}+\frac{\mathbf{v}}{c}\times\mathbf{B}\Big)^2 - \Big(\frac{\mathbf{v}}{c}\cdot\mathbf{E}\Big)^2\Big]\frac{\mathbf{v}}{c}\Big\} \tag{1.23}$$

where $\mathbf{v} = d\mathbf{x}/dt$ is the three-dimensional velocity, $\mathbf{p} = \gamma m\mathbf{v}$ is electron's momentum and $\gamma = \sqrt{1+\mathbf{p}^2/m^2c^2}$ is the relativistic factor.

Since in the following we mostly refer to the case of interaction with a quasi-monochromatic wave i.e. a laser pulse, in order to highlight the relevant scales as well as to include the RR force in a numerical code, it is useful to employ dimensionless quantities by normalizing time in units of ω^{-1}, space in units of $c\omega^{-1}$, momenta in units of mc and fields in units of $m\omega c/|e|$ where $\omega = 2\pi c/\lambda$ is the laser frequency and λ is the laser wavelength. Then, Eq. (1.23) becomes

$$\frac{d\mathbf{p}}{dt} = -\left(\mathbf{E}+\mathbf{v}\times\mathbf{B}\right) - \left(\frac{4\pi r_e}{3\lambda}\right)\Big\{\gamma\Big[\left(\frac{\partial}{\partial t}+\mathbf{v}\cdot\nabla\right)\mathbf{E} \\ + \mathbf{v}\times\left(\frac{\partial}{\partial t}+\mathbf{v}\cdot\nabla\right)\mathbf{B}\Big] - \left[\left(\mathbf{E}+\mathbf{v}\times\mathbf{B}\right)\times\mathbf{B} + \left(\mathbf{v}\cdot\mathbf{E}\right)\mathbf{E}\right] \\ + \gamma^2\left[\left(\mathbf{E}+\mathbf{v}\times\mathbf{B}\right)^2 - \left(\mathbf{v}\cdot\mathbf{E}\right)^2\right]\mathbf{v}\Big\} \tag{1.24}$$

The LL equation (1.24) is strongly non-linear both in the fields and in the electron momentum. In general, the importance of RR effects on the electron

motion depends on the strength and geometry of the electromagnetic fields, as well as on the electron energy, which is a function of the amplitude and frequency of the field itself. In a plasma with many relativistic electrons which are subject both to the laser field and to the self-generated fields, it is very difficult to asses a priori the relevance of RR effects; however one would need to estimate at least the scaling of RR effects with the laser pulse parameters. From Eq. (1.24) we find that the strength of the RR force depends on the ratio of the 'effective' electron radius $4\pi r_e/3$ by the laser wavelength λ. For a typical laser wavelength $\lambda \sim 0.8\,\mu$m and therefore $4\pi r_e/3\lambda \approx 1.47 \times 10^{-8}$. This implies that RR effects are significant, i.e. the RR force is comparable with the Lorentz force, only when ultrarelativistic electrons $\gamma \gg 1$ move inside superintense fields $\sqrt{(\mathbf{E}^2+\mathbf{B}^2)/2} \gg 1$ (normalized units).

It is useful to consider the qualitative properties of the RR force in the special case of electron motion in a plane wave. For this problem, the LL equation has an exact analytical solution for arbitrary pulse shape and polarization of the plane wave [39] and is considered in detail in section 2.2. Hence, the plane wave case may provide a useful benchmark and reference for RR effects in superstrong laser fields and, in the following discussion, we mostly refer to a plane wave. In a many-particle system such as a high-density plasma, the collective fields are generally much more complicated but the plane wave results may still provide some guidance for their interpretation.

When an ultrarelativistic electron is moving into a strong laser pulse and is *not* co-propagating with the pulse itself (when co-propagating the RR force tends to vanish, see below for details), the last term of the RR force in Eq. (1.24) (proportional to γ^2) is approximately γ^2 larger than the preceding one and is approximately $\gamma\sqrt{(\mathbf{E}^2+\mathbf{B}^2)/2}$ larger than the term containing the *derivatives* of the fields. This suggests that the effect of the RR force is almost completely determined by the last term of Eq. (1.24) while the smaller terms may often be neglected. Moreover, at least for the case of a plane wave, it is possible to show (see Ref. [11] and section 1.2.1) that the force related to the electron spin is about 137γ larger than the term of Eq. (1.24) containing the derivatives of the fields. This 'derivative' term in Eq.(1.24) must therefore be neglected as effects of the order or smaller than quantum effects are neglected. It is therefore possible to consider a reduced

LL equation

$$\frac{d\mathbf{p}}{dt} = -\left(\mathbf{E} + \mathbf{v}\times\mathbf{B}\right) + \left(\frac{4\pi r_e}{3\lambda}\right)\Big\{\left[\left(\mathbf{E} + \mathbf{v}\times\mathbf{B}\right)\times\mathbf{B} + \left(\mathbf{v}\cdot\mathbf{E}\right)\mathbf{E}\right] - \gamma^2\left[\left(\mathbf{E} + \mathbf{v}\times\mathbf{B}\right)^2 - \left(\mathbf{v}\cdot\mathbf{E}\right)^2\right]\mathbf{v}\Big\} \tag{1.25}$$

where the term containing the derivatives has been removed. The smallness of the contribution of the removed term was confirmed up to optical laser intensities of the order of $I \sim 10^{24}\,\mathrm{W\,cm^{-2}}$ comparing the results of one-electron simulations in a plane wave with versus without this term using a fourth-order Runge-Kutta method. In our PIC simulations, the reduced LL equation (1.25) was always used instead of the full LL equation (1.24).

We point out that even though the term in Eq.(1.25) that is proportional to γ^2 is typically much larger than the previous one, which is often of the same order of magnitude of the neglected 'derivative' term, both terms in Eq.(1.25) are essential to preserve the on-shell condition[8] $u_\mu u^\mu = 1$. In fact, the term proportional to γ^2 is zero in the instantaneous rest frame. However, from a practical point of view, PIC simulations with the RR force included are performed in the laboratory frame, i.e. the frame where the plasma target is initially at rest. It is therefore possibly instructive to neglect for a moment the smaller term and write down an 'effective' reduced LL equation in the *laboratory frame*

$$\frac{d\mathbf{p}}{dt} = \mathbf{f}_L - d\,\mathbf{v} \tag{1.26}$$

where $\mathbf{f}_L = -\left(\mathbf{E} + \mathbf{v}\times\mathbf{B}\right)$ is the Lorentz force and d is

$$\begin{aligned} d &\equiv \left(\frac{4\pi r_e}{3\lambda}\right)\gamma^2\left[\left(\mathbf{E} + \mathbf{v}\times\mathbf{B}\right)^2 - \left(\mathbf{v}\cdot\mathbf{E}\right)^2\right] \\ &= \left(\frac{4\pi r_e}{3\lambda}\right)\gamma^2\left[\mathbf{E}^2 - \left(\mathbf{v}\cdot\mathbf{E}\right)^2 + \mathbf{v}^2\mathbf{B}^2 - \left(\mathbf{v}\cdot\mathbf{B}\right)^2 - 2\mathbf{v}\cdot\left(\mathbf{E}\times\mathbf{B}\right)\right] \end{aligned} \tag{1.27}$$

It is straightforward to show that d is always non-negative as Eq.(1.27) can be rewritten as

$$d = \left(\frac{4\pi r_e}{3\lambda}\right)\gamma^2\left[\mathbf{f}_L^2 - \left(\mathbf{v}\cdot\mathbf{f}_L\right)^2\right] = \left(\frac{4\pi r_e}{3\lambda}\right)\gamma^2\mathbf{f}_L^2\left(1 - \mathbf{v}^2\cos^2(\theta)\right) \geq 0 \tag{1.28}$$

[8] This is immediately clear looking at the four-dimensional expression of the LL force Eq. (1.13). On the contrary, the derivative terms can be safely neglected.

where $1 > |\mathbf{v}| \geq 0$ and θ is the angle between $\mathbf{v}$ and $\mathbf{f}_L$.

In equation (1.26), RR effects appear as a 'friction' force with a nonlinear and anisotropic friction coefficient given by d. When an electron moves in an electromagnetic field, it feels a viscous force opposite to its velocity. Since the RR force in the laboratory frame is mainly a 'friction' force, in simple cases it is possible to estimate when RR effects become important with the dominant friction term of Eq. (1.22) evaluating the energy losses in the characteristic time scale of the system e.g. the cyclotron period or the laser period [10].

In the laboratory frame and for an ultra-relativistic electron, the friction coefficient d may be used as a measure of the strength of the RR force in units of $m\omega c$. In the case of electron motion in a plane wave, d may be compared directly with the normalized wave amplitude a_0 ($a_0 = |e|E/m\omega c$ in Gaussian units, where E is the peak value of the electric field). Setting $\mathbf{E}\times\mathbf{B}$ along the positive x-axis, the RR force is large for transverse motion ($d \to (\frac{4\pi r_e}{3\lambda})\gamma^2 a_0^2$ when $v_y^2 + v_z^2 \to 1$), tends to vanish ($d \to 0$) when the electron co-propagates with the wave ($v_x \to 1$) and has its maximum value ($d \to (\frac{4\pi r_e}{3\lambda})\gamma^2 4a_0^2$) when the electron counter-propagates with the wave ($v_x \to -1$). In the interaction of a laser-pulse with a solid-density plasma, the dynamics of the particles as well as the dynamics of the fields are much more complicated and the local value of $d(\mathbf{x}, \mathbf{p}, \mathbf{E}, \mathbf{B})$ must be obtained from the simulation data. In fact, as a result of our PIC simulations (see Ref. [11] and chapter 5), we found that the value of d can change by *four orders of magnitude* just changing the laser polarization with the other parameters fixed.

The friction effect of the RR force physically corresponds to the single particle 'incoherent' emission of high-frequency radiation by ultra-relativistic electrons. When the RR force is included in the numerical simulation of a collisionless, relativistic plasma, it is typically not feasible to resolve electromagnetic waves at such high frequencies, much larger than the inverse of the temporal resolution. Thus, it is assumed that such radiation escapes from the system without re-interacting with other electrons. Note that even a solid-density plasma is transparent to such radiation, since in the RPA regime ($a_0 \gtrsim 300$) the RR effect is mostly due to the emission of radiation with photon energies in the MeV range, while the plasma frequency corresponds to at most a few hundreds of eV. In fact, for a plane wave with $a_0 \gg 1$,

the instantaneous emission spectrum is approximately synchrotron-like and therefore the main part of the emitted radiation is concentrated in the region of frequencies $\omega_e \sim \gamma^2 |e|E/mc = \gamma^2 a_0\,\omega$ while the plasma frequency is $\omega_p = \sqrt{n/n_c}\,\omega$ and the ratio $\omega_e/\omega_p = \gamma^2 a_0 \sqrt{n_c/n}$ is typically of the order of $\sim 10^5$ for solid-density targets ($n \sim 100\, n_c$) and superintense pulses ($a_0 \sim 300$). From the point of view of the energy balance of the system, the energy radiated at high frequencies appears as a loss term or 'dissipation'. In our PIC simulations, the percentage of radiative loss is measured by comparing the energy balance of the same simulation[9] with versus without RR.

Finally, we compare the three-dimensional LL equation (1.23) with the three-dimensional Sokolov equation (see Eqs. (12, 13) in Ref. [20])

$$\begin{aligned} \frac{d\mathbf{p}}{dt} &= \mathbf{f}_L + \frac{e}{c}[\delta\mathbf{u} \times \mathbf{B}] - \frac{\mathbf{u}\gamma^2}{c^2}(\delta\mathbf{u} \cdot \mathbf{f}_L) \\ \frac{d\mathbf{x}}{dt} &= \mathbf{u} + \delta\mathbf{u} \end{aligned} \tag{1.29}$$

where

$$\mathbf{u} = \frac{\mathbf{p}}{\sqrt{m^2 + \mathbf{p}^2/c^2}}, \qquad \mathbf{f}_L = e\mathbf{E} + \frac{e}{c}[\mathbf{u} \times \mathbf{B}] \tag{1.30}$$

and

$$\delta\mathbf{u} = \frac{\tau_0}{m} \frac{\mathbf{f}_L - \mathbf{u}(\mathbf{u} \cdot \mathbf{f}_L)/c^2}{1 + \tau_0(\mathbf{u} \cdot \mathbf{f}_L)/(mc^2)} \tag{1.31}$$

Eq.(1.29) differs from the LL equation (1.23) for terms that are small even for QED fields $|\mathbf{E}|, |\mathbf{B}| \sim m^2c^3/\hbar|e|$. In fact, $\tau_0(\mathbf{u} \cdot \mathbf{f}_L)/(mc^2) \leq \tau_0|e||\mathbf{E}|/mc$ and for $|\mathbf{E}| = m^2c^3/\hbar|e|$ we have $\tau_0|e||\mathbf{E}|/mc = 2e^2/3\hbar c \sim 1/205$ and therefore $\delta\mathbf{u} \ll \mathbf{u}$ for a relativistic electron[10]. Hence, Eq.(1.29) reduces to

$$\begin{aligned} \frac{d\mathbf{p}}{dt} &\simeq \mathbf{f}_L + \frac{e\tau_0}{mc}[\mathbf{f}_L \times \mathbf{B} - (\mathbf{u} \cdot \mathbf{f}_L)(\mathbf{u} \times \mathbf{B})/c^2] - \frac{\tau_0\gamma^2}{mc^2}(\mathbf{f}_L^2 - (\mathbf{u} \cdot \mathbf{f}_L)^2/c^2)\mathbf{u} \\ \frac{d\mathbf{x}}{dt} &\simeq \mathbf{u} \end{aligned} \tag{1.32}$$

[9] In a PIC code, the total energy of fields and particles is conserved within the limits of numerical accuracy, typically within 1% in our 1D PIC simulations.

[10] This is not an actual restriction as RR effects are negligible for non-relativistic electrons and, for QED strong fields, an electron initially at rest becomes relativistic in a Compton time $\lambda_C/c \approx 1.29 \times 10^{-21}$ s.

while the reduced LL equation (1.25) is (using the same notation of Eq.1.32)

$$\frac{d\mathbf{p}}{dt} = \mathbf{f}_L + \frac{e\tau_0}{mc}[\mathbf{f}_L \times \mathbf{B} + (\mathbf{u}\cdot\mathbf{f}_L)\mathbf{E}/c] - \frac{\tau_0\gamma^2}{mc^2}(\mathbf{f}_L^2 - (\mathbf{u}\cdot\mathbf{f}_L)^2/c^2)\mathbf{u}$$
$$\frac{d\mathbf{x}}{dt} = \mathbf{u} \tag{1.33}$$

Eq.(1.32) and Eq.(1.33) have the same leading friction-like term and they differ for terms that are smaller than quantum effects.

1.2.1 The RR force versus the spin force

In this section we compare the order of magnitude of the RR force Eq. (1.13) and of the force due to the magnetic dipole associated with the electron spin.

The correct relativistic generalization of the spin force for an electron has been discussed in Ref. [16] (see also Ref. [36] for a different derivation) and its expression is

$$g^\mu = -\frac{1}{2}Q^{\gamma\delta}\partial^\mu F_{\gamma\delta} + \frac{1}{2}\left(Q^{\gamma\delta}\partial_\alpha F_{\gamma\delta}u^\alpha\right)u^\mu \tag{1.34}$$

where $Q^{\gamma\delta} = \varepsilon^{\gamma\delta\alpha\beta}u_\alpha m_\beta$ and we recall the definition of the four-velocity $u^\alpha = (\gamma, \gamma\mathbf{v}/c)$ and of the magnetic dipole moment four-vector

$$m^\alpha = \left(\gamma\,\mathbf{m}\cdot\frac{\mathbf{v}}{c}, \gamma\mathbf{m}\right) \tag{1.35}$$

where

$$\mathbf{m} = \frac{\mathbf{m}_0}{\gamma} + \frac{\gamma(\frac{\mathbf{v}}{c}\cdot\mathbf{m}_0)}{1+\gamma}\frac{\mathbf{v}}{c} \tag{1.36}$$

and $\mathbf{m}_0$ is the magnetic dipole moment in the instantaneous rest frame

$$\mathbf{m}_0 = g\frac{e\hbar}{2mc}\left(\frac{\mathbf{S}}{\hbar}\right) \tag{1.37}$$

where $g \approx 2$ is the gyromagnetic ratio and $\mathbf{S} = \hbar\langle\vec{\sigma}\rangle/2$ is the expectation value of the spin vector and $\vec{\sigma}$ are the Pauli matrices.

It may be convenient to introduce the dual tensor of the electromagnetic field $\mathcal{F}^{\alpha\beta} = \varepsilon^{\alpha\beta\gamma\delta}F_{\gamma\delta}/2$ then the spin force Eq. (1.34) becomes

$$g^\mu = -\partial^\mu\mathcal{F}^{\alpha\beta}u_\alpha m_\beta + (\partial_\gamma\mathcal{F}^{\alpha\beta}u_\alpha m_\beta u^\gamma)u^\mu \tag{1.38}$$

In the non-relativistic limit Eq. (1.38) becomes

$$g_j = m_i \partial_j B_i = \partial_j m_i B_i \tag{1.39}$$

or equivalently

$$\mathbf{g} = \nabla(\mathbf{m} \cdot \mathbf{B}) \tag{1.40}$$

which is the usual non-relativistic force for a magnetic dipole.

Eq. (1.34) or equivalently Eq. (1.38) have to be compared with the RR force which can be conveniently split into two four-forces

$$f^{\mu}_{R1} = \frac{2e^3}{3mc^2} \left(\partial_\alpha F^{\mu\nu} u_\nu u^\alpha\right) \tag{1.41}$$

$$f^{\mu}_{R2} = \frac{2e^4}{3m^2c^4} \left(F^{\mu\nu} F_{\nu\alpha} u^\alpha + (F^{\nu\beta} u_\beta F_{\nu\alpha} u^\alpha) u^\mu\right) \tag{1.42}$$

In the classical framework and in the laboratory frame[11], both the RR force and the spin force significantly affect the dynamics only in the ultra-relativistic limit while their contribution is negligible in the non-relativistic limit. In the ultra-relativistic limit, the spin force is dominated by the last term of Eq. (1.38) i.e. it is directed along the velocity and its strength is

$$\left[\partial_\gamma \mathcal{F}^{\alpha\beta} u_\alpha m_\beta u^\gamma\right] = \gamma^3 \left[(D_t \mathbf{B} \cdot \mathbf{m}) + (D_t \mathbf{E} \times \frac{\mathbf{v}}{c}) \cdot \mathbf{m} - (D_t \mathbf{B} \cdot \frac{\mathbf{v}}{c})(\frac{\mathbf{v}}{c} \cdot \mathbf{m})\right] \tag{1.43}$$

where we have introduced the operator

$$D_t \equiv \left(\frac{1}{c}\frac{\partial}{\partial t} + \left(\frac{\mathbf{v}}{c} \cdot \nabla\right)\right) \tag{1.44}$$

which is the 'total' time derivative.

In the ultra-relativistic limit $\gamma \gg 1$ and from Eq. (1.36)

$$\mathbf{m} \approx (\frac{\mathbf{v}}{c} \cdot \mathbf{m}_0)\frac{\mathbf{v}}{c} + \frac{\mathbf{m}_0}{\gamma} = (\frac{\mathbf{v}}{c} \cdot \mathbf{m})\frac{\mathbf{v}}{c} + \frac{\mathbf{m}_0}{\gamma}\,. \tag{1.45}$$

since $(\mathbf{v} \cdot \mathbf{m}_0) = (\mathbf{v} \cdot \mathbf{m})$ and from Eq. (1.45) we get for the first term of Eq. (1.43)

$$(D_t \mathbf{B} \cdot \mathbf{m}) \approx (D_t \mathbf{B} \cdot \frac{\mathbf{v}}{c})(\frac{\mathbf{v}}{c} \cdot \mathbf{m}) + \frac{(D_t \mathbf{B} \cdot \mathbf{m}_0)}{\gamma}\,. \tag{1.46}$$

[11] That is in the frame where the plasma target is initially at rest, this discussion is similar to that of the effective reduced LL equation (1.26).

The first term of Eq. (1.46) cancels the last term of Eq. (1.43) and substituting Eq. (1.36) in the second term of Eq. (1.43) we get

$$(D_t\mathbf{E} \times \frac{\mathbf{v}}{c}) \cdot \mathbf{m} = (D_t\mathbf{E} \times \frac{\mathbf{v}}{c}) \cdot \frac{\mathbf{m}_0}{\gamma} \tag{1.47}$$

and in the ultra-relativistic limit Eq. (1.43) becomes

$$\left[\partial_\gamma \mathcal{F}^{\alpha\beta} u_\alpha m_\beta u^\gamma\right] \approx \gamma^2 \left(D_t\mathbf{B} - \frac{\mathbf{v}}{c} \times D_t\mathbf{E}\right) \cdot \mathbf{m}_0 \tag{1.48}$$

Since in the following we mostly refer to the case of a plane wave, it is convenient to use normalized quantities, then Eq. (1.48) becomes

$$-\left(\frac{\pi\lambda_C}{\lambda}\right) \gamma^2 \left(D_t\mathbf{B} - \mathbf{v} \times D_t\mathbf{E}\right) \cdot \langle\vec{\sigma}\rangle \tag{1.49}$$

while the normalized spatial components of Eq.(1.41) are

$$-\left(\frac{4\pi r_e}{3\lambda}\right) \gamma \left(D_t\mathbf{E} + \mathbf{v} \times D_t\mathbf{B}\right) \tag{1.50}$$

and the dominant term of Eq. (1.42) (i.e. the friction-like term) is directed along the velocity and its strength in normalized units is

$$-\left(\frac{4\pi r_e}{3\lambda}\right) \gamma^2 \left[(\mathbf{E} + \mathbf{v} \times \mathbf{B})^2 - (\mathbf{v} \cdot \mathbf{E})^2\right] \tag{1.51}$$

Considering an ultra-relativistic electron interacting with a plane wave with normalized laser amplitude a_0:

1. From Eq. (1.49) the order of magnitude of the spin force is $\sim \pi\lambda_C\gamma^2 a_0/\lambda$ and we recall that $\lambda_C = r_e\alpha^{-1}$ and $\alpha \sim 1/137$.

2. From Eq. (1.50) the order of magnitude of the 'derivative' term of the RR force is $\sim 4\pi r_e\gamma a_0/3\lambda$.

3. From Eq. (1.51) the order of magnitude of the main friction-like term of the RR force is $\sim 4\pi r_e\gamma^2 a_0^2/3\lambda$.

4. The order of magnitude of the Lorentz force is a_0.

In conclusion, in the interaction of an ultra-relativistic electron with a plane wave in the classical framework:

1. The spin force is roughly $\alpha^{-1}\gamma \sim 137\gamma$ larger than the 'derivative' term of the RR force. Both forces have an oscillatory behavior and tend to average to zero after a wave cycle. The 'derivative' term of the RR force should therefore be neglected as its effect is much smaller than quantum effects such as spin effects which are neglected in the classical framework.

2. The dominant friction-like term of the RR force is is roughly $\alpha a_0 \sim a_0/137$ times the spin force, since in our simulations $a_0 \gtrsim 300$ the RR force dominates over the spin force. Moreover, the effect of the friction-like term of the RR force cumulates with the number of wave-cycles while the effect of the spin force tends to average to zero after a wave-cycle.

3. The Lorentz force is is roughly $\lambda/\pi\lambda_C\gamma^2$ times the spin force. When $\gamma \gtrsim \sqrt{\lambda/\pi\lambda_C}$ the spin force is comparable with the Lorentz force and the effect of spin degrees of freedom may become important. The order of magnitude of the threshold for spin effects is $\sqrt{\lambda/\pi\lambda_C} \sim 812$ for a typical laser wavelength $\lambda \sim 0.8\,\mu$m.

Finally, we mention that even though the issue of quantum effects in laser-plasma interaction at ultra-high intensities is currently much debated, it seems that the role of the spin degrees of freedom as well as their effect on the electron dynamics have not been considered yet. As discussed above, spin effects may become important when the order of magnitude of the spin force and of the Lorentz force are comparable during a wave-cycle.

Chapter 2

Electron motion in strong electromagnetic fields

The study of the motion of a single electron in a strong electromagnetic field is a natural starting point for a preliminary investigation of non-linear laser-plasma interactions. In fact, the study of the orbits of a single electron provides a reference picture in order to test suitable numerical schemes, interpret more complex systems and identify the relevant physical quantities.

2.1 Constant and uniform magnetic field

We begin our study focusing on the simple case of zero electric field and a constant and uniform magnetic field[1] along the z axis $\mathbf{B} = (0, 0, B)$. The temporal component (1.22) of the four-dimensional LL equation (1.13) provides the energy equation

$$\frac{d\gamma}{dt} = -\omega_c^2 \tau_0 \gamma^2 \left(\frac{\mathbf{v}_\perp^2}{c^2} \right) \tag{2.1}$$

while the spatial components (1.23) become

$$\frac{1}{c}\frac{d(\gamma \mathbf{v})}{dt} = \frac{e}{mc}\left(\frac{\mathbf{v}_\perp}{c} \times \mathbf{B} \right) - \omega_c^2 \tau_0 \left(\frac{\mathbf{v}_\perp}{c} \right) - \omega_c^2 \tau_0 \gamma^2 \left(\frac{\mathbf{v}_\perp^2}{c^2} \right) \frac{\mathbf{v}}{c} \tag{2.2}$$

where $\omega_c = |e|B/mc$ is the cyclotron frequency, $\mathbf{v}_\perp^2 = v_x^2 + v_y^2$ and $\mathbf{v} = \mathbf{v}_\perp + v_z \hat{\mathbf{z}}$. In order to make computations as simple as possible while retaining

[1] This problem can be fully solved and has been studied in detail in [29].

the physical content, we discuss the case $v_z = 0$. In this case, exploiting the identity $\mathbf{v}_\perp^2/c^2 = (1 - 1/\gamma^2)$, the energy equation (2.1) gives

$$\frac{d\gamma}{dt} = -\frac{1}{\tau_c}\left(\gamma^2 - 1\right) \tag{2.3}$$

where $\tau_c = 1/(\omega_c^2 \tau_0)$ is a characteristic time of the damping process due to radiation losses. The general solution of (2.3) is:

$$\gamma(t) = \frac{e^{2(t/\tau_c)} + e^{2c}}{e^{2(t/\tau_c)} - e^{2c}} = \coth\left(\frac{t}{\tau_c} - C\right) \tag{2.4}$$

where

$$C = -\frac{1}{2}\ln\left(\frac{\gamma(0)+1}{\gamma(0)-1}\right) \tag{2.5}$$

In order to highlight the relevant scale of RR effects, we consider the simpler case of an initially ultrarelativistic electron $\gamma(0) = \gamma_0 \gg 1$ then Eq.(2.3) reduces to

$$\frac{d\gamma}{dt} = -\frac{1}{\tau_c}\gamma^2 \tag{2.6}$$

and the general solution is:

$$\frac{\gamma(t)}{\gamma_0} = \frac{1}{1 + t\gamma_0/\tau_c} \tag{2.7}$$

The function $\gamma(t)$ decreases quickly (see Fig. 2.1) within a characteristic time τ_c/γ_0. Physically, this implies that the electron loses a significant fraction of its initial energy in a time τ_c/γ_0; more precisely, the energy halves $\gamma(t) \simeq \gamma_0/2$ after a time $t = \tau_c/\gamma_0$.

It's well known from standard textbooks [37] that in absence of RR an electron performs a circular motion with constant energy $\varepsilon = \gamma mc^2 = \varepsilon_0$ and the gyration frequency is $\omega = \omega_c/\gamma_0$. In order to estimate the relevance of RR effects, the characteristic time of revolution due to the Lorentz force $T = \gamma_0 T_c$ where $T_c = 2\pi/\omega_c$ has to be compared with the characteristic damping time of the RR force τ_c/γ_0. When the time of revolution is larger that the damping time $T > \tau_c/\gamma_0$ i.e. when $\gamma_0 > (1/2\pi)\sqrt{T_c/\tau_0}$, then the RR force dominates the electron motion.

However, there is an important constraint that comes from the requirement that we are not outside the boundaries of classical mechanics: the

relative change of the Lorentz force in a time λ_C/c must be small in the instantaneous rest frame i.e. the basic restriction (1.11) must be fulfilled. The restriction (1.11) divided by m^2c^2 after some lengthly calculations yields

$$\left|1-\gamma^2\left(\frac{\mathbf{v}_\perp^2}{c^2}\right)(\gamma^2-2)+\left(\frac{\mathbf{v}_\perp^4}{c^4}\right)\gamma^4\right| \ll \frac{c^2}{\omega_c^2\lambda_C^2} \tag{2.8}$$

and exploiting $\mathbf{v}_\perp^2/c^2=(1-1/\gamma^2)$ we finally get the simple inequality

$$\gamma \ll \frac{c}{\omega_c\lambda_C}=\frac{\alpha T_c}{3\pi\tau_0} \tag{2.9}$$

The RR force damps the motion thus $\gamma(t)\leq\gamma_0$ and it is sufficient to require that $\gamma_0 \ll \alpha T_c/3\pi\tau_0$. In conclusion, the energy interval

$$\frac{1}{2\pi}\sqrt{\frac{T_c}{\tau_0}} < \gamma_0 \ll \frac{\alpha}{3\pi}\frac{T_c}{\tau_0} \tag{2.10}$$

defines the strong radiation damping regime in the framework of classical mechanics; the larger the ratio T_c/τ_0 the larger the interval of energies where RR effects are dominant in the classical framework. For instance, for a magnetic field of the order of $B\sim 10^4\,\mathrm{G}$ we have $T_c\sim 3.57\times10^{-11}\,\mathrm{s}$ while $\tau_0\sim 6.27\times10^{-24}\,\mathrm{s}$ and from (2.10) we have: $3.8\times10^5<\gamma_0\ll 4.4\times10^9$.

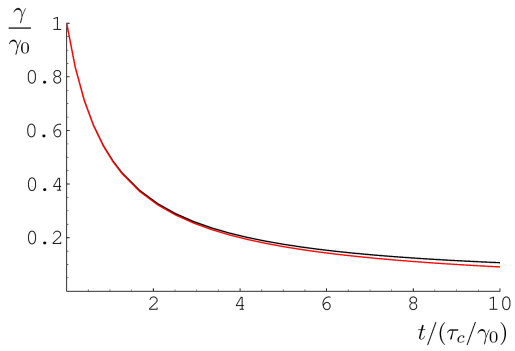

Figure 2.1: Plot of $\gamma(x)/\gamma_0$ where $x=t/(\tau_c/\gamma_0)$ for $\gamma_0=15$. The black line is the solution (2.4) and the red line is the solution (2.7).

2.2 Single electron in an electromagnetic plane wave

In this section, we consider the exact analytical solution of the LL equation for the case of an arbitrary plane wave [39]. This analytical solution is used in chapter 4 as a benchmark to test our leap-frog pusher with RR effects included.

As discussed previously, in order to highlight the relevant physical scales and to implement the equation of motion into numerical codes, normalized quantities are used

$$\begin{cases} t \mapsto \omega t \\ \mathbf{x} \mapsto k\mathbf{x} \\ \mathbf{v} \mapsto \mathbf{v}/c \end{cases} \quad \begin{cases} \mathbf{p} \mapsto \frac{\mathbf{p}}{mc} \\ \mathbf{A} \mapsto \frac{|e|}{mc^2}\mathbf{A} \end{cases} \quad \begin{cases} \mathbf{E} \mapsto \frac{|e|}{mc\omega}\mathbf{E} \\ \mathbf{B} \mapsto \frac{|e|}{mc\omega}\mathbf{B} \end{cases} \quad \begin{cases} \omega = c\frac{2\pi}{\lambda} \\ k = \frac{2\pi}{\lambda} \end{cases} \tag{2.11}$$

This implies that time is in units of ω^{-1}, space is in units of $k^{-1} = c\omega^{-1}$, velocities in units of c, momenta in units of mc and fields in units of $mc\omega/|e|$. We also recall the 'practical' relation between the normalized laser amplitude a_0 and the laser intensity I

$$a_0 \equiv \frac{|e|E}{m\omega c} \approx 0.85\sqrt{\frac{I\lambda^2}{10^{18}\ \mathrm{W\,cm^{-2}}\,\mu\mathrm{m}^2}} \tag{2.12}$$

Let's consider an arbitrary plane wave moving along the positive x-axis, we introduce the phase of the wave at the particle position $\varphi = t - x(t)$ as the independent variable. The four-vector potential in the Coulomb gauge is

$$A^\mu(\varphi) = (0, 0, a_0\psi_1(\varphi), a_0\psi_2(\varphi)) \tag{2.13}$$

thus the electric and magnetic fields are

$$\mathbf{E} = (0, -a_0\psi_1'(\varphi), -a_0\psi_2'(\varphi)) \tag{2.14}$$

$$\mathbf{B} = (0, a_0\psi_2'(\varphi), -a_0\psi_1'(\varphi)) \tag{2.15}$$

where $\psi_1(\varphi)$ and $\psi_2(\varphi)$ are two *arbitrary* scalar functions of φ and the prime indicates the derivative respect to φ. In the special case of a monochromatic plane wave

$$\psi_1(\varphi) = \delta\cos(\varphi); \qquad \psi_2(\varphi) = \sqrt{1-\delta^2}\sin(\varphi) \tag{2.16}$$

where δ is the polarization parameter, $\delta = \{\pm 1, 0\}$ for linear polarization and $\delta = \{\pm 1/\sqrt{2}\}$ for circular polarization.

First, we introduce the components $\gamma(\varphi)$, $p_x(\varphi)$, $p_y(\varphi)$, $p_z(\varphi)$ of the exact solution with the auxiliary functions $h(\varphi)$ and $\mathcal{I}_i(\varphi)$ and then we discuss their physical interpretation in terms of the electric (2.14) and magnetic (2.15) fields. The components of the exact solutions are

$$\begin{aligned}\gamma(\varphi) &= \frac{1}{h(\varphi)}\Bigg[\gamma_0 + \frac{1}{\rho_0}\Big(\mathcal{I}_1(\varphi)p_{y_0} + \mathcal{I}_2(\varphi)p_{z_0}\Big) \\ &\quad + \frac{1}{2\rho_0}(h^2(\varphi)-1) + \frac{1}{2\rho_0}\Big(\mathcal{I}_1^2(\varphi) + \mathcal{I}_2^2(\varphi)\Big)\Bigg] \qquad (2.17)\\ p_x(\varphi) &= \frac{1}{h(\varphi)}\Bigg[p_{x_0} + \frac{1}{\rho_0}\Big(\mathcal{I}_1(\varphi)p_{y_0} + \mathcal{I}_2(\varphi)p_{z_0}\Big) \\ &\quad + \frac{1}{2\rho_0}(h^2(\varphi)-1) + \frac{1}{2\rho_0}\Big(\mathcal{I}_1^2(\varphi) + \mathcal{I}_2^2(\varphi)\Big)\Bigg] \qquad (2.18)\\ p_y(\varphi) &= \frac{1}{h(\varphi)}\Big[p_{y_0} + \mathcal{I}_1(\varphi)\Big] \qquad (2.19)\\ p_z(\varphi) &= \frac{1}{h(\varphi)}\Big[p_{z_0} + \mathcal{I}_2(\varphi)\Big] \qquad (2.20)\end{aligned}$$

where the subscript zero indicates quantities at $t = 0$ and we have introduced the Doppler factor

$$\rho_0 \equiv \gamma_0(1 - v_{x_0}) \qquad (2.21)$$

that accounts for the change in the wavelength. In fact, in the case $v_{y_0} = v_{z_0} = 0$ the formula (2.21) reduces to the well-known expression

$$\rho_0 = \sqrt{\frac{1 - v_{x_0}}{1 + v_{x_0}}}\,. \qquad (2.22)$$

We have also introduced the following auxiliary functions

$$h(\varphi) = 1 + \left(\frac{4}{3}\pi\frac{r_e}{\lambda}\right)\rho_0 \int_{\varphi_0}^{\varphi} \left[\mathbf{E}(\phi) \times \mathbf{B}(\phi)\right]_x \, d\phi \qquad (2.23)$$

and

$$\begin{aligned}\mathcal{I}_i(\varphi) &= -\int_{\varphi_0}^{\varphi} E_i(\phi)d\phi \\ &\quad - \left(\frac{4}{3}\pi\frac{r_e}{\lambda}\right)\rho_0\Big[E_i(\varphi) - E_i(\varphi_0)\Big]\end{aligned}$$

$$- \left(\frac{4}{3}\pi\frac{r_e}{\lambda}\right)\rho_0 \int_{\varphi_0}^{\varphi} d\phi\, E_i(\phi) \int_{\varphi_0}^{\phi} d\vartheta \left(\mathbf{E}(\vartheta)\times\mathbf{B}(\vartheta)\right)_x \tag{2.24}$$

where the suffix x indicates the component x of the vector $\mathbf{E}\times\mathbf{B}$.

In order to identify the relevant terms and parameters, we substitute in equations (2.23) and (2.24) the components of the electric (2.14) and magnetic (2.15) fields

$$h(\varphi) = 1 + R\int_{\varphi_0}^{\varphi} d\phi \left[(\psi_1'(\phi))^2 + (\psi_2'(\phi))^2\right] \tag{2.25}$$

and

$$\begin{aligned}\mathcal{I}_i(\varphi) = {} & a_0\Big[\psi_i(\varphi) - \psi_i(\varphi_0)\Big] \\ & + \frac{R}{a_0}\Big[\psi_i'(\varphi) - \psi_i'(\varphi_0)\Big] \\ & + Ra_0 \int_{\varphi_0}^{\varphi} d\phi\, \psi'(\phi) \int_{\varphi_0}^{\phi} d\vartheta \Big[(\psi_1'(\vartheta))^2 + (\psi_2'(\vartheta))^2\Big]\end{aligned} \tag{2.26}$$

where we have introduced the RR parameter

$$R \equiv \left(\frac{4}{3}\pi\frac{r_e}{\lambda}\right)\rho_0\, a_0^2 \tag{2.27}$$

that signals the onset of the strong RR regime (see Refs.[17, 10]). The usual solution without RR effects is recovered formally[2] in the limit $r_e/\lambda \to 0$ or equivalently $R \to 0$ so it is easy to identify the new terms due to the presence of the RR force. By inspection of equations (2.17 - 2.20), we see that the most relevant factors are $h(\varphi)$ and $\mathcal{I}_i^2(\varphi)$. We provide a physical interpretation of each term and discuss how it affects the electron motion.

2.2.1 The physical picture and the relevant parameters

We start discussing the function $h(\varphi)$, it is essentially an energy-momentum suppression factor due to the irreversible four-momentum loss by emission

[2]This *does not* imply that the RR force vanishes in the limit $\lambda \to \infty$ i.e. constant uniform fields as we are using normalized units that are implicit functions of λ.

of radiation. In fact, in equations (2.17 - 2.20) $h(\varphi)$ appears at the denominator suppressing the initial electron energy and momentum. Subtracting Eq.(2.18) from Eq.(2.17) we get

$$\gamma(\varphi) - p_x(\varphi) = \frac{1}{h(\varphi)} \left(\gamma_0 - p_{x_0}\right) \tag{2.28}$$

and therefore $1 - h(\varphi)^{-1}$ provides the percentage of violation of the usual conservation law $\gamma(\varphi) - p_x(\varphi) = (\gamma_0 - p_{x_0})$ and of the Lawson-Woodward theorem (see Ref. [22] and references therein). Since $h(\varphi_0) = 1$, then Eq.(2.28) can be recast as a 'modified conservation law'

$$h(\varphi) \left(\gamma(\varphi) - p_x(\varphi)\right) = h(\varphi_0) \left(\gamma_0 - p_{x_0}\right) \tag{2.29}$$

and, since $\mathcal{I}_i(\varphi_0) = 0$, from Eqs. (2.19, 2.20) a similar 'modified conservation law' can be written for the transverse momentum

$$h(\varphi) p_{y,\,z}(\varphi) - \mathcal{I}_{1,\,2}(\varphi) = h(\varphi_0) p_{y_0,\,z_0} - \mathcal{I}_{1,\,2}(\varphi_0) \tag{2.30}$$

and therefore if $h(\varphi) \neq 1$ or $\mathcal{I}_{1,\,2}(\varphi) \neq 0$ *after* the electron-plane wave interaction phase, then the electron has gained a net longitudinal (see Eq. (2.18)) and transverse momentum (see Eq. (2.19, 2.20)). The fact that the RR force allows the electron to gain a net momentum after the interaction with a plane wave is not an intrinsic property of the RR force; it is known that a simple constant friction force in Newton's equations allows a net gain of energy and momentum in the interaction with a plane wave. For instance, for a non-relativistic electron in a linearly polarized plane wave with a constant friction term $k > 0$ we have $d\mathbf{v}/dt = -(\mathbf{E} + \mathbf{v} \times \mathbf{B}) - k\mathbf{v}$ with $\mathbf{E} = (0, E_0 \sin(t), 0)$ and $\mathbf{B} = (0, 0, E_0 \sin(t))$. Assuming $|\mathbf{v}| \ll 1$ then $v_y \simeq E_0(\cos(t) - 1) + v_{y_0}$ and substituting into the equation for v_x we have $dv_x/dt \simeq -E_0 v_{y_0} \sin(t) + E_0^2(\sin(t) - \sin(2t)/2) - kv_x$ and if $k > 0$ then the value of v_x is *not* zero after an integer number of laser periods.

Figure 2.2 shows the trajectory of an electron during the interaction with a monochromatic linearly polarized plane wave in the so called "average rest frame" i.e. in the frame where the electron describes a 'figure of eight' when the RR force is neglected. The red curve describes the electron trajectory without RR effects while the black curve describes the electron trajectory

with RR effects. When RR effects are accounted, the 'figure of eight' begins to open and the electron drifts with increasing velocity along the plane wave propagation direction.

From equation (2.23) we see that the RR contribution is

$$\left(\frac{4}{3}\pi\frac{r_e}{\lambda}\right)\rho_0\int_{\varphi_0}^{\varphi}\left[\mathbf{E}(\phi)\times\mathbf{B}(\phi)\right]_x\,d\phi \tag{2.31}$$

which is the normalized fluence times the Doppler factor times the ratio of the effective electron size with the laser wavelength. This implies that what is really important for the final RR contribution is the ratio between the effective electron size and the laser wavelength in the *initial rest frame* times the electromagnetic momentum integrated along the electron's worldline. From equation (2.25) we see that the RR contribution is relevant if

$$R\int_{\varphi_0}^{\varphi}d\phi\left[(\psi_1'(\phi))^2+(\psi_2'(\phi))^2\right]\gtrsim 1 \tag{2.32}$$

The two following regimes are possible:

1. The radiation damping regime $R\ll 1$ and the integral contribution is much larger than the unity so that the total result is

   $$R\int_{\varphi_0}^{\varphi}d\phi\left[(\psi_1'(\phi))^2+(\psi_2'(\phi))^2\right]\gtrsim 1$$

   which implies that the laser pulse is very long and the RR contribution becomes important only as a cumulative effect so that the *total* integrated electromagnetic momentum is large. At fixed wavelength λ, peak intensity I and initial electron conditions, two pulses that differ for the total energy-momentum content produce different final RR effects.

2. The strong radiation damping regime $R\gtrsim 1$. This implies that the RR force dominates the electron dynamics and

   $$R\int_{\varphi_0}^{\varphi}d\phi\left[(\psi_1'(\phi))^2+(\psi_2'(\phi))^2\right]\gtrsim 1$$

   the electron loses a large fraction of its initial energy even after a single wave cycle. Even in the case that the *final* RR contribution is the same

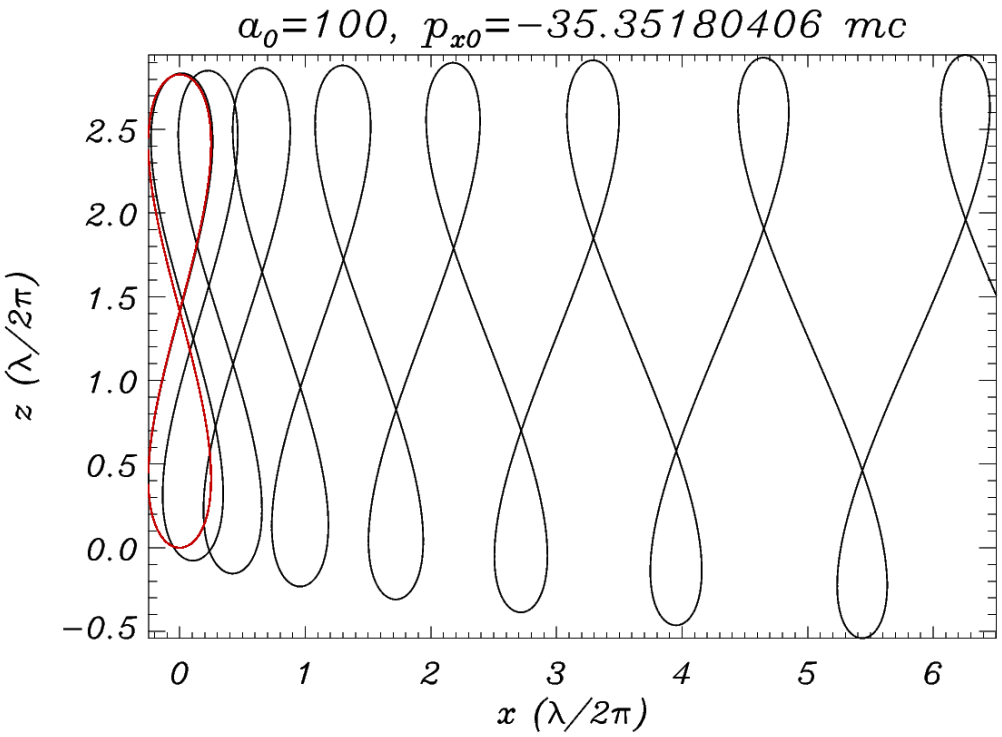

Figure 2.2: Electron trajectory during the interaction with a monochromatic linearly polarized plane wave in the so called "average rest frame". The normalized amplitude of the plane wave is $a_0 = 100$ with a wavelength $\lambda = 0.8\,\mu$m that corresponds to an intensity $I \sim 2.2 \times 10^{22}\,\mathrm{W\,cm^{-2}}$. The plane wave is propagating along the positive x-axis while the electron is initially counter-propagating with the plane wave with initial momentum $p_{x_0} = -35.35\,mc$. The red curve describes the electron trajectory without RR effects while the black curve describes the electron trajectory with RR effects.

obtained by a less intense but longer laser pulse, the dynamics during the electron-pulse interaction, the physical scales and the emitted spectrum are very different.

We point out that the *temporal* scales required to have significant RR effects for fixed RR parameter R are strongly dependent on the motion since the integral contribution in Eq. (2.32) can grow very quickly or very slowly *in time* compared to the wave period depending on the electron worldline. For instance, in the interaction of an electron initially at rest with a plane wave with wavelength $\lambda = 0.8\,\mu$m and normalized amplitude $a_0 = 1000$, from Eq. (2.27) we have $R \sim 0.015$. The same value is obtained in the interaction of an electron with initial momentum $p_{x_0} = -50\,mc$ and a plane wave with $\lambda = 0.8\,\mu$m and $a_0 = 100$. However, in the first case the integral in Eq. (2.32) grows slowly in time because the phase φ grows slowly in time. In fact, in the first case the electron is immediately pushed along the positive x-direction by the Lorentz force, then $\varphi = t - x(t) \simeq \varphi_0$ for many waveperiods and the RR contribution in Eq. (2.32) grows slowly in time (see the left frame of Fig. 2.3). In the second case, the electron collides head-on with the laser pulse and both the phase $\varphi = t - x(t)$ and the RR contribution in Eq. (2.32) grow quickly (see the right frame of Fig. 2.3).

The other important functions in Eqs. (2.17 - 2.20) are $\mathcal{I}_{1,\,2}(\varphi)$. These functions give the dominant contribution to RR effects during the electron-wave interaction as they appear squared in Eqs. (2.17, 2.18) and they contain a term that depends on the *third power* of the normalized laser amplitude a_0. The formal role of $\mathcal{I}_{1,\,2}(\varphi)$ in equations (2.19 - 2.20) suggests to interpret these functions as terms of a 'modified' generalized canonical momentum.

From equation (2.24) we see that the first term of $\mathcal{I}_i(\varphi)$

$$-\int_{\varphi_0}^{\varphi} E_i(\phi)d\phi \tag{2.33}$$

is the change in transverse momentum carried out by the electric field, comes from Lorentz force and it always vanishes after the interaction with the wave (except in the case $\omega = 0$ i.e. there are constant crossed fields superimposed with the propagating wave). The second term

$$-\left(\frac{4}{3}\pi\frac{r_e}{\lambda}\right)\rho_0\Big[E_i(\varphi) - E_i(\varphi_0)\Big] \tag{2.34}$$

is the variation of the electric field seen by the moving particle. This term comes from the term of the LL equation (1.23) that depends on the derivatives of the fields, gives a negligible contribution and always vanishes after the interaction as the fields before $E_i(\varphi_0)$ and after $E_i(\varphi)$ the interaction are zero. The third term

$$-\left(\frac{4}{3}\pi\frac{r_e}{\lambda}\right)\rho_0\int_{\varphi_0}^{\varphi}d\phi\,E_i(\phi)\int_{\varphi_0}^{\phi}d\vartheta\left(\mathbf{E}(\vartheta)\times\mathbf{B}(\vartheta)\right)_x \tag{2.35}$$

is the change in transverse momentum carried out by the electric field averaged by the normalized fluence and comes from the irreversible friction-like term of the RR force. This term is usually strongly oscillatory and for monochromatic-like laser pulses its final contribution is almost zero but it can significantly affect the motion during the interaction. In fact, using the components of the electric and magnetic fields Eq. (2.35) becomes (see Eq. (2.26))

$$Ra_0\int_{\varphi_0}^{\varphi}d\phi\,\psi'(\phi)\int_{\varphi_0}^{\phi}d\vartheta\Big[(\psi_1'(\vartheta))^2+(\psi_2'(\vartheta))^2\Big] \tag{2.36}$$

This implies that even though $R\ll 1$, the RR force can significantly affect the motion when $a_0\gg 1$ and $Ra_0>1$. Since $\gamma(\varphi)$ and $p_x(\varphi)$ in Eqs. (2.17, 2.18) depend on the square of $\mathcal{I}_i(\varphi)$ (more precisely on $\mathcal{I}_i^2(\varphi)/2\rho_0$), the two leading RR term in Eqs. (2.17, 2.18) are

$$\frac{Ra_0^2}{\rho_0}\Big[\psi_i(\varphi)-\psi_i(\varphi_0)\Big]\int_{\varphi_0}^{\varphi}d\phi\,\psi'(\phi)\int_{\varphi_0}^{\phi}d\vartheta\Big[(\psi_1'(\vartheta))^2+(\psi_2'(\vartheta))^2\Big] \tag{2.37}$$

which comes from the double product of (2.36) with the Lorentz term (2.33) and

$$\frac{R^2a_0^2}{2\rho_0}\left[\int_{\varphi_0}^{\varphi}d\phi\,\psi'(\phi)\int_{\varphi_0}^{\phi}d\vartheta\Big[(\psi_1'(\vartheta))^2+(\psi_2'(\vartheta))^2\Big]\right]^2 \tag{2.38}$$

which comes from the square of (2.36).

The term in Eq. (2.37) is proportional to the *fourth* power of a_0 and is independent on ρ_0 as $Ra_0^2/\rho_0=(4\pi r_e/3\lambda)a_0^4$ (see Eq. (2.27)). Since for a propagating wave (i.e. when there is no $\omega=0$ component) the final contribution of $[\psi_i(\varphi)-\psi_i(\varphi_0)]$ is zero, this term does not lead to a net gain of momentum. However, when $R<1$ this is the dominant contribution

due to RR effects during the electron-wave interaction and it can reach peak values comparable or larger than the initial momentum p_{x_0}.

The term in Eq. (2.38) is proportional to the *sixth* power of a_0 and is proportional to ρ_0 as $R^2 a_0^2/2\rho_0 = (4\pi r_e/3\lambda)^2 \rho_0 a_0^6/2$ and when $R > 1$ this is the dominant contribution due to RR effects. Indeed when $R > 1$, it reaches values that are larger than the Lorentz term and the electron motion is dominated by the RR force.

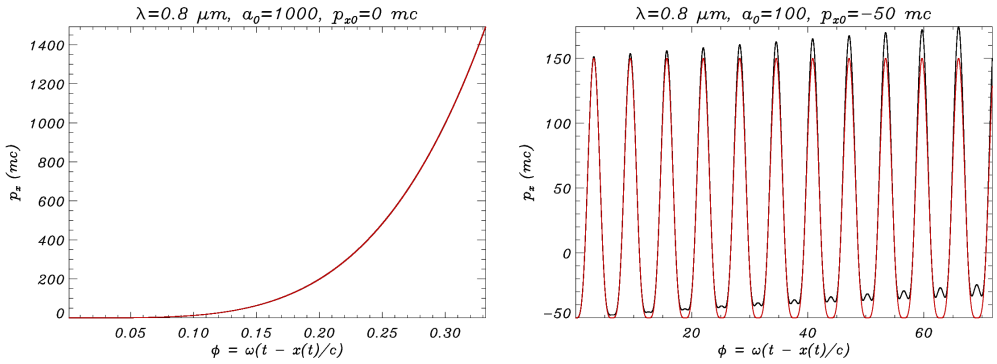

Figure 2.3: Plots of the longitudinal electron momentum p_x as a function of the phase ϕ in the interaction with a monochromatic linearly polarized plane wave propagating along the positive x-axis. The red curve is the trajectory without RR while the black curve is the trajectory with RR. A fourth-order Runge-Kutta method was used with timestep $\Delta T = \omega^{-1}/1000$ and in both cases the simulation lasted in total $100\omega^{-1}$. Left frame: the laser wavelength is $\lambda = 0.8\,\mu$m and the normalized amplitude is $a_0 = 1000$ corresponding to an intensity $I \sim 2.2 \times 10^{24}\,\mathrm{W\,cm^{-2}}$, the electron is initially at rest. In this case the phase ϕ grows slowly and RR effects do not play an appreciable role, yet. In fact, the red and the black curves are almost superimposed. Right frame: the laser wavelength is $\lambda = 0.8\,\mu$m and the normalized amplitude is $a_0 = 100$ corresponding to an intensity $I \sim 2.2 \times 10^{22}\,\mathrm{W\,cm^{-2}}$, the electron has an initial momentum $p_{x_0} = -50\,mc$. In this case the phase φ grows quickly and RR effects are apparent. Comparing the left and the right frames, notice the different range for the phase ϕ although the total run time is the same.

Chapter 3

Kinetic theory for a plasma with radiation reaction

In this chapter we briefly discuss the kinetic theory of an optically thin plasma with RR effects included. We determine a few basic properties of the kinetic equation pointing out the peculiarities of the RR force whose main new feature is that it does not conserve the phase-space volume. Generalized kinetic equations for non-conservative forces and in particular for the RR force have been known since late sixties for the LAD equation [40, 41] and late seventies for the LL equation [46]. Recently, the generalized kinetic equation has been used to study the RR effects on thermal electrons in a magnetically confined plasma [42] and to develop a set of closed fluid equations with RR effects included [43, 44, 45].

We start recalling the basic physical assumption that allows to replace the many-body description of a plasma as a discrete system of interacting point-like particles with a smooth statistical distribution function $f = f(\mathbf{x}, \mathbf{p}, t)$ evolving with self-consistent fields in the mean field approximation. The assumption is that the mean interparticle distance $n^{-1/3}$, where n is the electron density, is much smaller than the other relevant spatial scales such as the wavelength of the emitted or absorbed radiation. When distances below $n^{-1/3}$ are probed, the predictions of the statistical theory in the mean field approximation are no longer valid and effects below $n^{-1/3}$ must be included into the kinetic equation with some suitable approach. In particular, when

the wavelength of the radiation emitted by a plasma λ_e is much larger than the interparticle distance i.e. $\lambda_e \gg n^{-1/3}$, the process of emission as well as the 'back-reaction' due to such emission is accounted self-consistently by the usual coupled system of kinetic and Maxwell equations in the mean field approximation. On the contrary, when the wavelength of the emitted radiation is smaller the mean interparticle distance $\lambda_e \lesssim n^{-1/3}$, the emission becomes a single particle 'incoherent' process and such emission must be included in the kinetic equation with some suitable approach[1].

Assuming an optical laser wavelength $\lambda \sim 1\,\mu$m and a typical solid-density plasma of the order of $n \sim 100\, n_c$ where

$$n_c \equiv \frac{m\omega^2}{4\pi e^2} = \frac{\pi}{r_e \lambda^2} \approx 1.115 \times 10^9 \left(\frac{1\,\mu\text{m}}{\lambda}\right)^2 \mu\text{m}^{-3} \tag{3.1}$$

is the critical density, the mean interparticle distance if of the order of $n^{-1/3} \sim (100\, n_c)^{-1/3} \sim 2\times 10^{-4}$ μm or equivalently $n^{-1/3} \sim 2\times 10^{-4}\lambda$ since $\lambda \sim 1\,\mu$m. As discussed in the first chapter, the instantaneous emission spectrum of an ultra-relativistic electron is approximately synchrotron-like and the main part of the emitted radiation is concentrated in the region of frequencies $\omega_e \sim \gamma^2 |e|E/mc = \gamma^2 a_0\, \omega$ which corresponds to an emitted radiation with wavelength $\lambda_e \sim \lambda/\gamma^2 a_0$. In regimes where RR effects are important $a_0 \sim 3 \times 10^2$ and the electron energy is typically of the same order of magnitude of a_0 (see e.g. the results of our simulations in chapter 5). Hence, the spectrum of the emitted radiation is peaked around a wavelength of the order of $\lambda_e \sim 4\times 10^{-8}\lambda$ i.e. around a wavelength that is about *four*-orders of magnitude smaller than the typical mean electron distance $n^{-1/3} \sim 2\times 10^{-4}\lambda$. The back-reaction due to the emission of such high-energy photons with wavelength much smaller than the mean electron distance is therefore a single particle process that is not accounted by the usual system of kinetic and Maxwell equations in the mean field approximation.

Finally, we mention that the inclusion in the kinetic equation of a new term that accounts for the single electron emission of high-frequency radiation

[1]We recall that the 'coherent back-reaction' included in the mean field description of a plasma scales with the *square* of the number of particles while the 'incoherent back-reaction' or RR scales linearly with the number of particles.

leads to a 'double-counting' of the contribution to the 'back-reaction' of all the wavelengths $\bar{\lambda}$ in the range $\bar{\lambda} \gtrsim n^{-1/3}$. In fact, the emission and the consequent 'back-reaction' of radiation with wavelength $\bar{\lambda} \gtrsim n^{-1/3}$ is already accounted by the coupled system of kinetic and Maxwell equation in the mean field approximation. On the other side, the 'friction' term of the RR force (Eq. 1.26) is proportional to the total intensity emitted by a single electron that contains also a contribution from wavelengths in the range $\bar{\lambda} \gtrsim n^{-1/3}$ that is therefore double-counted. However, the contribution to the intensity emitted by a single electron from wavelengths in the range $\bar{\lambda} \gtrsim n^{-1/3}$ is small since the emission is peaked at much smaller wavelengths.

Moreover, a suitable mesh for space and time has to be used in PIC simulations. This mesh introduces a cut-off wavelength of the order of the spatial space-step Δx of the mesh that is typically orders of magnitude larger than the physical cut-off wavelength $n^{-1/3}$ for the self-consistent fields in the mean field approximation[2]. Hence, in a PIC simulation the range of wavelengths contributing to both the strength of the RR force and to the back-reaction from the coupled kinetic and Maxwell equations for self-consistent fields is $\bar{\lambda} \gtrsim \Delta x \gg n^{-1/3} \gg \lambda_e$. We recall that the contribution to the strength of the RR force mainly comes from wavelengths peaked around $\lambda_e \sim \lambda/\gamma^2 a_0$ while the contribution from comparatively much longer wavelengths is very small and therefore the issue of double-counting is of little practical relevance[3].

3.1 Basic properties of the kinetic equation

In this section, a fully relativistic kinetic equation that includes RR effects is discussed and original results of the author about the evolution of the phase-space are reported. We provide the kinetic equation in a non-manifestly covariant form, see Ref. [46] for a discussion of the Bogolyubov

[2]A possible exception might be the study of high-harmonic generation where 1D simulations with very high spatial and temporal resolution can be performed.

[3]To summarize the typical relevant scales in a PIC simulation of the interaction of a laser pulse with an overdense plasma, $\lambda > \delta > \Delta x \gg n^{-1/3} \gg \lambda_e$ where λ is the laser wavelength, $\delta = c/\omega_p$ is the skin depth (ω_p is the plasma frequency), Δx is the space-step in the PIC simulation, $n^{-1/3}$ is the mean electron distance and $\lambda_e \sim \lambda/\gamma^2 a_0$ is the typical wavelength of the radiation emitted incoherently by a single electron.

hierarchy of equations with RR in a manifestly Lorentz-covariant form and Ref. [42] for an application of the manifestly covariant equation to thermal electrons in a magnetically confined plasma.

In order to keep the notation as simple as possible we use the dimensionless quantities introduced in Eq. (2.11). The relativistic distribution function $f = f(\mathbf{x}, \mathbf{p}, t)$ evolves according to the collisionless transport equation

$$\frac{\partial f}{\partial t} + \nabla_{\mathbf{x}} \cdot (f\, \mathbf{v}) + \nabla_{\mathbf{p}} \cdot (f\, \mathbf{F}) = 0\,, \tag{3.2}$$

where $\mathbf{x}$ are the spatial coordinates, $\mathbf{v} = \mathbf{p}/\gamma$ is the three-dimensional velocity, $\gamma = \sqrt{1 + \mathbf{p}^2}$ is the relativistic factor and $\mathbf{F} = \mathbf{F}_L + \mathbf{F}_R$ is the mean force due to external and collective fields ($\mathbf{F}_L \equiv -(\mathbf{E} + \mathbf{v} \times \mathbf{B})$ is the Lorentz force and $\mathbf{F}_R$ is the LL force introduced in Eq. (1.24)).

We remark that the kinetic equation (3.2) only requires a system of equations of motion and *does not* require that these equations of motion are derived from an Hamiltonian. Physically, Eq.(3.2) implies the conservation of the number of particles as easily found integrating Eq.(3.2) in the phase-space and using the divergence theorem. An equivalent expression of (3.2) is

$$\frac{\partial f}{\partial t} + \mathbf{v} \cdot \nabla_{\mathbf{x}} f + \mathbf{F} \cdot \nabla_{\mathbf{p}} f + f \nabla_{\mathbf{p}} \cdot \mathbf{F} = 0 \tag{3.3}$$

The new key feature compared to the usual Vlasov equation is that for the RR force $\mathbf{F}_R$ we have $\nabla_{\mathbf{p}} \cdot \mathbf{F}_R \neq 0$.

Considering a small phase-space volume element, it is convenient to use Lagrangian coordinates $\mathbf{x}(t)$, $\mathbf{p}(t)$ that describe the position of the volume element in the phase-space at a given time t in order to follow its evolution as it moves through the phase-space. Then, Eq.(3.3) can be recast in the equivalent form

$$\frac{df}{dt} = -f\, \nabla_{\mathbf{p}} \cdot \mathbf{F} \tag{3.4}$$

or equivalently

$$\frac{d \ln f}{dt} = -\nabla_{\mathbf{p}} \cdot \mathbf{F}\,. \tag{3.5}$$

According to Eq.(3.5), $\nabla_{\mathbf{p}} \cdot \mathbf{F}$ provides the percentage of variation of the distribution function f within the characteristic time scale ω^{-1} (as normalized units are used). Integrating Eq.(3.5) along its characteristics, we find that

the distribution function f remains positive as required[4]

$$f = f_0\, e^{-\int_{t_0}^{t} \nabla_{\mathbf{p}}\cdot\mathbf{F}\, dt} \tag{3.6}$$

since the exponential is never zero or negative for any real value.

Introducing the entropy density in the phase space

$$s(\mathbf{x},\mathbf{p},t) = -f(\mathbf{x},\mathbf{p},t)\ln f(\mathbf{x},\mathbf{p},t)\,, \tag{3.7}$$

taking the partial derivative respect to time of $s(\mathbf{x},\mathbf{p},t)$ and using the kinetic equation (3.2) we straightforwardly get the equation for the evolution of the entropy density

$$\frac{\partial s}{\partial t} + \nabla_{\mathbf{x}}\cdot(s\,\mathbf{v}) + \nabla_{\mathbf{p}}\cdot(s\,\mathbf{F}) = f\,\nabla_{\mathbf{p}}\cdot\mathbf{F}\,. \tag{3.8}$$

Integrating Eq.(3.8) in the phase space, we get the rate of variation of the total entropy $S(t) = \int d^3x\, d^3p\; s(\mathbf{x},\mathbf{p},t)$

$$\frac{dS(t)}{dt} = \int d^3x\, d^3p\; f\,\nabla_{\mathbf{p}}\cdot\mathbf{F}\,. \tag{3.9}$$

The Lorentz force $\mathbf{F}_L \equiv -(\mathbf{E}+\mathbf{v}\times\mathbf{B})$ gives $\nabla_{\mathbf{p}}\cdot\mathbf{F}_L = 0$ identically thus $\nabla_{\mathbf{p}}\cdot\mathbf{F} = \nabla_{\mathbf{p}}\cdot\mathbf{F}_R$. Moreover, the distribution function $f(\mathbf{x},\mathbf{p},t)$ is always non-negative $f \geq 0$ thus the sign of dS/dt is given by $\nabla_{\mathbf{p}}\cdot\mathbf{F}_R$ solely.

From the expression of the LL force in Eq.(1.24) and using the following identities

$$\frac{\partial\gamma}{\partial p_i} = v_i \tag{3.10}$$

$$\frac{\partial v_j}{\partial p_i} = \frac{1}{\gamma}\Big(\delta_{ij} - v_i v_j\Big) \tag{3.11}$$

after a lengthy but straightforward calculation, we get

$$\nabla_{\mathbf{p}}\cdot\mathbf{F}_R \;=\; -\left(\frac{4\pi}{3}\frac{r_e}{\lambda}\right)\left\{\Big[\nabla_{\mathbf{x}}\cdot\mathbf{E} - \mathbf{v}\cdot\Big(\nabla_{\mathbf{x}}\times\mathbf{B} - \frac{\partial\mathbf{E}}{\partial t}\Big)\Big] + 2\Big[\frac{\mathbf{E}^2+\mathbf{B}^2}{\gamma}\Big] + 4\gamma\Big[\Big(\mathbf{v}\times\mathbf{E}\Big)^2 + \Big(\mathbf{v}\times\mathbf{B}\Big)^2 - 2\mathbf{v}\cdot\Big(\mathbf{E}\times\mathbf{B}\Big)\Big]\right\}. \tag{3.12}$$

[4]This can be shown in another way: if the right hand side of Eq.(3.4) is a regular function of $(f,\,t)$ such that it satisfies the hypothesis of the Picard theorem of existence and uniqueness of solutions of differential equations, then an initially positive f will always remain strictly positive as $f = 0$ is a solution of Eq.(3.4) and for the uniqueness two different solutions cannot meet in the plane $(f,\,t)$.

In a plasma, the kinetic equation is coupled with the Maxwell equations for the self-consistent fields

$$\nabla_{\mathbf{x}} \cdot \mathbf{E} = \frac{\rho}{\rho_c} = \frac{1}{n_c} \sum_{j=e,i} Z_j \int d^3p \, f_j(\mathbf{x}, \mathbf{p}, t) \tag{3.13}$$

$$\nabla_{\mathbf{x}} \times \mathbf{B} - \frac{\partial \mathbf{E}}{\partial t} = \frac{\mathbf{j}}{j_c} = \frac{1}{n_c c} \sum_{j=e,i} Z_j \int d^3p \, \mathbf{v} f_j(\mathbf{x}, \mathbf{p}, t), \tag{3.14}$$

where $\rho_c \equiv |e| n_c$, $j_c \equiv |e| n_c c$, $\int d^3q \, d^3p \, f_j(\mathbf{x}, \mathbf{p}, t) = N_j$ is the total number of particles for each species ($j = e$ electrons, $j = i$ ions) and Z_j is the charge of the particle species in units of $|e|$ (for electrons $Z_e = -1$). For a plasma, Eq.(3.12) can be recast as

$$\nabla_{\mathbf{p}} \cdot \mathbf{F}_R = -\left(\frac{4\pi}{3}\frac{r_e}{\lambda}\right) \Big\{ \Big[\frac{\rho}{\rho_c} - \mathbf{v} \cdot \frac{\mathbf{j}}{j_c}\Big] + 2\Big[\frac{\mathbf{E}^2 + \mathbf{B}^2}{\gamma}\Big] + 4\gamma \Big[\Big(\mathbf{v} \times \mathbf{E}\Big)^2 + \Big(\mathbf{v} \times \mathbf{B}\Big)^2 - 2\mathbf{v} \cdot \Big(\mathbf{E} \times \mathbf{B}\Big) \Big] \Big\}. \tag{3.15}$$

The terms of Eq.(3.15) proportional to the charge density ρ and to the current density $\mathbf{j}$ come from the term of the LL force (1.24) containing the derivatives of the fields. In general, these terms can give either a positive or negative contribution to $\nabla_{\mathbf{p}} \cdot \mathbf{F}_R$. The second term of Eq.(3.15) i.e. the term proportional to $(\mathbf{E}^2 + \mathbf{B}^2)$ has always a negative sign, its effect decreases with increasing electron energy and it is roughly γ^2 times smaller the third term. The third term of Eq.(3.15) comes from the strongly anisotropic 'friction' term of the LL force i.e. the term proportional to γ^2 in Eq.(1.24) and dominates in the ultra-relativistic limit $\gamma \gg 1$.

In appendix B we prove the following statement: for arbitrary fields and for any $\mathbf{v}$ such that $1 > |\mathbf{v}| \geq 0$ then

$$4\gamma \Big[\Big(\mathbf{v} \times \mathbf{E}\Big)^2 + \Big(\mathbf{v} \times \mathbf{B}\Big)^2 - 2\mathbf{v} \cdot \Big(\mathbf{E} \times \mathbf{B}\Big) \Big] + 2\Big[\frac{\mathbf{E}^2 + \mathbf{B}^2}{\gamma}\Big] \geq 0\,, \tag{3.16}$$

therefore according with Eqs. (3.9, 3.15), the terms of the LL force Eq. (1.24) that *do not* depend on the derivatives of the fields always lead to a *decrease* of the entropy i.e. to a *contraction* of the available phase space volume. In fact, the phase-space volume element J evolves according to $dJ/dt = J \, \nabla_{\mathbf{p}} \cdot \mathbf{F}_R$ (see appendix B.2 for a derivation of this equation). In a few special cases, the

effect of the terms of the LL force Eq.(1.24) that depend on the derivatives of the fields (i.e. the terms proportional to ρ and $\mathbf{j}$ in Eq.(3.15)) might lead to an expansion of the phase space volume. Anyway, their effect should be negligible compared to quantum effects as discussed in Ref. [11] and in section 1.2.1 and tends to vanish when the system is dominated by external fields i.e. collective fields are much smaller than external fields.

The physical interpretation of the above properties is that the RR force acts as a cooling mechanism for the system: part of the energy and momentum are radiated away and the spread in both momentum and coordinate space may be reduced. This prediction is confirmed by our PIC simulations (see chapter 5) where we found that RR effects lead to both an increased bunching in space and to a noticeable cooling of hot electrons.

It is instructive to discuss the contraction of the phase space in the special case of a small bunch of electrons interacting with a plane wave where collective fields are assumed to be negligible compared with the plane wave fields. Assuming an initial distribution $f = g(\mathbf{x})\,\delta^3(\mathbf{p}-\mathbf{p}_0)$, from Eqs.(3.9, 3.15) we have

$$\frac{dS(t)}{dt} = -\left(\frac{4\pi}{3}\frac{r_e}{\lambda}\right)\int d^3q\; g(\mathbf{x})\left\{2\left[\frac{\mathbf{E}^2+\mathbf{B}^2}{\gamma(\mathbf{p}_0)}\right] + \right.$$
$$\left. + 4\gamma(\mathbf{p}_0)\left[(\mathbf{v}_0\times\mathbf{E})^2 + (\mathbf{v}_0\times\mathbf{B})^2 - 2\mathbf{v}_0\cdot(\mathbf{E}\times\mathbf{B})\right]\right\}, \quad (3.17)$$

where $\mathbf{v}_0 = \mathbf{p}_0/\gamma(\mathbf{p}_0)$. If the electron bunch counter-propagates with the plane wave ($[\mathbf{v}_0\cdot(\mathbf{E}\times\mathbf{B})] < 0$) or propagates in the transverse direction ($[\mathbf{v}_0\cdot(\mathbf{E}\times\mathbf{B})] = 0$), from Eq.(3.17) it follows that RR leads to a contraction of the phase space. In particular, in the case of counter-propagation (using $|\mathbf{E}| = |\mathbf{B}|$, $\mathbf{E}\cdot\mathbf{B} = 0$) we have

$$\nabla_{\mathbf{p}}\cdot\mathbf{F}_R = -\,(4\pi r_e/3\lambda)\,4\mathbf{E}^2\left[2\gamma(\mathbf{p}_0)|\mathbf{v}_0|(1+|\mathbf{v}_0|) + 1/\gamma(\mathbf{p}_0)\right]. \quad (3.18)$$

On the other hand, if the bunch propagates in the same direction of the plane wave ($\mathbf{v}_0$ parallel to $\mathbf{E}\times\mathbf{B}$), then the contribution of the friction term (proportional to γ in Eq.(3.15)) becomes comparable with the contribution of the second term (proportional to $(\mathbf{E}^2+\mathbf{B}^2)$ in Eq.(3.15)) and we have

$$\nabla_{\mathbf{p}}\cdot\mathbf{F}_R = -\,(4\pi r_e/3\lambda)\left[4\mathbf{E}^2/(1+|\mathbf{v}_0|)^2\gamma^3(\mathbf{p}_0)\right] \quad (3.19)$$

which still leads to a contraction of the phase space but with a rate γ^4 smaller than the case of counter-propagation. This reinforces the evidence of the strongly *anisotropic* features of the LL force Eq.(1.24) as discussed in section 1.2.

Finally, we recall that Eq.(3.2) is more general than the usual collisionless kinetic equation (namely the Vlasov equation) but the PIC approach is still valid i.e. the PIC approach provides a solution for Eq.(3.2) and it is *not* limited to the Vlasov equation (see appendix B.3 for a derivation).

Chapter 4

Numerical approach

In this chapter we develop a compact algorithm that allows to include the RR force into existing PIC codes. We recall that in the PIC approach fields and computational particles[1] are advanced in time using a 'pusher' i.e. a numerical scheme to integrate the equations of motion. In fact, a 'pusher' is a numerical method to solve a system of first-order differential equations where derivatives are approximated with finite differences and differential equations are turned into algebraic equations. The classic, second order numerical accuracy, particle pusher is the 'leap-frog' algorithm. In this scheme positions and momenta are shifted in such a way that they 'leap-frog' over each other (see Fig. 4.1 for a sketch of a leap-frog advance); for example, the position is known at integer time steps and the velocity is known at integer plus half time steps (see Ref. [65] for further details). Leap-frog pushers are relatively simple compared to higher-order schemes, and most of all they are fast and require a minimal amount of storage memory while a good accuracy is retained.

The PIC method and leap-frog schemes are well-developed, well-tested and highly optimized numerical approaches for the study of many-body systems of charged particles subject to self-consistent fields i.e. a plasma. In the PIC approach each quasi-particle has to be advanced separately by the pusher, due to the large number of quasi-particles commonly used ($\gtrsim 10^6$), the particle pusher usually represents the most expensive part of the compu-

[1] We recall these computational particles provide a discrete representation of the continuous distribution function in the phase-space.

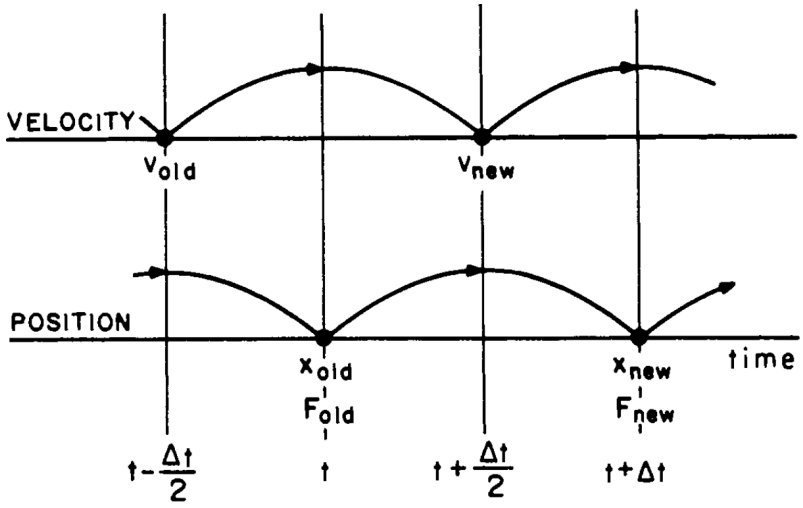

Figure 4.1: Sketch of leap-frog integration method. The two first-order differential equations $md\mathbf{v}/dt = \mathbf{F}$ and $d\mathbf{x}/dt = \mathbf{v}$ are replace by the finite-difference equations $m(\mathbf{v}_{\rm new} - \mathbf{v}_{\rm old})/\Delta t = \mathbf{F}_{\rm old}$ and $(\mathbf{x}_{\rm new} - \mathbf{x}_{\rm old})/\Delta t = \mathbf{v}_{\rm new}$. From Ref. [65].

tational cycle on which most efforts of optimization needs to be performed both to reduce the amount of data to be stored in memory and to improve the computational performance. In order to study RR effects in laser-plasma interactions, especially when multi-dimensional simulations are required, it is therefore crucial to look for an approach that is compatible with standard leap-frog schemes preserving their accuracy without requiring significant extra memory storage or computational effort. To this aim, we remark that the possibility to replace the full LL equation (1.24) with the reduced LL equation (1.25) as discussed in section 1.2 is greatly advantageous in PIC simulations. Indeed, the 'derivative' term in the full LL equation (1.24) does not lead to significant extra computational effort when the fields are given known functions of the position and time such as in the case of an electron in an external plane wave but a noticeable extra computational effort is required when they have to be calculated self-consistently. In fact, in PIC simulations fields are defined on a fixed grid, derivatives of the fields have therefore to be calculated using the value of fields on multiple grid-points in

order to approximate the derivative with the required numerical accuracy. In particular, time derivatives are challenging since the fields at least one step forward in time have to be estimated to approximate the time derivative with an acceptable accuracy.

In the following, we introduce our modular approach that allows to include RR effects without changing the existing leap-frog schemes for the Lorentz force and field advance, then simulations of a single electron in a plane wave are used as a testing bench comparing the numerical result with the exact analytical solution discussed in section 2.2 and with a fourth-order Runge-Kutta approach. This is a necessary check in order to be confident in the results of our PIC simulations of laser-plasma interaction where we do not have an analytical benchmark.

4.1 A modular leap-frog pusher

We briefly recall some basic concepts of a leap-frog pusher. If we consider a smooth function $p(t)$ of a parameter t, using a Taylor expansion we have

$$p\left(t_0 \pm \frac{\Delta}{2}\right) = p(t_0) \pm \left.\frac{dp(t)}{dt}\right|_{t_0} \frac{\Delta}{2} + \frac{1}{2} \left.\frac{d^2p(t)}{dt^2}\right|_{t_0} \frac{\Delta^2}{4} + \mathcal{O}(\Delta^3) \tag{4.1}$$

therefore

$$p\left(t_0 + \frac{\Delta}{2}\right) - p\left(t_0 - \frac{\Delta}{2}\right) = \left.\frac{dp(t)}{dt}\right|_{t_0} \Delta + \mathcal{O}(\Delta^3)\,. \tag{4.2}$$

Thus, a first order differential equation

$$\frac{dp(t)}{dt} = f(t) \tag{4.3}$$

can be approximated with

$$p\left(t_0 + \frac{\Delta}{2}\right) - p\left(t_0 - \frac{\Delta}{2}\right) = f\left(t_0\right)\Delta + \mathcal{O}(\Delta^3) \tag{4.4}$$

or, using a simpler notation, starting with $p(t_0 - \Delta/2) = p^{n-1/2}$ we can get $p(t_0 + \Delta/2) = p^{n+1/2}$ up to an error of order $\mathcal{O}(\Delta^3)$ if $f(t_0) = f^n$ and the step Δ are known. The generalization to a system of first order differential

equations is straightforward. Since $N = (t - t_0)/\Delta$ steps are required to reach a fixed time t from time t_0 then the *global* error after N steps is $\mathcal{O}(\Delta^2)$ and the leap-frog is a second order accuracy method.

In our approach, the key idea is to exploit the superposition property of the force that allows to write the *total* force by vectorial addition of the Lorentz and RR force. In fact, supposing that the total force $\mathbf{f}_T$ is the sum of two forces $\mathbf{f}_1$ and $\mathbf{f}_2$

$$\mathbf{f}_T = \mathbf{f}_1 + \mathbf{f}_2 \tag{4.5}$$

then the full equation of motion is

$$\frac{d\mathbf{p}_T}{dt} = \mathbf{f}_T = \mathbf{f}_1 + \mathbf{f}_2 \tag{4.6}$$

and the full leap-frog step is

$$\frac{\mathbf{p}_T^{n+1/2} - \mathbf{p}_T^{n-1/2}}{\Delta t} = \mathbf{f}_T^n = \mathbf{f}_1^n + \mathbf{f}_2^n \tag{4.7}$$

We consider the following set of equations of motion where only one of the two forces works

$$\begin{cases} \frac{d\mathbf{p}_1}{dt} = \mathbf{f}_1 \\ \frac{d\mathbf{p}_2}{dt} = \mathbf{f}_2 \end{cases} \longrightarrow \begin{cases} \frac{\mathbf{p}_1^{n+1/2} - \mathbf{p}_1^{n-1/2}}{\Delta t} = \mathbf{f}_1^n \\ \frac{\mathbf{p}_2^{n+1/2} - \mathbf{p}_2^{n-1/2}}{\Delta t} = \mathbf{f}_2^n \end{cases} \tag{4.8}$$

If in the full (4.7) and partial (4.8) leap-frog equations we start with the same initial condition $\mathbf{p}^{n-1/2} \equiv \mathbf{p}_T^{n-1/2} = \mathbf{p}_1^{n-1/2} = \mathbf{p}_2^{n-1/2}$ then the two partial leap-frog equations (4.8) become

$$\begin{cases} \mathbf{p}_1^{n+1/2} - \mathbf{p}^{n-1/2} = \mathbf{f}_1^n \Delta t \\ \mathbf{p}_2^{n+1/2} - \mathbf{p}^{n-1/2} = \mathbf{f}_2^n \Delta t \end{cases} \tag{4.9}$$

Then, we sum the two partial leap-frog equations (4.9) getting

$$\mathbf{p}_1^{n+1/2} + \mathbf{p}_2^{n+1/2} - 2\mathbf{p}^{n-1/2} = (\mathbf{f}_1^n + \mathbf{f}_2^n)\Delta t \tag{4.10}$$

while the full leap-frog equation (4.7) becomes

$$\mathbf{p}_T^{n+1/2} - \mathbf{p}^{n-1/2} = \mathbf{f}_T^n \Delta t = (\mathbf{f}_1^n + \mathbf{f}_2^n)\Delta t \tag{4.11}$$

Therefore, by comparing the equation (4.10) with equation (4.11) we get for the *full* leap-frog step

$$\mathbf{p}_T^{n+1/2} = \mathbf{p}_1^{n+1/2} + \mathbf{p}_2^{n+1/2} - \mathbf{p}^{n-1/2} \tag{4.12}$$

This means, starting at time t^n and position $\mathbf{x}^n$ with $\mathbf{p}^{n-1/2}$, first advance $\mathbf{p}^{n-1/2}$ to $\mathbf{p}_1^{n+1/2}$ by $\mathbf{f}_1^n$ alone. Then advance *independently* $\mathbf{p}^{n-1/2}$ to $\mathbf{p}_2^{n+1/2}$ by $\mathbf{f}_2^n$ alone and finally use equation (4.12) to get the full leap-frog step $\mathbf{p}_T^{n+1/2}$. The generalization of (4.12) to i forces $\mathbf{f}_T = \mathbf{f}_1 + \ldots + \mathbf{f}_i$ is straightforward

$$\mathbf{p}_T^{n+1/2} = \mathbf{p}_1^{n+1/2} + \ldots + \mathbf{p}_i^{n+1/2} - (i-1)\mathbf{p}^{n-1/2} \tag{4.13}$$

Using (4.9) we can recast (4.12) as

$$\mathbf{p}_T^{n+1/2} = \mathbf{p}_1^{n+1/2} + \mathbf{f}_2^n \Delta t = \mathbf{p}_2^{n+1/2} + \mathbf{f}_1^n \Delta t \tag{4.14}$$

In principle, the previous algorithm allows us to keep our current leap-frog pusher for the Lorentz force and to develop an independent pusher for the RR force alone. However, since our forces depend on the momentum of the particle, an estimate of the momentum at half-step is needed to compute the forces at half-step (i.e $\mathbf{f}_1^n$ and $\mathbf{f}_2^n$). Assuming that the RR force $\mathbf{f}_R$ is a perturbation to the electron motion, we can use the Lorentz force $\mathbf{f}_L$ to estimate the velocity and momentum at half time-step and evaluate the RR force directly using the estimated momentum. According to the previous assumption, the initial momentum $\mathbf{p}^{n-1/2}$ is advanced to $\mathbf{p}_L^{n+1/2}$ using our existing pusher for the Lorentz force[2]. Then $\mathbf{p}_L^{n+1/2}$ is used to estimate the *total* momentum $\mathbf{p}^n$ and velocity $\mathbf{v}^n$ at half time step

$$\mathbf{p}^n \approx \frac{\mathbf{p}_L^{n+1/2} + \mathbf{p}^{n-1/2}}{2} \tag{4.15}$$

$$\mathbf{v}^n \approx \frac{\mathbf{p}^n}{\gamma^n} \tag{4.16}$$

where

$$\gamma^n = \sqrt{1 + (\mathbf{p}^n)^2} \tag{4.17}$$

[2]We implemented our numerical algorithm into existing PIC codes where the Boris particle pusher is used (see appendix A) and therefore the Boris particle pusher is used in our single electron simulations.

Next Eqs. (4.15-4.17) are used together with the fields $\mathbf{E}^n$, $\mathbf{B}^n$ and their derivatives at half time-step to compute the estimate of the RR force at half-step $\mathbf{f}_R^n$. This task is particularly simple because many terms of $\mathbf{f}_R$ such as the friction term can be written using $\mathbf{f}_L$ directly. In fact, the full[3] dimensionless LL equation (1.24) can be written in a more concise way as

$$\frac{d\mathbf{p}}{dt} = \mathbf{f}_L + \left(\frac{4}{3}\pi\frac{r_e}{\lambda}\right)\Big[\mathbf{g}_1 + \mathbf{g}_2 + \mathbf{g}_3\Big] \tag{4.18}$$

where

$$\mathbf{f}_L = -\Big(\mathbf{E} + \mathbf{v}\times\mathbf{B}\Big) \tag{4.19}$$

$$\mathbf{g}_1 = -\gamma\Big[\Big(\frac{\partial}{\partial t} + \mathbf{v}\cdot\nabla\Big)\mathbf{E} + \mathbf{v}\times\Big(\frac{\partial}{\partial t} + \mathbf{v}\cdot\nabla\Big)\mathbf{B}\Big] \tag{4.20}$$

$$\mathbf{g}_2 = \Big[-\mathbf{f}_L\times\mathbf{B} + (\mathbf{v}\cdot\mathbf{E})\mathbf{E}\Big] \tag{4.21}$$

$$\mathbf{g}_3 = -\gamma^2\Big[\mathbf{f}_L^2 - (\mathbf{v}\cdot\mathbf{E})^2\Big]\mathbf{v} \tag{4.22}$$

Finally, recalling that $\mathbf{f}_L^n$ is

$$\mathbf{f}_L^n = \frac{\mathbf{p}_L^{n+1/2} - \mathbf{p}^{n-1/2}}{\Delta t} \tag{4.23}$$

we apply (4.14) to compute $\mathbf{p}_T^{n+1/2}$ using $\mathbf{p}_L^{n+1/2}$ and

$$\mathbf{f}_R^n = \left(\frac{4}{3}\pi\frac{r_e}{\lambda}\right)\Big[\mathbf{g}_1^n + \mathbf{g}_2^n + \mathbf{g}_3^n\Big] \tag{4.24}$$

$$\mathbf{g}_1^n = -\gamma^n\Big[\Big(\frac{\partial}{\partial t} + \mathbf{v}^n\cdot\nabla\Big)\mathbf{E}^n + \mathbf{v}^n\times\Big(\frac{\partial}{\partial t} + \mathbf{v}^n\cdot\nabla\Big)\mathbf{B}^n\Big] \tag{4.25}$$

$$\mathbf{g}_2^n = \Big[-\mathbf{f}_L^n\times\mathbf{B}^n + (\mathbf{v}^n\cdot\mathbf{E}^n)\mathbf{E}^n\Big] \tag{4.26}$$

$$\mathbf{g}_3^n = -(\gamma^n)^2\Big[(\mathbf{f}_L^n)^2 - (\mathbf{v}^n\cdot\mathbf{E}^n)^2\Big]\mathbf{v}^n \tag{4.27}$$

where we used the expressions (4.15 - 4.17) and (4.23).

[3] In our single particle tests, we used the full LL equation (1.24) in order to compare the results with the analytical solution. However, further tests confirmed that the contribution of both the term of the LL force that depends on the derivatives of the fields (i.e. $\mathbf{g}_1$) and of the term that does not depend on γ^2 (i.e. $\mathbf{g}_2$) is negligible to all practical purposes on relevant simulation time scales (hundreds of time periods).

Summarizing, assuming that the RR force is a perturbation to the Lorentz force, first the full leap-frog step advance is split into two step advances due to the Lorentz and RR force *separately*; then the RR force is computed directly using the unperturbed momentum due to the Lorentz force alone as an estimate of the full momentum at half-step. This keeps the numerical code simple and fast while both a good numerical accuracy (see our tests in next section) and the existing code developed for the Lorentz force are retained.

4.2 Tests and results

In order to test our numerical approach, we performed several simulations of a single electron in a monochromatic plane wave with a wide range of physical parameters such as polarization parameter δ (see 2.16), normalized laser amplitude a_0 and initial electron momentum $\mathbf{p}_0$ comparing the numerical with the analytical result. In our simulations, we used a $\omega^{-1}/100$ timestep and a run time of $500\,\omega^{-1}$. We summarize here our main conclusions

- Neither a large initial value of the ratio between the modulus of the RR force $|\mathbf{f}_R|$ and the modulus of the Lorentz force $|\mathbf{f}_L|$ nor a large value of the RR parameter R (see (2.27)) yield a significant discrepancy between the numerical prediction and the analytical solution. Simulations with an initial $|\mathbf{f}_R|$ to $|\mathbf{f}_L|$ ratio of the order of $|\mathbf{f}_R|/|\mathbf{f}_L| \gtrsim 1140$ or RR parameter up to $R \sim 68$ were performed with very good agreement between the numerical and the analytical prediction (see Figs. 4.2 - 4.5).

  Figure 4.2 shows a plot of the longitudinal momentum p_x as a function of the phase $\phi = \omega(t - x(t)/c)$ for an electron with initial momentum $p_{x_0} = -200\,mc$ interacting with a plane wave of intensity $I \sim 2.6 \times 10^{23}\,\mathrm{W\,cm^{-2}}$. In this case $|\mathbf{f}_R|/|\mathbf{f}_L| \sim 0.4$ initially and $R \sim 0.72$, the agreement between the numerical prediction and the analytical solution is excellent. Figure 4.3 shows a comparison of the trajectories obtained using a fourth-order Runge-Kutta and our leap-frog pusher with the same physical and numerical parameters of Figure 4.2, the relative difference is of the order of 10^{-4}.

Figures 4.4 and 4.5 show the longitudinal momentum p_x as a function of the phase $\phi = \omega(t - x(t)/c)$ for an electron with initial momentum $p_{x_0} = -5000\, mc$ and $p_{x_0} = -9000\, mc$ respectively. In figure 4.4 the intensity of the plane wave is $I \sim 10^{24}\,\mathrm{W\,cm^{-2}}$, the initial ratio of the RR to the Lorentz force is $|\mathbf{f}_R|/|\mathbf{f}_L| \sim 501$ and the RR parameter is $R \sim 68$ while in figure 4.5 the intensity of the plane wave is $I \sim 5 \times 10^{23}\,\mathrm{W\,cm^{-2}}$, the initial ratio of the RR to the Lorentz force is $|\mathbf{f}_R|/|\mathbf{f}_L| \sim 1147$ and the RR parameter is $R \sim 61$. In both cases the agreement between the numerical and the analytical solution is good even though the dynamics is dominated by the RR force.

- Our tests have shown that our approach to the inclusion of the RR force into a numerical code provides reliable results even when the RR force is not small compared to the Lorentz force. We provide an heuristic argument to explain such good agreement:

  1. As a consequence of the smallness of the ratio between the effective electron radius and the typical laser wavelength ($4\pi r_e/3\lambda \sim 10^{-8}$), the terms $\mathbf{g}_1$ (Eq. (4.20)) and $\mathbf{g}_2$ (Eq. (4.21)) are much smaller than the Lorentz force (Eq. (4.19)) in the classical framework. For these terms of the RR force a perturbative approach is always suitable in the classical framework.

  2. The dominant friction-like term $\mathbf{g}_3$ (Eq. (4.22)) is directed along the velocity $\mathbf{v}$. This implies that, at a given time, the effect of the friction-like term amounts to a change of the modulus of the momentum $|\mathbf{p}|$ without changing its direction.

  3. Since the friction-like term $\mathbf{g}_3$ (Eq. (4.22)) is large only for ultra-relativistic electrons $\gamma \gg 1$ and $|\mathbf{p}| \sim \gamma$ for $\gamma \gg 1$, in the cases when the friction term $\mathbf{g}_3$ is large, the variation of the modulus of the momentum due to $\mathbf{g}_3$ is approximately equal to the variation of the electron energy due to $\mathbf{g}_3$.

  4. If the *percentage* of variation of the modulus of the momentum, or equivalently the percentage of variation of the energy, due to the friction-like term $\mathbf{g}_3$ is small in a single leap-frog step $\Delta = \omega^{-1}/N$

i.e.

$$\left|\frac{\Delta}{\gamma}\left.\frac{d\gamma}{dt}\right|_{\mathbf{g}_3}\right| \ll 1 \tag{4.28}$$

then the momentum at half-step can be estimated self-consistently neglecting the contribution of the friction-like term $\mathbf{g}_3$ i.e. using Eq. (4.15) although $\mathbf{g}_3$ is not small compared to the Lorentz force.

5. Taking the scalar product of Eq.(4.22) and $\mathbf{v}$ and using $\mathbf{v}^2 = 1 - 1/\gamma^2$ we have (normalized units)

$$\left.\frac{d\gamma}{dt}\right|_{\mathbf{g}_3} \simeq -\left(\frac{4\pi r_e}{3\lambda}\right)\gamma^2\Big[\Big(\mathbf{E}+\mathbf{v}\times\mathbf{B}\Big)^2 - (\mathbf{v}\cdot\mathbf{E})^2\Big] \tag{4.29}$$

and therefore the percentage of variation of the energy in a single step due to $\mathbf{g}_3$ is

$$\left|\frac{\Delta}{\gamma}\left.\frac{d\gamma}{dt}\right|_{\mathbf{g}_3}\right| \simeq \frac{1}{N}\left(\frac{4\pi r_e}{3\lambda}\right)\gamma\Big[\Big(\mathbf{E}+\mathbf{v}\times\mathbf{B}\Big)^2 - (\mathbf{v}\cdot\mathbf{E})^2\Big] \tag{4.30}$$

which is at most

$$\left|\frac{\Delta}{\gamma}\left.\frac{d\gamma}{dt}\right|_{\mathbf{g}_3}\right| \lesssim \frac{1}{N}\left(\frac{4\pi r_e}{3\lambda}\right)\gamma(\mathbf{E}^2+\mathbf{B}^2) \tag{4.31}$$

and assuming $N \sim 100$, $\lambda \sim 1\,\mu$m, $\gamma \sim |\mathbf{E}| \sim |\mathbf{B}| \sim 300$ then $(4\pi r_e/3\lambda N)\,\gamma(\mathbf{E}^2+\mathbf{B}^2) \sim 6\times 10^{-3}$.

In conclusion, our perturbative approach turns out to be suitable even when the RR force is not small compared to the Lorentz force because the *percentage* of variation of the momentum due to the RR force in a single leap-frog step is small and therefore the full momentum at half-step can be approximated self-consistently with the momentum at half-step obtained neglecting the RR force i.e. using Eqs. (4.15 - 4.17). An analogous estimate of the percentage of variation of the momentum in a single step for the Lorentz force leads to

$$\left|\frac{\Delta}{\gamma}\left.\frac{d\mathbf{p}}{dt}\right|_{\mathbf{f}_L}\right| \lesssim \frac{1}{N}\sqrt{\frac{\mathbf{E}^2+\mathbf{B}^2}{2\gamma^2}} \tag{4.32}$$

For $\gamma \sim |\mathbf{E}| \sim |\mathbf{B}|$ then $\left|(\Delta/\gamma)\,d\mathbf{p}/dt|_{\mathbf{f}_L}\right| \sim 1/N$ but if the electron energy is much smaller than the normalized field strength i.e. $|\mathbf{E}| \gg \gamma$ then the

percentage of variation of the momentum in a single timestep is large and may lead to a significant deviation from the exact solution. For instance, in Fig. 4.6 the numerical and the analytical prediction (both without RR effects) of the longitudinal momentum p_x as a function of the phase ϕ are compared for an electron initially at rest interacting with a plane wave of intensity $I \sim 10^{23}\,\mathrm{W\,cm^{-2}}$. It is found that using a time-step $\omega^{-1}/100$, the standard Boris particle pusher lead to a significant deviation from the analytical solution according with the estimate (4.32). However, in this case the electron is initially at rest while the fields are at their maximum $a_0 = 215$; in realistic simulations fields grow smoothly and electrons gain energy gradually so that $\left|(\Delta/\gamma)\, d\mathbf{p}/dt|_{\mathbf{f}_L}\right| \lesssim 1/N$ and the numerical prediction traces the exact solution.

Our tests confirmed that the inclusion of the RR force according to our approach preserves the accuracy and stability of the (unmodified) particle pusher for the Lorentz force (the standard Boris particle pusher in our code). Finally, we remark that this approach to the inclusion of the RR force have led to a less than 10% increment of the computing time compared to the case without RR in our PIC simulations reported in chapter 5. As discussed above, this relatively modest increase of the computational time may be crucial to perform large scale PIC simulations with RR effects included.

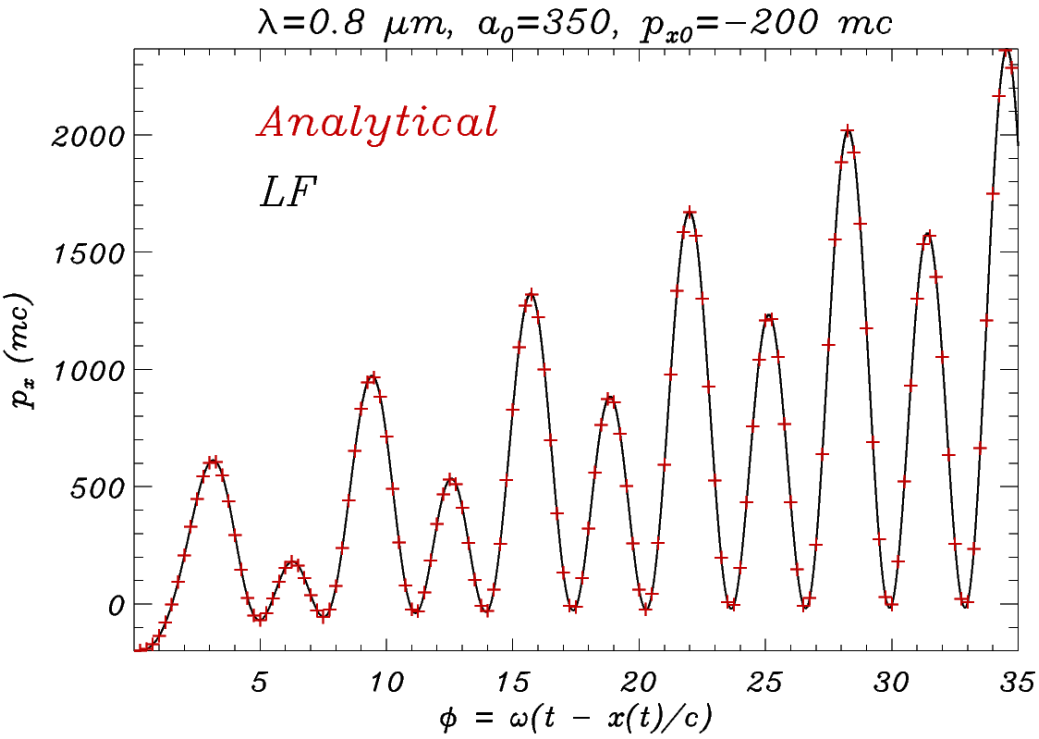

Figure 4.2: Plot of p_x as a function of the phase ϕ for an electron with initial momentum $p_{y_0} = p_{z_0} = 0$ and $p_{x_0} = -200\,mc$ interacting with a monochromatic linearly polarized plane wave with normalized amplitude $a_0 = 350$ and wavelength $\lambda = 0.8\,\mu$m (corresponding to an intensity $I \sim 2.6{\times}10^{23}\,\mathrm{W\,cm^{-2}}$). The black curve reports the numerical result obtained with our leap-frog pusher with the RR force included while the red crosses report the analytical solution. The initial ratio of the modulus of RR force to the modulus of the Lorentz force is $|\mathbf{f}_R|/|\mathbf{f}_L| \sim 0.4$, the RR parameter (see (2.27)) is $R \sim 0.72$, the time-step is $\omega^{-1}/100$, the run time is $500\omega^{-1}$, the polarization parameter (see (2.16)) is $\delta = 1$ and the electron is initially located at $x = 0$.

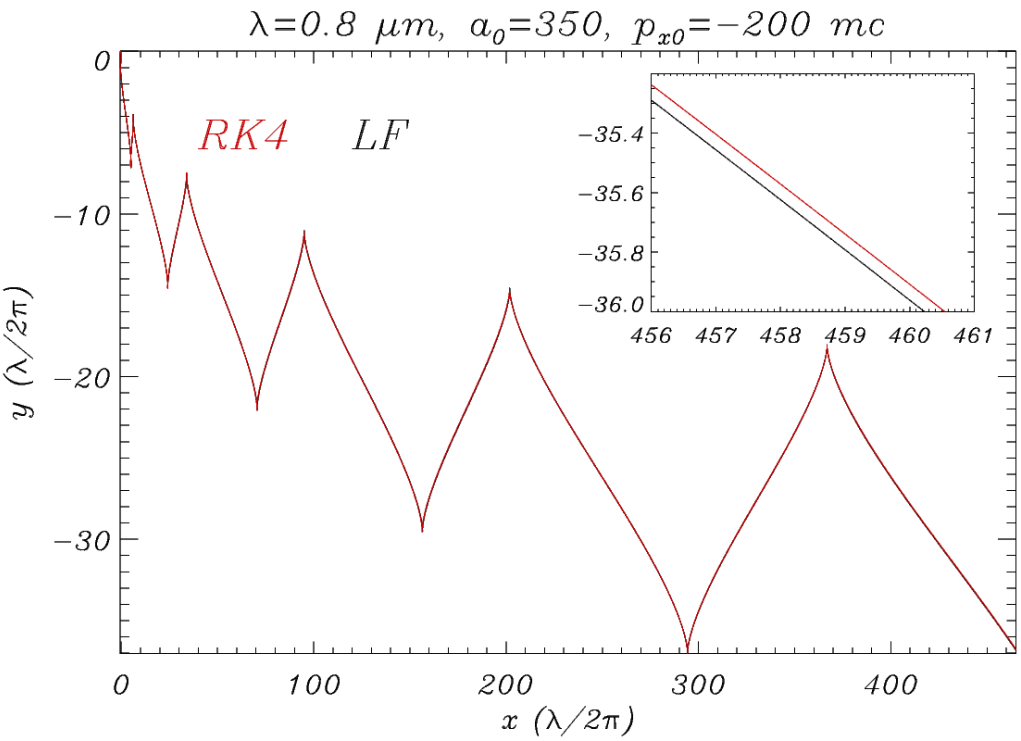

Figure 4.3: Comparison of single electron trajectories with RR in the (x, y) plane obtained with a fourth-order Runge-Kutta method (red curve) and our leap-frog method (black curve). The physical and numerical parameters are the same of the case reported in Fig.(4.2). A zoom of a small region of the trajectory in the lower-right corner of the plot is also reported.

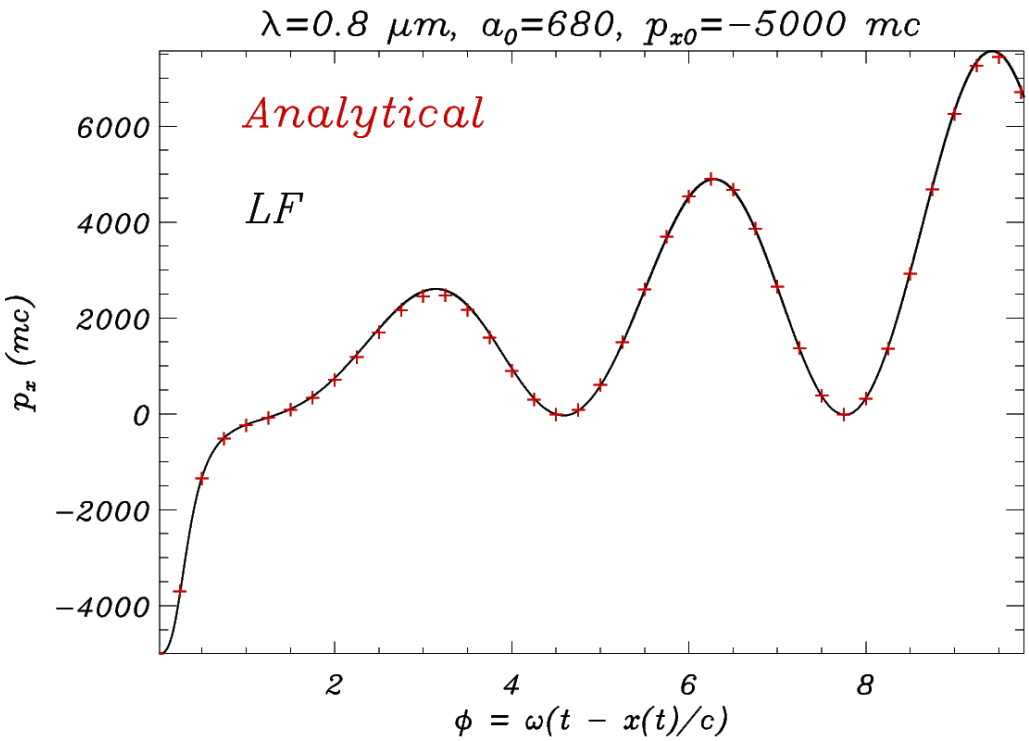

Figure 4.4: Plot of p_x as a function of the phase ϕ for an electron with initial momentum $p_{y_0} = p_{z_0} = 0$ and $p_{x_0} = -5000\, mc$ interacting with a monochromatic linearly polarized plane wave with normalized amplitude $a_0 = 680$ and wavelength $\lambda = 0.8\,\mu$m (corresponding to an intensity $I \sim 10^{24}\,\mathrm{W\,cm^{-2}}$). The black curve reports the numerical result obtained with our leap-frog pusher with the RR force included while the red crosses report the analytical solution. The initial ratio of the modulus of RR force to the modulus of the Lorentz force is $|\mathbf{f}_R|/|\mathbf{f}_L| \sim 501$, the RR parameter (see (2.27)) is $R \sim 68$, the time-step is $\omega^{-1}/100$, the run time is $500\omega^{-1}$, the polarization parameter (see (2.16)) is $\delta = 1$ and the electron is initially located at $x = 0$.

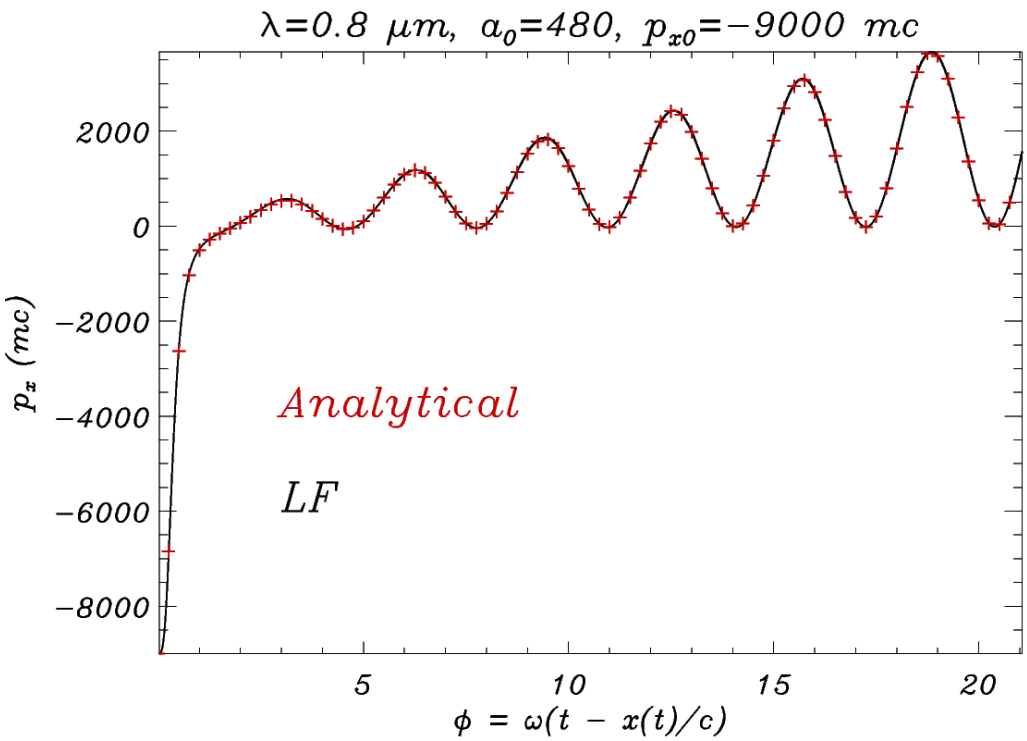

Figure 4.5: Plot of p_x as a function of the phase ϕ for an electron with initial momentum $p_{y_0} = p_{z_0} = 0$ and $p_{x_0} = -9000\, mc$ interacting with a monochromatic linearly polarized plane wave with normalized amplitude $a_0 = 480$ and wavelength $\lambda = 0.8\,\mu$m (corresponding to an intensity $I \sim 5 \times 10^{23}\,\mathrm{W\,cm^{-2}}$). The black curve reports the numerical result obtained with our leap-frog pusher with the RR force included while the red crosses report the analytical solution. The initial ratio of the modulus of RR force to the modulus of the Lorentz force is $|\mathbf{f}_R|/|\mathbf{f}_L| \sim 1147$, the RR parameter (see (2.27)) is $R \sim 61$, the time-step is $\omega^{-1}/100$, the run time is $500\omega^{-1}$, the polarization parameter (see (2.16)) is $\delta = 1$ and the electron is initially located at $x = 0$.

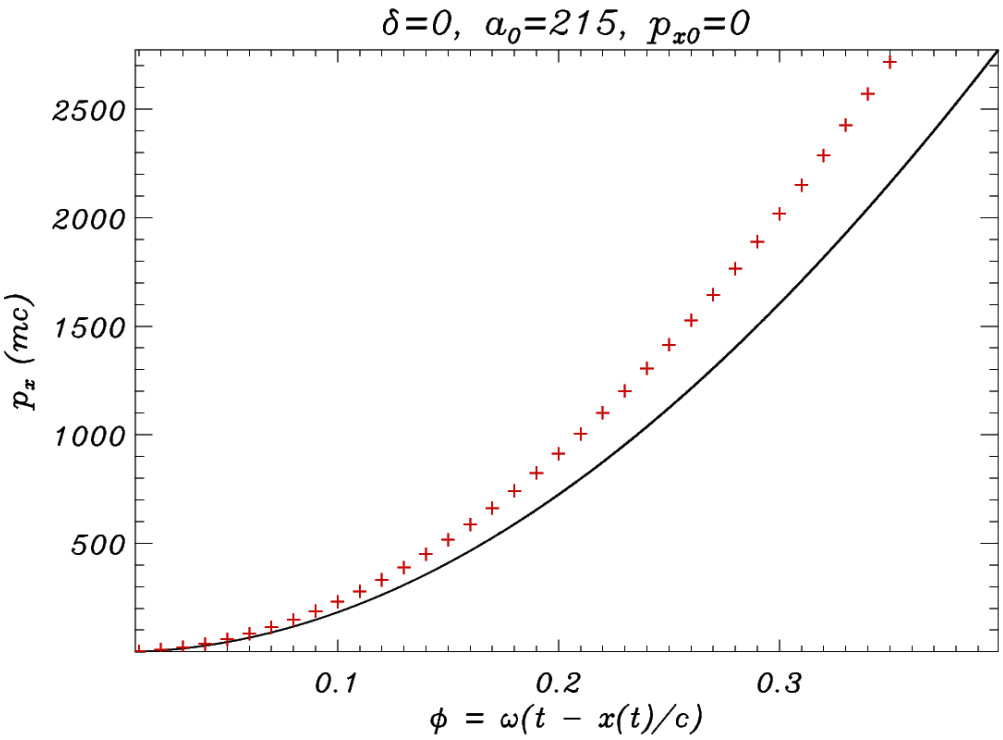

Figure 4.6: Plot of p_x as a function of the phase ϕ for an electron with initial momentum $\mathbf{p} = 0$ interacting with a monochromatic linearly polarized plane wave with polarization parameter $\delta = 0$ (see (2.16)) and normalized amplitude $a_0 = 215$ (corresponding to an intensity $I \sim 10^{23}\,\mathrm{W\,cm^{-2}}$ for $\lambda = 0.8\,\mu\mathrm{m}$). In this example, the time-step is $\omega^{-1}/100$, the run time is $300\omega^{-1}$ and the electron is initially located at $x = 0$. The black curve reports the numerical result obtained with the standard Boris particle pusher for the Lorentz force (the RR force is switched off) while the red crosses report the analytical solution. In this case the electron is initially at rest $\gamma = 1$ while the fields are at their maximum $a_0 = 215$ and the deviation from the analytical solution is large according with the estimate (4.32).

Chapter 5

Simulations of radiation pressure dominated acceleration

In this chapter, RR effects on ion acceleration in the interaction of a superintense laser pulse ($I \gtrsim 10^{23}\,\mathrm{W\,cm^{-2}}$) with a thin plasma foil ($\ell \lesssim \lambda$) in the radiation pressure dominated acceleration (RPDA) regime are investigated with multi-dimensional particle-in-cell (PIC) simulations.

The radiation pressure dominated regime

Before proceeding any further, it may be useful to briefly recall some basic concepts of ion acceleration in the RPDA regime as well as some of its foreseen appealing features (see the recent review [8] for details). It is known that an electromagnetic wave carries momentum which can be exchanged with either a reflecting or absorbing medium leading to an effective radiation pressure. Radiation pressure acceleration of a thin foil may be essentially described as a light mirror or light 'sail' boosted by an electromagnetic wave; this model is indeed customary named the "light sail" model (see Ref. [57]). In the case of a plane wave normally incident on a flat surface, radiation pressure physically arises from the cycle-averaged value of the non-linear magnetic term of the Lorentz force $e(\mathbf{v}/c \times \mathbf{B})$. The effect of the magnetic term can be *qualitatively* described using a simple perturbative approach

and recalling that for a plasma with density n much higher than the critical density n_c the penetration of an electromagnetic wave into the plasma is limited to a skin layer of thickness of the order of the skin depth $\delta = c/\omega_p$. Considering an elliptically polarized electromagnetic wave normally incident on a plasma slab with a step profile, the vector potential inside the plasma can be approximated as (see Ref. [55])

$$\mathbf{A}(x,t) = \frac{A_0}{\sqrt{1+\epsilon^2}} e^{-x/d_s} \left(\hat{\mathbf{y}}\cos(\omega t) + \epsilon\hat{\mathbf{z}}\sin(\omega t)\right) \tag{5.1}$$

where $d_s = c/\sqrt{\omega_p^2 - \omega^2}$ and $0 \leq \epsilon \leq 1$. Using $\mathbf{B} = \nabla \times \mathbf{A}$ and neglecting relativistic effects, the transverse velocity is $\mathbf{v}_T = -e\mathbf{A}/mc$ and the longitudinal component of the $f_x = e\mathbf{v}_T/c \times \mathbf{B}$ force is estimated as

$$f_x = f_0 e^{-2x/d_s} \left(1 + \frac{1-\epsilon^2}{1+\epsilon^2}\cos(2\omega t)\right) \tag{5.2}$$

where $f_0 = e^2 A_0^2/2d_s mc^2$ (see Ref. [55] or Ref. [8] and references therein). The integral over x of the electron density n times the cycle-averaged magnetic force $\langle f_x \rangle$ is customary called the ponderomotive force and gives the total radiation pressure on the surface.

The force f_x mainly operates on electrons due to their higher charge to mass ratio. The effect of this force is to push electrons inside the plasma generating a charge separation and consequently an electrostatic field E_x. In a steady state, the ponderomotive force on electrons is balanced by the averaged electrostatic field $\langle E_x \rangle$ due to the charge separation so that $\langle f_x \rangle = e\langle E_x \rangle$. The steady electrostatic field $\langle E_x \rangle$ accelerates ions so that the momentum of the impinging wave is mostly transferred to ions due to their higher mass, even though radiation pressure operates on electrons. We mention that if the electromagnetic wave interacts with a plasma foil with thickness ℓ comparable or smaller than the laser wavelength λ then the penetration of the laser pulse into the plasma depends also on the foil thickness. In the case of a delta-like density profile, the transmission and reflection coefficients can be calculated analytically [56]. This simple model may be useful to describe ultra-thin foils where the thickness is a small fraction of the laser wavelength, in this cases the foil is transparent when $a_0 > \zeta$ where $\zeta = \pi n\ell/n_c\lambda$ is the normalized surface density [56].

Eq. (5.2) illustrates the differences between circular and linear polarization of the electromagnetic wave. In fact, for circular polarization $\epsilon = 1$ and the 2ω frequency term vanishes in Eq. (5.2); in this case only the steady component i.e. the ponderomotive term of the longitudinal force f_x is present. In the case of linear polarization $\epsilon = 0$ and the 2ω term of the force f_x in Eq. (5.2) coupled with the longitudinal electric field generated by the charge separation drives strong density oscillations at the surface. Since the laser pulse cannot penetrate much into a solid-density target, the energy absorbed at the surface due to such oscillations is then transferred into inner regions by 'fast' electrons i.e. electrons with energies of the order or beyond the normalized laser amplitude $\gamma \gtrsim a_0$ ($a_0 \gg 1$). It has become customary to name such mechanism of fast electron generation due to the oscillating component of f_x as the $\mathbf{J} \times \mathbf{B}$ heating mechanism.

We mention that in the so called Target Normal Sheath Acceleration (TNSA) model, ion acceleration is driven by the space-charge field generated at the rear surface of the target by fast electrons generated at the front surface and then attempting to escape in vacuum from the rear side (see Ref. [8] for details). For a linearly polarized laser pulse normally incident on a plasma slab, the TNSA acceleration mechanism and the radiation pressure acceleration mechanism are therefore simultaneously present and radiation pressure acceleration dominates only at ultra-high intensities $I > 10^{23}\,\mathrm{W\,cm^{-2}}$ (see Ref. [19]). The qualitative prediction from Eq. (5.2) therefore suggests that a 'pure' radiation pressure acceleration regime requires normal incidence and the use of circularly polarized electromagnetic waves in order to suppress the electron heating due to the 2ω component of the $\mathbf{J} \times \mathbf{B}$ force. The strong suppression of the longitudinal oscillations in the case of circularly polarized laser pulses was confirmed with PIC simulations. In fact, PIC simulations have shown that the use of circular polarization instead of linear polarization and normal incidence quenches the generation of high-energy electrons and leads to a steady acceleration [54, 58, 59, 60].

In 2004, Esirkepov *et al.* suggested that radiation pressure may efficiently drive the acceleration of a thin plasma foil yielding a quasi-monoenergetic spectrum in contrast with other previously studied mechanisms such as TNSA where the spectrum is typically very broad. In fact, using a three-dimensional

PIC simulation Esirkepov *et al.* have shown that at intensities exceeding $10^{23}\,\mathrm{W\,cm^{-2}}$ and for linear polarization the radiation pressure of a laser pulse can accelerate a thin foil nearly as a whole with a gain in kinetic energy that agrees with the prediction obtained modeling the foil as a perfectly reflecting mirror boosted by the radiation pressure of the laser pulse. In Fig. 5.1 the peak of the ion kinetic energy as a function of time is compared with the prediction of the "light sail" model (see Ref. [19]) showing a fair agreement. Indeed, such agreement between the "light sail" model and the PIC simulation data was used to infer that at intensities exceeding $I \gtrsim 10^{23}\,\mathrm{W\,cm^{-2}}$ the radiation pressure dominates the acceleration. The light sail model allows to deduce the relevant scaling laws for given laser and plasma parameters as well as to choose such laser and plasma parameters for 'optimal' acceleration [57, 56]. In particular, a linear scaling with the laser pulse intensity, an high efficiency in the relativistic limit and quasi-monoenergetic features in the ion energy spectrum are expected (see [57, 56]). These promising features as well as the foreseen possibility to accelerate a large number of ions up to energies of the order of several hundred of MeVs per nucleon make the RPDA regime very appealing for applications such as hadron therapy and have stimulated a steadily growing interest (see the review [8]).

RR effects on radiation pressure acceleration

According to Ref. [19], radiation pressure becomes the dominant mechanism of ion acceleration when the laser intensity is $I > 10^{23}\,\mathrm{W\,cm^{-2}}$. At these ultra-high intensities the normalized laser amplitude for typical optical wavelengths is $a_0 \gtrsim 250$ and electrons become ultra-relativistic in a fraction of the wave period losing large amounts of energy by emission of electromagnetic radiation. Such strong emission and its back-reaction or radiation reaction (RR) may in turn lead to a significant deviation from the prediction of the Lorentz force alone. Hence, RR effects may significantly affect the collective dynamics of electron and ions and must be included in PIC simulations of laser-plasma interactions at ultra-high intensities in order to have reliable qualitative and quantitative predictions of the dynamics and in particular of the ion energy spectrum. This may also be of relevance for the

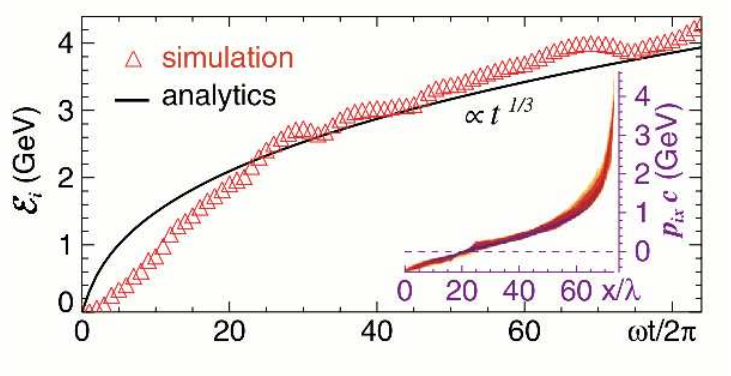

Figure 5.1: The maximum ion (proton) kinetic energy as a function of time and the ion phase-space projection (x, p_x) at $t = 80\,T$ obtained with a three-dimensional PIC simulation of thin foil acceleration in the radiation pressure dominated regime. The solid line reports the analytical prediction according to the light sail model. From Ref.[19].

design of future experiments at ultra-high intensity such that those foreseen with the construction of the ELI facility [2].

In 2002, pioneering PIC simulations of RR effects (included via the LL equation) in laser-plasma interaction were performed by Zhidkov *et al.* (see Ref. [24]) for the case of a thick plasma slab and a linearly polarized laser pulse. It was found that RR effects depend non-linearly from the laser intensity I and lead to a noticeable dissipation of the laser pulse energy. Further studies of RR effects for the case of thick targets either using the Sokolov equation or using a different RR modelling were performed recently both for thick targets [23, 26, 27] and for laser and plasma parameters such that the plasma foil is transparent to the laser pulse [25] showing that RR effects lead to a beneficial effect reducing the fraction of hot electrons and increasing the number of accelerated ions.

Concerning RR effects in the case of interaction with thin plasma foils in the RPDA regime, in Ref. [19] it was conjectured that the higher the velocity to which the plasma foil is accelerated, the lower the RR force becomes because of the relativistic increase of the laser wavelength λ' in the rest frame of the foil, making the RR strength parameter $\sim r_e/\lambda'$ increasingly

small (see 1.24, each term of the RR force is proportional to $\sim r_e/\lambda$). This mechanism of quenching of RR effects may also be explained with the help of the effective reduced LL equation (1.26) in the laboratory frame: when the foil moves coherently with a velocity close to c, the amplitude of the reflected wave is strongly reduced at any time in the laboratory frame; thus, the electrons at the surface of the foil can be considered as moving in the field of the incident plane wave and parallel to its propagation direction with a velocity $v_x \sim c$ and the RR force almost vanishes (see the discussion in section 1.2). However, our multi-dimensional simulations have shown that this picture holds only in the case of circular polarization and for laser and plasma parameters such that the laser pulse does not break through the foil. In other cases, RR effects strongly affect the dynamics leading to an increased spatial bunching of both electrons and ions and to a noticeable cooling of hot electrons with a beneficial effect on the quality of the ion spectrum [11, 12, 13].

5.1 1D simulations: role of the laser polarization

PIC simulations with a plasma slab of ions (protons) with uniform initial density n_0 were performed. Since our main aim is to evaluate the importance of RR effects on laser-plasma dynamics and ion acceleration in the regime of radiation pressure dominance, we begin with a 1D geometry for the sake of simplicity and the possibility of using high numerical resolution. The role of multi-dimensional effects is investigated in section 5.2 with fully three-dimensional PIC simulations; it is shown that the trends of RR effects found in 1D simulations hold qualitatively even in this case. We remark that for 1D (2D) simulations we mean that the *space* is one (two) dimensional while the *momentum space* is always fully three-dimensional.

We considered a total of three laser intensities $I = 2.3 \times 10^{23}\,\mathrm{W\,cm^{-2}}$, $I = 5.5 \times 10^{23}\,\mathrm{W\,cm^{-2}}$ and $I = 10^{24}\,\mathrm{W\,cm^{-2}}$ for both circular polarization (CP) and linear polarization (LP) and a laser wavelength $\lambda = 0.8\,\mu\mathrm{m}$. In the following, we mainly focus on results for a laser intensity $I = 2.3 \times$

$10^{23}\,\mathrm{W\,cm^{-2}}$ corresponding to a normalized laser amplitude $a_0 = 328$ for LP ($a_0 = 232$ for CP). In all the simulations, the initial density is $n_0 = 100\,n_c$ and the profile of the laser field amplitude has a trapezoidal shape in time with one-cycle, $\sin^2$-function rise and fall and a five-cycle constant plateau. The laser pulse front reaches the edge of the plasma foil at $t = 0$. The foil thickness is $\ell = 1\,\lambda$ in all the simulations except for the transparency case reported below, for which $\ell = 0.3\,\lambda$. The parameters are similar to those of the 3D simulations in Ref. [19], where the laser pulse was linearly polarized.

In the CP case, we found that RR effects on the ion spectrum (distribution of protons per unit energy) are negligible as shown in Fig. 5.2 at $t = 46\,T$ where $T = \lambda/c \approx 2.67\,\mathrm{fs}$ is the laser period. Even at higher intensities, RR effects on the ion spectrum are weak provided that there is not a strong transmission of the laser pulse through the foil (see Fig. 5.3). These results may be explained noticing that e.g. in the simulation corresponding to Fig. 5.2, the laser pulse penetrates into the plasma for a small distance of the order of $\lambda/20$, the fields in the plasma are much smaller than the fields in vacuum and the order of magnitude of the electron energy γ is some tens (see Fig. 5.4). As a consequence of the relatively small fields and electron energy, the order of magnitude of the friction coefficient introduced in Eq. (1.27) is $d \sim 10^{-2}$. We recall that the friction coefficient d provides a measure of the strength of the RR force in normalized units, RR effects are significant when the values of d are comparable with the Lorentz force in normalized units, which is of the order of the values of the normalized fields inside the plasma. The spatial profiles of both the fields and the coefficient d in the skin layer are shown in Fig. 5.4. We remark that Fig.5.4 shows a snapshot at $t = 1.7\,T$, but the typical values of the friction coefficient d are always of the same order of magnitude for CP.

Reducing the foil density or thickness, the laser pulse may break through the foil. In this case a significant fraction of electrons move in a strong electromagnetic field becoming ultrarelativistic in a fraction of the wave cycle and RR effects strongly affect the ion spectrum, as shown in Fig. 5.5. In particular, when RR is included, peaks in the energy spectrum appear at energies higher than in the case without RR. This result is similar to that obtained in Ref. [25] at lower intensities ($\sim 10^{22}\,\mathrm{W\,cm^{-2}}$), where it was suggested that

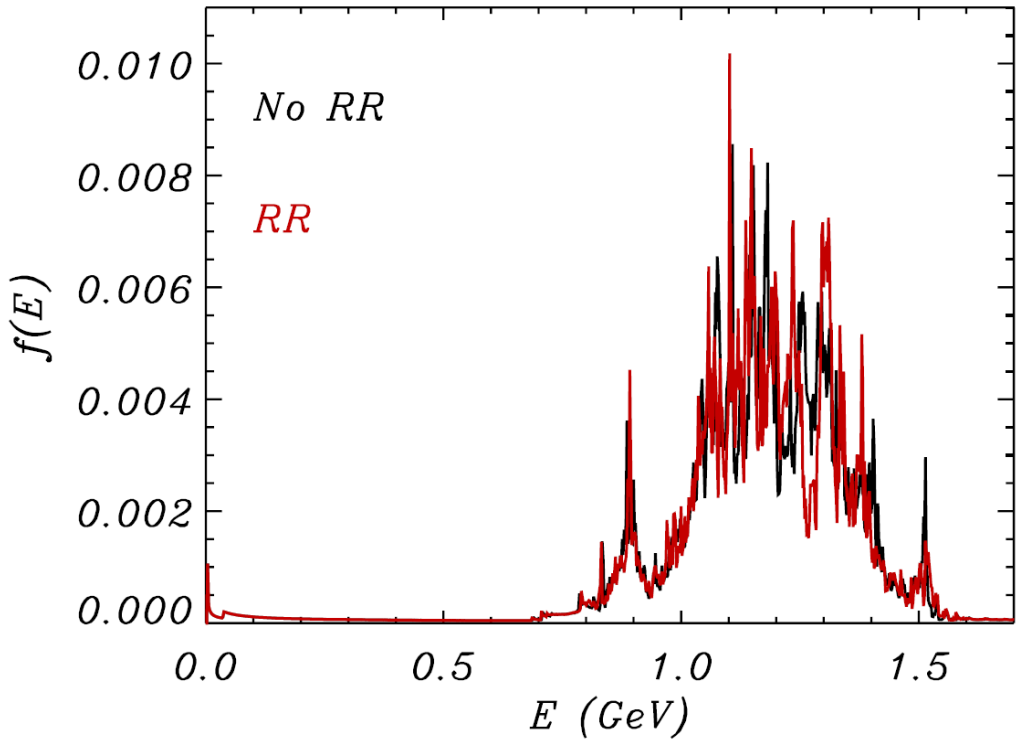

Figure 5.2: Ion energy spectrum $f(E)$ at $t = 46\,T$ with (red) and without (black) RR for CP. The laser intensity is $I = 2.3 \times 10^{23}\,\mathrm{W\,cm^{-2}}$ and the target thickness is $\ell = 1\lambda$.

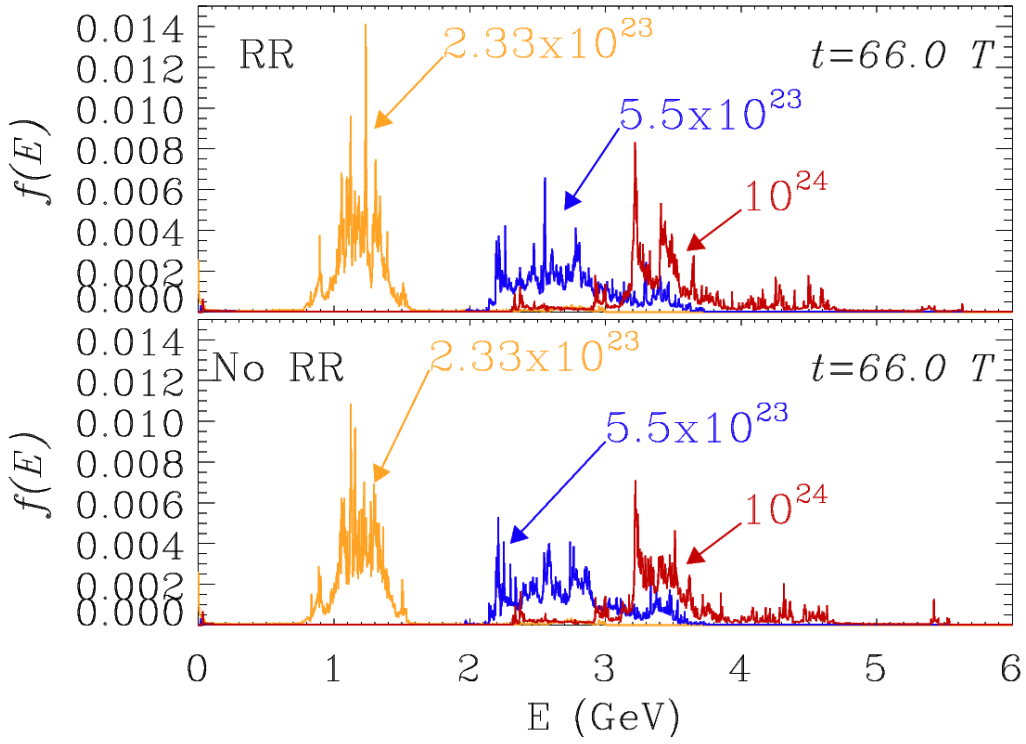

Figure 5.3: Ion energy spectra at $t = 66\,T$ with (top) and without (bottom) RR for CP. The laser intensity I is $2.3 \times 10^{23}\,\mathrm{W\,cm^{-2}}$ (yellow), $5.5 \times 10^{23}\,\mathrm{W\,cm^{-2}}$ (blue), $10^{24}\,\mathrm{W\,cm^{-2}}$ (red) and the target thickness is $\ell = 1\lambda$.

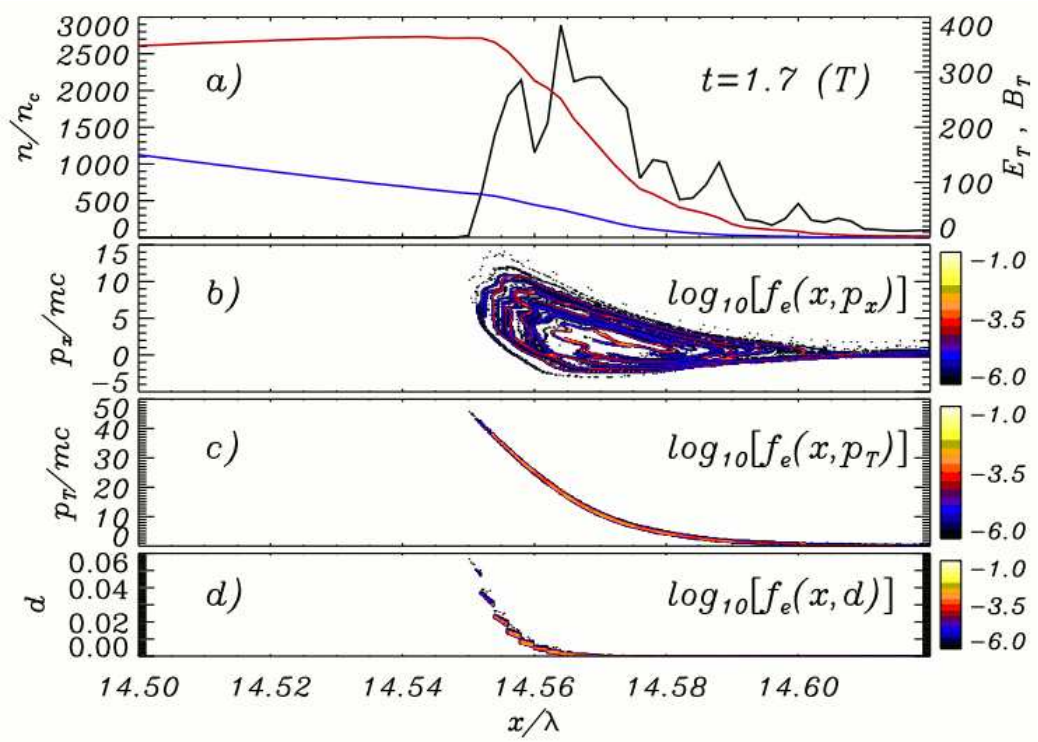

Figure 5.4: Snapshot at $t = 1.7\,T$ of the 'skin' layer of the foil for CP and intensity $I = 2.3 \times 10^{23}\,\mathrm{W\,cm^{-2}}$. The foil was initially placed between $x = 14\lambda$ and $x = 15\lambda$. (a) The electron density (black), the modulus of the transverse electric $E_T = \sqrt{E_y^2 + E_z^2}$ (blue) and magnetic $B_T = \sqrt{B_y^2 + B_z^2}$ (red) fields. Distribution of (b) the longitudinal momentum p_x, (c) modulus of the transverse momentum $p_T = \sqrt{p_y^2 + p_z^2}$ and (d) friction coefficient d.

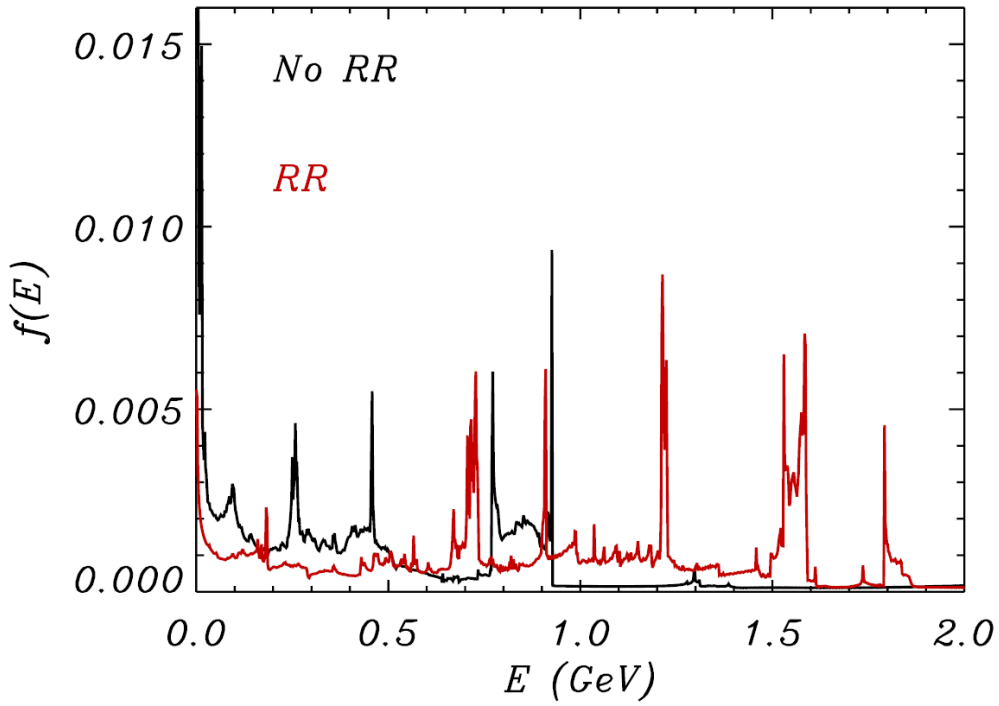

Figure 5.5: Ion energy spectrum $f(E)$ at $t = 46\,T$ for a simulation with the same parameters as Fig. 5.2 but with a target thickness $\ell = 0.3\lambda$. In this case the laser pulse breaks through the foil and RR effects are evident.

RR effects 'improve' the ion spectrum in the optical transparency regime. This may be explained recalling that the RR force reaches its maximum for electrons counter-propagating with the laser pulse therefore impeding the electron backward motion. This leads to an increased electron bunching and to a later breakthrough of the laser pulse through the foil with a longer and more efficient radiation pressure stage. However, comparing Fig. 5.5 with the thicker target case in Fig. 5.2, it is evident that the spectrum becomes far from monoenergetic, while the maximum ion energy increases only slightly. Hence, in our simulations 'optimal' conditions for ion acceleration are found for the case of Fig. 5.2; for the corresponding laser and plasma parameters, RR effects are negligible.

In the LP case, the foil is accelerated by radiation pressure too but unlike the CP case, the laser pulse does penetrate up to a fraction of the order of $\lambda/4$ at the front surface of the foil, as shown in Fig. 5.6. For LP, it is found that a significant fraction of electrons at the front surface move in a strong electromagnetic field of the same order as the vacuum fields. In this case, the friction coefficient function d reaches values of $d \approx 10^2$ (see Fig. 5.6), which are comparable with the Lorentz force. The deeper penetration of the laser pulse is correlated with the strong longitudinal oscillatory motion driven by the oscillating component of the $\mathbf{J} \times \mathbf{B}$ force, which is suppressed for CP. In fact, large numbers of electrons are pushed periodically inside the foil, producing strong fluctuations of the electron density (see Fig. 5.6, part (a)).

For LP, the ion energy spectrum is significantly affected by RR effects (see Figs. 5.7, 5.8). In the lower intensity case, the spectrum is fairly peaked during the acceleration phase with a smaller energy spread and a lower peak energy than in the case without RR (Fig. 5.7). In general, as observed in many simulations, the energy distribution broadens with increasing electron 'temperature', since hot electrons drive the expansion of the plasma, leading to additional, non-monoenergetic ion acceleration. The smaller energy spread observed when RR is included can thus be traced back to the radiative cooling of the most energetic electrons.

Moreover, a significant fraction of ions on the low-energy tail of the spectrum is observed in the case without RR, but disappears when RR is included (Fig. 5.7). To explain this effect, we recall that ions are accelerated

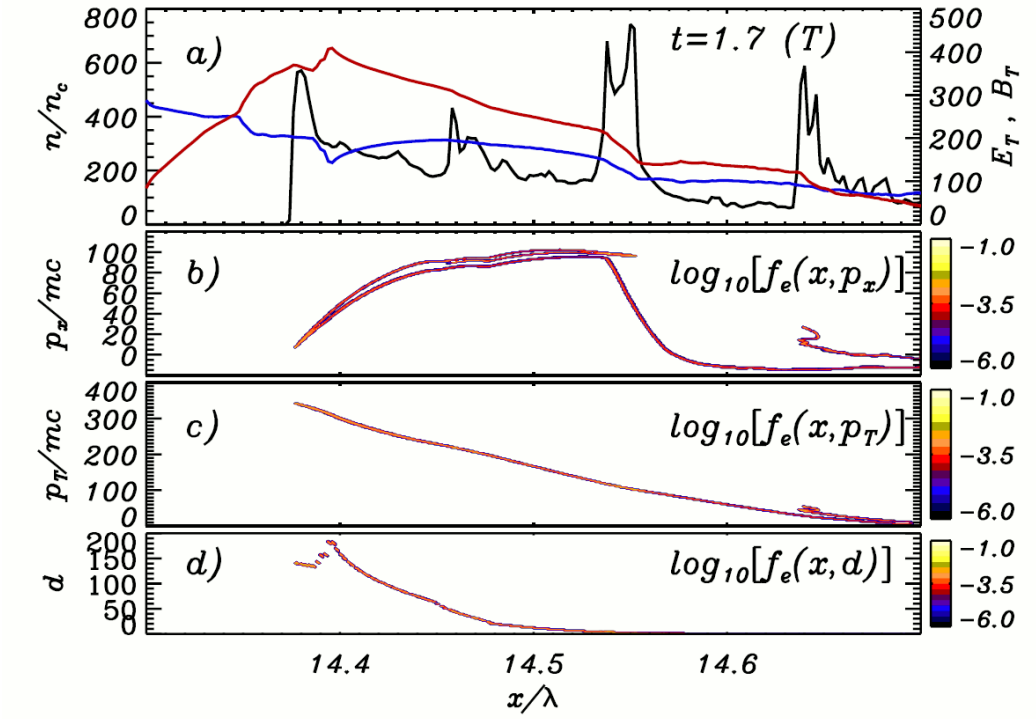

Figure 5.6: Snapshot at $t = 1.7\,T$ of the 'skin' layer of the foil for LP and intensity $I = 2.3{\times}10^{23}\,\mathrm{W\,cm^{-2}}$. The foil was initially placed between $x = 14\lambda$ and $x = 15\lambda$. The strong longitudinal oscillations driven by the $\mathbf{J} \times \mathbf{B}$ force allow a deeper penetration of the laser pulse into the foil compared to the CP case reported in Fig.5.4. (a) The electron density (black), the modulus of the transverse electric $|E_y|$ (blue) and magnetic $|B_z|$ (red) fields. Distribution of (b) the longitudinal momentum p_x, (c) modulus of the transverse momentum $p_T = |p_y|$ and (d) friction coefficient d.

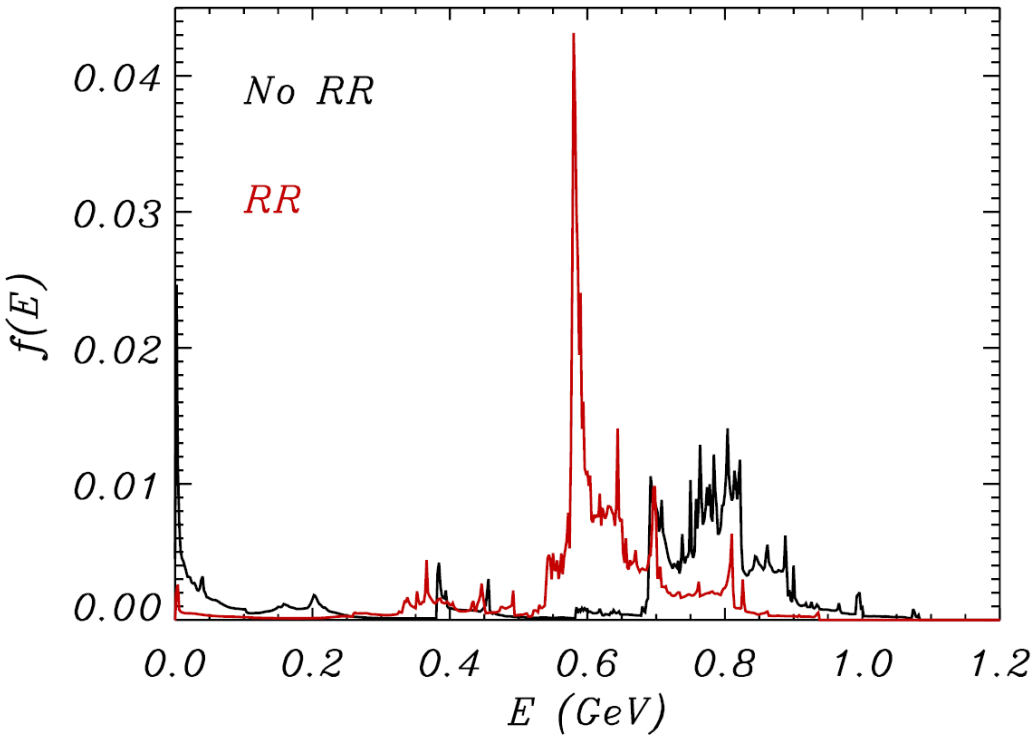

Figure 5.7: Ion energy spectrum $f(E)$ at $t = 12\,T$ with (red) and without (black) RR for LP. The laser intensity is $I = 2.33 \times 10^{23}\,\mathrm{W\,cm^{-2}}$ and the target thickness is $\ell = 1\lambda$.

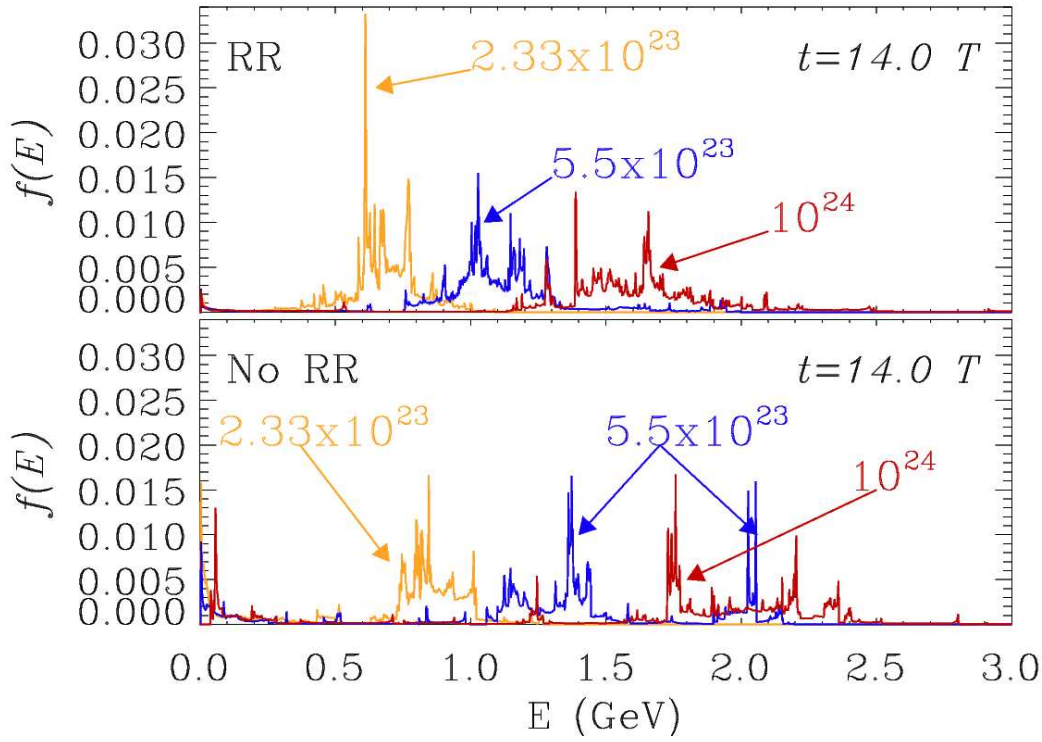

Figure 5.8: Ion energy spectra at $t = 14T$ with (top) and without (bottom) RR for Linear Polarization. The laser intensity I is $2.3 \times 10^{23}\,\mathrm{W\,cm^{-2}}$ (yellow), $5.5 \times 10^{23}\,\mathrm{W\,cm^{-2}}$ (blue), $10^{24}\,\mathrm{W\,cm^{-2}}$ (red) and the target thickness is $\ell = 1\lambda$.

by the steady electric field generated by the charge separation; if a significant fraction of fast electron moving backward is generated during the laser-foil interaction, then a corresponding fraction of ions may be neutralized and remains at lower energies. When the foil is still non-relativistic in the laboratory frame, the RR force has larger values when electrons counter-propagate with respect to the laser pulse and therefore the electron backward motion is strongly impeded with RR force included. This effect prevents an efficient neutralization of lower energy ions by returning electrons, these ions can be therefore accelerated by the charge separation field explaining why a lower number of low-energy ions is observed with RR.

The fractional difference in ion energy with RR versus without RR is of the order of the fraction of the laser pulse energy that is lost as incoherent emission (Fig. 5.9). For $I = 2.3 \times 10^{23}\,\mathrm{W\,cm^{-2}}$, about 20% of the total pulse energy is dissipated by the RR force during the laser-foil interaction (Fig. 5.9), which lasts about 22 cycles (30 cycles without RR). As discussed in section 1.2, such dissipated energy accounts for the incoherent radiation escaping from the plasma. During the laser-foil interaction, such a flux of incoherent radiation shows itself in a missing pulse energy, while ions have almost the same total energy in both cases and their spectrum is quasi-monochromatic (Fig. 5.7). However, after the acceleration phase by the radiation pressure of the laser pulse, a 20% missing pulse energy implies nearly the same amount of missing final ion energy (Fig. 5.9).

We remark that just changing the laser polarization from CP to LP, the friction coefficient d increases by up to *four-orders* of magnitude due the enhanced laser pulse penetration into the foil by the $\mathbf{J}\times\mathbf{B}$-driven longitudinal oscillations. Then, the electrons on the 'skin' layer of the foil move in strong electromagnetic fields of the same order of vacuum fields becoming ultra-relativistic and the friction term of the RR force becomes comparable with the Lorentz force.

As discussed previously, these results are a relevant test of the conjecture in Ref. [19] that RR effects would be weak as the foil motion becomes relativistic. Our simulations suggest that this picture strictly holds only in the CP case, where almost all of the foil moves at relativistic speed in the same direction as the laser pulse. In the LP case, a substantial fraction of elec-

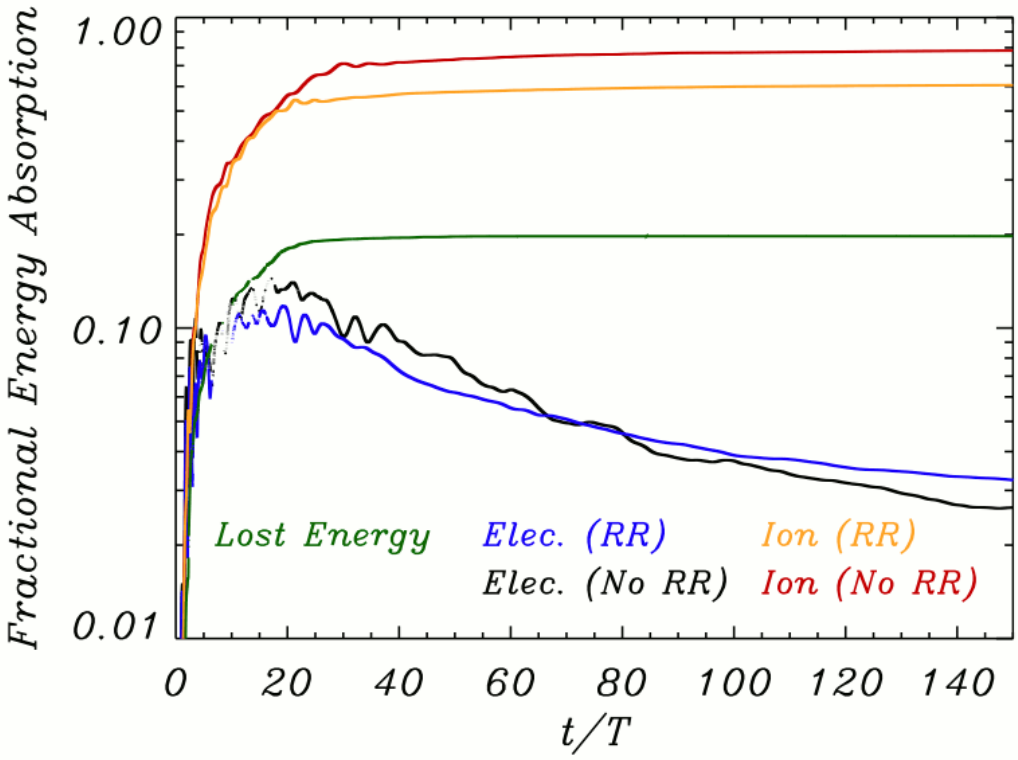

Figure 5.9: Fractional energy absorption as a function of time for LP and intensity $I = 2.3 \times 10^{23}\,\mathrm{W\,cm^{-2}}$. Electron kinetic energy with RR (blue) and without RR (black), ion kinetic energy with RR (orange) and without RR (red) and the fraction of energy lost in the system (green).

trons has both an ultra-relativistic motion in the transverse direction and a strong oscillatory motion in the longitudinal direction, leading to significant RR effects.

The dependence of RR effects on the pulse polarization was also studied in Refs. [23, 26, 27] for thick targets and long pulse durations. It was also found that RR effects are stronger for LP, although they are not negligible for CP [27]. These results cannot be compared straightforwardly to our findings because of the quite different laser and plasma parameters, leading to different dynamics. For instance, in the thick target case the laser-plasma surface oscillates also for CP ('piston oscillations' [27]) and a return current of electrons counter-propagating with respect to the laser pulse is generated; this effect is likely to enhance radiative losses.

Summarizing, the differences between LP and CP appear to be related to the different fraction of electrons moving into superintense fields. For LP, longitudinal electron oscillations driven by the $\mathbf{J} \times \mathbf{B}$ force allow a deeper penetration of the laser pulse into the foil enhancing the effect of the RR force on electrons. In the CP case, the oscillating component of the $\mathbf{J} \times \mathbf{B}$ force is suppressed [54], then electrons on the front surface pile-up, the numerical density grows exceeding thousand of times the critical density n_c and the laser pulse cannot penetrate into the foil significantly (i.e. the effective skin depth is a small fraction of both the foil thickness and the laser wavelength). For CP, significant RR effects are found only for laser and plasma parameters such that the laser pulse breaks through the foil due to nonlinear transparency, similar to what was found in previous studies [25]. In this latter case, RR effects are important for both LP and CP and higher ion energies are achieved in the case with RR included since the increased electron bunching delays the breakthrough of the laser pulse and leads to a longer and more efficient RPA phase.

5.2 Three-dimensional PIC simulation results

In this section, RR effects in the interaction of a superintense laser pulse with a thin plasma foil as well as their relationship with the laser pulse polarization are investigated with multi-dimensional PIC simulations.

A systematic comparison of LP versus CP in the RPDA regime where the radiation pressure of the laser pulse becomes the dominant mechanism of ion acceleration both for CP and LP has not been performed yet. To this aim, a three-dimensional (3D) approach is important because e.g. in 2D simulations and for LP the laser-plasma coupling is different for S- and P-polarization (i.e. for the electric field of the laser pulse either perpendicular or parallel to the simulation plane, respectively) suggesting a complex and asymmetric target deformation and expansion in 3D and the constraint of the conservation of angular momentum carried by CP pulses holds in 3D only. Multi-dimensional effects in the RPDA regime may play a crucial role as found in previous 2D simulations which have both shown the onset of instabilities [49] but also a potentially 'unlimited' energy gain for the fraction of ions that are phase-locked with the laser-pulse [50].

Preliminary 2D studies

Large-scale 3D PIC simulations are limited by the size and availability of computational resources both in the numerical resolution and in the number of runs that may be performed. These issues may raise doubts on the accuracy of 3D results. To gain confidence on this side, 2D simulations both with numerical parameters similar to those of 3D runs and with higher accuracy were performed prior to 3D runs.

We recall that in 2D simulations and for LP the electric field of the laser pulse can be directed either in the direction perpendicular to the simulation plane ("S"-polarization) or parallel to the simulation plane ("P"-polarization). These two different possibilities lead to a very different dynamics (see Fig. 5.10) as in the "P"-polarization case the electric field of the laser pulse strongly disperses electrons and ions along the polarization direction which lies in the simulation plane while in the "S"-polarization case electrons and ions tend to be collected in clumps which may be generated by transverse instabilities such as those studied in Ref. [49]. Hence, in full 3D simulations and for LP strong anisotropies in the electron and ion spatial distribution are expected as a consequence of the very different laser-plasma coupling in the plane perpendicular or parallel to the polarization axis; such

strong anisotropies are indeed found in our 3D simulations (see below).

Results of 2D simulations for the three different polarization cases (CP, LP-S and LP-P) with and without RR are reported in Fig. 5.10 which shows the color contours of $\sqrt{\mathbf{E}^2 + \mathbf{B}^2}$ (in normalized units) with black contours of the ion and electron densities superimposed. In these 2D simulations, the physical parameters are the same of the 3D case reported below while both numerical parameters analogous to the 3D simulations (left column) and numerical parameters with an increased accuracy (right column) are reported. Increasing the numerical accuracy leads to small differences in the CP case (third row in Fig. 5.10) where the formation of a parabolic-like shell moving at relativistic velocity is observed. The reflection of the impinging pulse from the walls of such parabolic-like shell moving at relativistic velocity generates the observed regular interference pattern and may be explained recalling that in the instantaneous rest frame the shell appears stretched along the direction of motion and its walls are therefore similar to two nearly parallel mirrors with the impinging pulse reflected between them. For CP, the RR force leads to negligible effects in agreement with the results of 1D simulations.

Numerical effects lead to larger differences for P- and S-polarized pulses compared to CP although the main qualitative features are preserved also for these cases (see Fig. 5.10). For S- and P-polarization, the interference pattern observed for CP is not present since the parabolic-like shell is not generated. For P-polarization the foil is completely dispersed and electrons are grouped into structures stretched and aligned along the polarization axis while only a relatively small fraction of ions is accelerated effectively. For P-polarization RR effects are apparent and lead to an increased bunching of electrons and ions therefore reducing the foil transparency and delaying the foil breakthrough (compare frames (a1) with (b1) and (c1) with (d1) in Fig. 5.10). In the case of S-polarization noticeable modulations appear in the foil density with the formation of clumps both in the electron and ion densities. In particular, two main clumps are observed near the central region of the foil; increasing the resolution these clumps are denser and shifted closer to the central axis while the penetration of the laser pulse into the foil as well as RR effects are reduced. The formation of such clumps is presumably

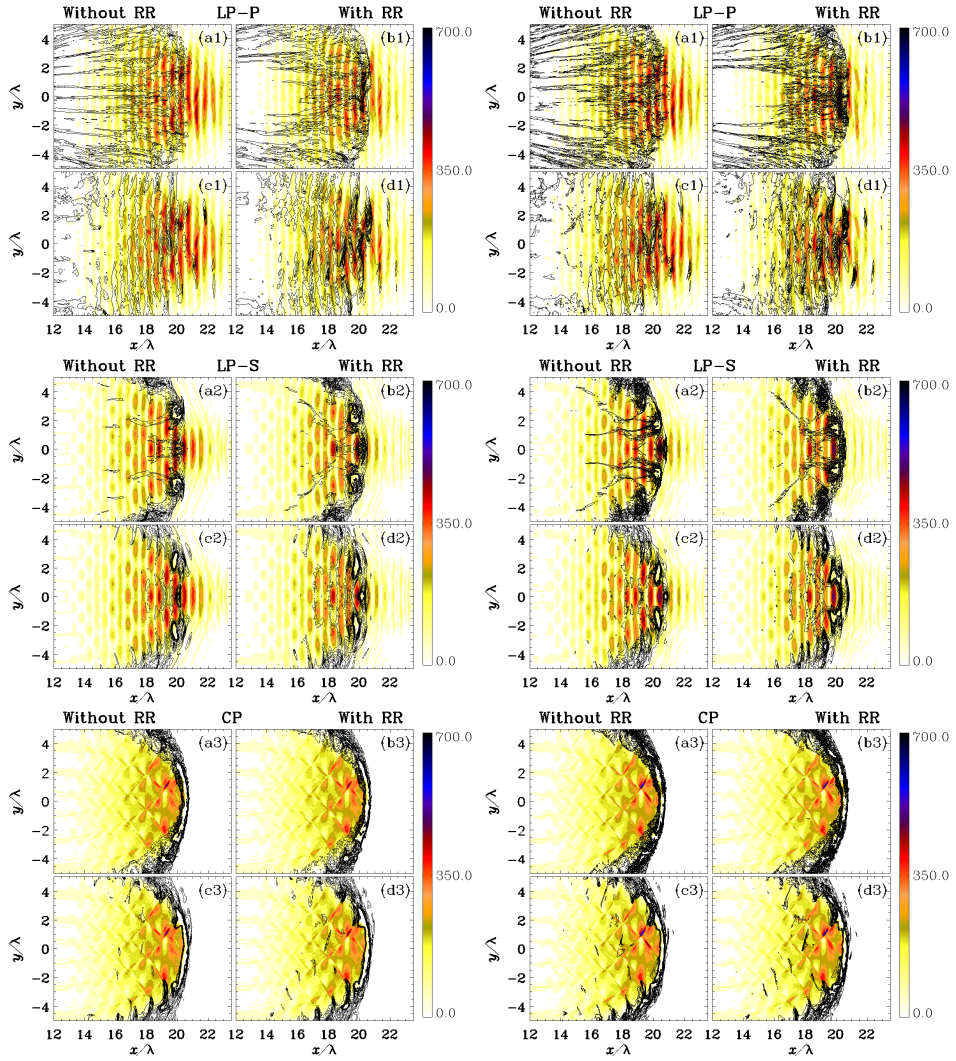

Figure 5.10: 2D simulations of the laser pulse-foil interaction at $t = 20\,T$. Each frame reports the color contours of $\sqrt{\mathbf{E}^2 + \mathbf{B}^2}$ (normalized units) without RR (a1-3 and c1-3) and with RR (b1-3 and d1-3). Black contours of the *ion* density are superimposed for the case without RR (a1-3) and with (b1-3) RR. Black contours of the *electron* density are superimposed for the case without RR (c1-3) and with (d1-3) RR. Left column: simulations with numerical parameters analogous to those of 3D simulations i.e. spatial step $\lambda/44$ for each direction and 256 particles-per-cell. Right column: the same simulations of left column with spatial step $\lambda/80$ for each direction and 625 particles-per-cell. First row, "P"-polarization case; second row, "S"-polarization case; third row, CP case.

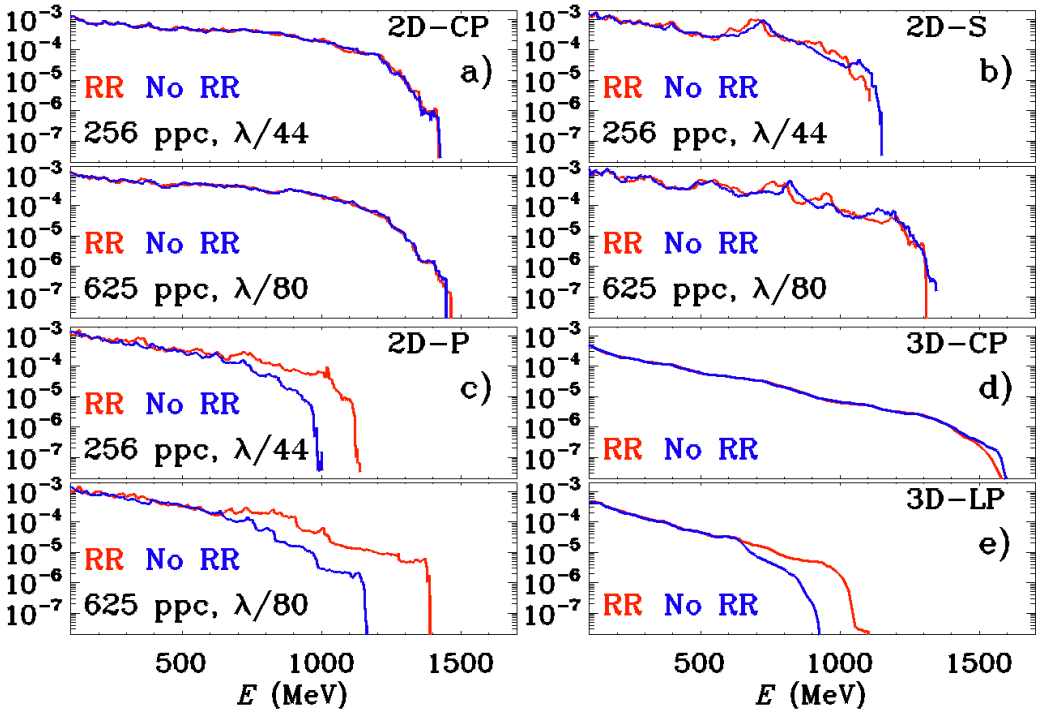

Figure 5.11: Ion spectra from 2D [a)-c)] and 3D [d)-e)] simulations with same physical parameters, all at $t = 20\,T$. The 2D spectra are reported for circular (CP, frame a)) and linear (LP) "S" (frame b)) and "P" (frame c)) polarization cases (i.e. for the electric field of the laser pulse either perpendicular or parallel to the simulation plane, respectively). In each plot, the blue and red curves correspond to simulations without and with radiation reaction (RR) effects, respectively. In the upper plots of frames a)-c) the numerical resolution (number of particles per cell and of points per wavelength) is similar to those of the 3D simulations in d)-e), while in the lower plots the results for higher resolution are shown.

driven by transverse inhomogeneities in the $\mathbf{J} \times \mathbf{B}$ force which may lead to instabilities as observed in previous studies [49].

The effect of increasing resolution and particle number on the ion spectra in 2D simulations is shown in Fig. 5.11 where 2D results are reported for the three different polarization cases (CP, LP-S and LP-P) and compared with the results obtained with 3D simulations for both LP and CP. In the CP case both numerical and RR effects on the spectrum are smaller while in the P-polarization case these effects are larger. Changing the spatial resolution from $\lambda/44$ to $\lambda/80$ and increasing the number of particles-per-cell (ppc) for each species from 256 to 625 shifts the energy cut-off by $\sim 2\%$ in the CP case and by $\sim 15\%$ ($\sim 20\%$) in the P-polarization case without RR (with RR). The stronger effect of the inclusion of RR for the higher resolution case may be explained by noticing that RR mostly affects the highest energy electrons, which are located in the tail of the distribution function that needs a very high number of particles to be resolved properly. However, the limited resolution does not qualitatively affect prominent features such as the higher energy for CP and the relevance of RR effects for LP only, leading for this latter case to an *higher* energy of ions as observed in 1D simulations in the regime of foil transparency [11]. At the same time, 2D and 3D spectra show new features such as an higher cut-off energy in 3D than in the 2D case, and the fact that P-polarization leads to a much stronger RR effect than the S-polarization case.

Full 3D simulations

Set up

We present a total of four 3D simulations each with the same physical and numerical parameters but different polarization, with and without RR effects. In these simulations, the laser field amplitude has a $\sin^2$-function longitudinal profile with 8λ FWHM (where $\lambda = 0.8$ μm is the laser wavelength) while the transverse radial profile is Gaussian with 10λ FWHM and the laser pulse front reaches the edge of the plasma foil at $t = 0$. The peak intensity at the focus is $I = 1.7 \times 10^{23}\,\mathrm{W\,cm^{-2}}$ which corresponds to a normalized amplitude $a_0 = 280$ for LP and $a_0 = 198$ for CP. The target is a plasma foil of electrons

and protons with uniform initial density $n_0 = 64\, n_c$ (where $n_c = \pi m_e c^2/e^2\lambda^2$ is the critical density), thickness $\ell = 1\lambda$ and initially located in the region $10\lambda \leq x \leq 11\lambda$. The simulation box is $30\lambda\,(x) \times 20.36\lambda\,(y) \times 20.36\lambda\,(z)$ while the grid is $1320\,(x) \times 896\,(y) \times 896\,(z)$; consequently the spatial step is $\lambda/44$ for each direction. The timestep is $T/100$ where $T = \lambda/c = 2.67\,\mathrm{fs}$ is the laser period. We use 216 particles-per-cell for each species and the total number of particles is 1.526×10^{10}.

We remark that such 3D simulations are very challenging from the computational point of view since thousands of CPUs and at least one TB of RAM memory are required for several hours to complete a relatively short simulation which may last in all 15-20 laser periods. The subsequent issue of data analysis and visualization is also challenging as large datasets of the order of some TB have to be managed and the relevant information has to be presented in a clear and meaningful way usually with three-dimensional plots or suitable 2D sections.

Polarization and anisotropy effects

Figures (5.12, 5.13) shows the ion and the electron 3D spatial distributions at $t = 20\,T$ for the LP case without (a) and with (b) RR and for the CP case without (c) and with (d) RR. The color corresponds to the range in kinetic energy. In the LP case the most energetic ions are grouped into two off-axis clumps lengthened and aligned along the polarization direction. The second most energetic ion population is also stretched along the polarization direction with two off-axis clumps and a widespread central clump, in which ions are grouped asymmetrically. The density of this latter population is smaller than that of the two higher-energy clumps.

RR effects are much stronger for LP, where the density and the total number of ions grouped into the highest energy populations is strongly enhanced in the case with RR as seen by the comparison of Figs. 5.12 a) and b) and also in Figs .5.14 a1), a2) and b1), b2) where sections of the ion density in the (x, y) and (x, z) planes are shown. The contours of the electromagnetic (EM) energy density in Figs. 5.14 a1), a2) and b1), b2) show that near the axis most of the laser pulse have been transmitted through the target.

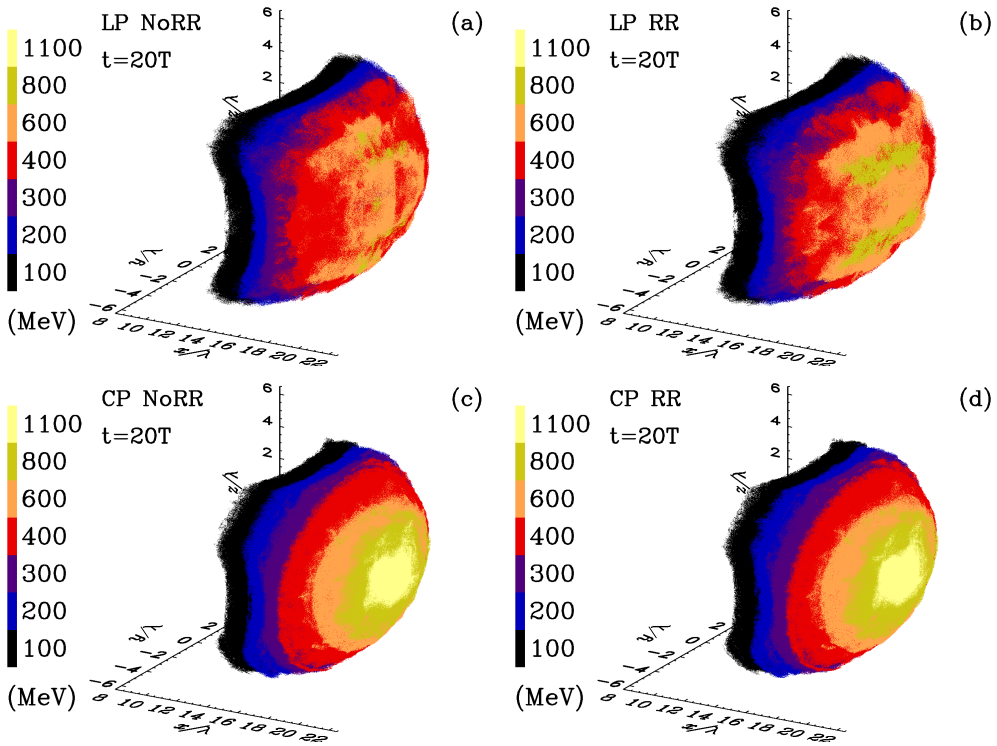

Figure 5.12: Spatial distributions of ions at $t = 20\,T$ and in the region $-5.7 \leq (y, z)/\lambda \leq 5.7$, for LP without (a) and with (b) RR and for CP without (c) and with (d) RR. Ions are divided into seven populations according to their kinetic energy, with the color-bar reporting the lower bound of the energy interval. In the LP case (frames (a,b)), the polarization is along the y axis.

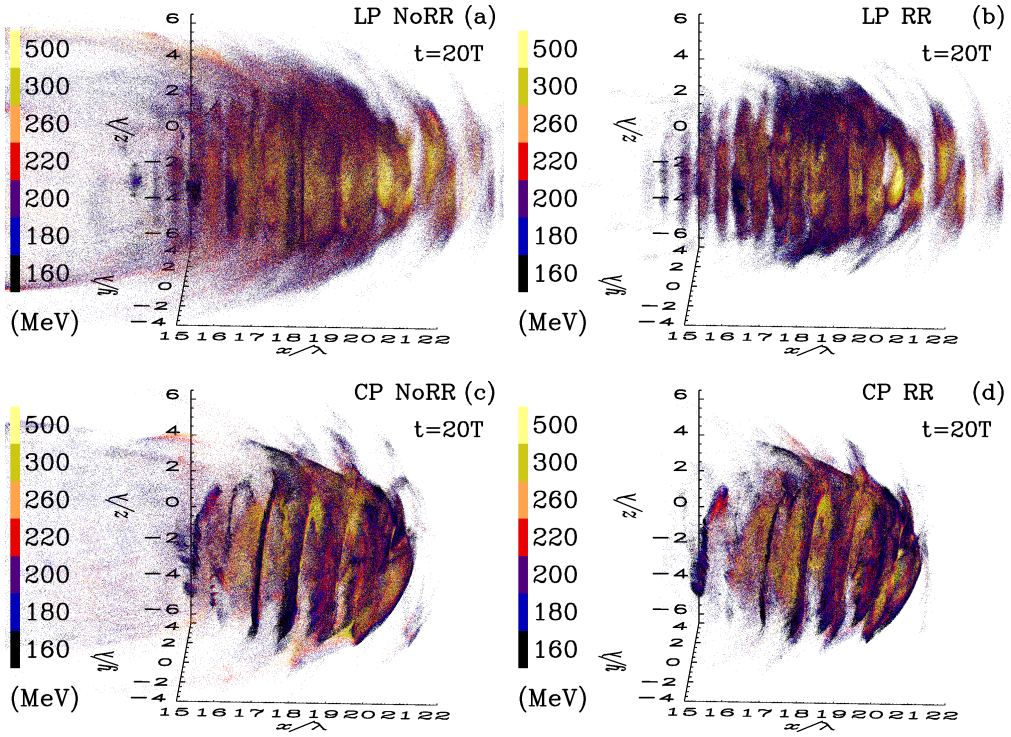

Figure 5.13: Spatial distributions of electrons at $t = 20\,T$ and in the region $-5.7 \leq (y, z)/\lambda \leq 5.7$, for LP without (a) and with (b) RR and for CP without (c) and with (d) RR. Electrons are divided into seven populations according to their kinetic energy, with the color-bar reporting the lower bound of the energy interval. In the LP case (frames (a,b)), the polarization is along the y axis.

The increased bunching and higher density observed in the case with RR may be related to the higher ion energies since the local increase of the density and therefore of the reflectivity leads to a longer and more efficient RPDA phase. This is consistent with observing in Figs. 5.14 b1) and b2) that the EM energy density is higher off-axis and behind the high-density clumps, which correspond to the most energetic ions. The high-energy clumps observed in the LP case are also similar to the ion lobes observed in Ref. [61] at lower intensity but still in a regime of strong pulse penetration through the foil. RR effects play a minor role for CP affecting only a small fraction of ultra-relativistic electrons with almost no influence on the ion distribution as seen in Figs. 5.12, 5.12, frames c),d). For CP, the ion spatial distribution follows the spatial intensity profile of the initial laser pulse, has rotational symmetry around the central axis, and a distribution in energy monotonically decreasing with increasing radial distance. The most energetic ions ($E \geq 1100\,\mathrm{MeV}$) are located near the axis. No population in the same energy interval is present in the LP case (compare frames (a,b) with (c,d) in Fig.5.12). The electron spatial distribution has an helicoidal shape with step λ Fig. 5.13 (c), (d).

The differences between CP and LP can be explained by the absence of the oscillating component of the $\mathbf{J} \times \mathbf{B}$ force for CP [54]. Thus, in the CP case we have a steady push of the foil with weak penetration of the laser pulse in the plasma. Most of the electrons move coherently with the foil and in the same direction as the laser pulse so that the RR force may also becomes very small [19, 11]. For LP pulses, the longitudinal oscillations driven by the 2ω component of the $\mathbf{J} \times \mathbf{B}$ force result into a strong electron dispersion and heating yielding a significant decrease of the electron density and penetration of the pulse. The much stronger RR effects in the LP case are accounted for by both the strongest penetration of the laser pulse and the $\mathbf{J} \times \mathbf{B}$-driven oscillations of the electrons causing them to collide with the counter-propagating laser pulse twice per cycle [11].

Our 2D and 3D results confirm the strong differences between CP and LP also for a focused laser pulse and a strongly bent target. At the same time, the 2D and 3D results suggest that the "P" component of the electric field $\mathbf{E}$ (not present in 1D geometry) strongly contributes to enhanced electron

heating and dispersion, pulse penetration and RR effects. Such component is present both in the LP case and in the 2D case with P-polarization and its importance accounts for the similarity between the corresponding spectra in Fig.5.11 c) and e). For LP, the laser pulse significantly penetrates into the foil from the beginning of the interaction. After this initial phase, electrons and ions are dispersed laterally and asymmetrically by the y-component of the electric field. This lateral dispersion leads to a further decrease of the electron density and eventually the laser pulse breaks through the foil as seen in Fig. 5.14, frames (a1-d1) and (a2-d2). Electrons thus move into strong fields of the same order of the vacuum fields and clear signs of RR effects appear both in the electron and in the ion distribution. As shown in frames (a,b) of Fig. 5.13, the spatial distribution electrons also show a quasi-periodical distribution with a $\sim \lambda/2$ wavelength.

Pulse focusing effects

The 2D sections of the total electromagnetic energy density and of the electron and ion densities in Fig. 5.14 show a self-generated parabolic shell wrapping the laser pulse. The formation of such parabolic-like shell is similar to previous results obtained in 2D simulations and for CP although in 3D this focusing effect is much stronger, is present also for LP and leads to a qualitatively different distribution of the electromagnetic energy density (compare Fig. 5.14 with Fig. 5.10).

In the CP case, a mark of the helicoidal electron distribution is present in the form of strong modulations of the shell (much stronger than in the corresponding 2D simulations) while in the LP case the two denser and higher-energy clumps are clearly visible in the $x - z$ plane. In the CP case, this self-generated parabola focuses the impinging laser pulse up to nearly a λ^3 scale and both the energy and the momentum densities at the focus reach values more than eight times their peak value in the initial laser pulse. The self-generated parabola is present also in the LP case even though its focusing effect is slightly reduced as the laser pulse breaks through the parabolic shell and both the energy and momentum densities reach values more than five times their peak value in the initial laser pulse.

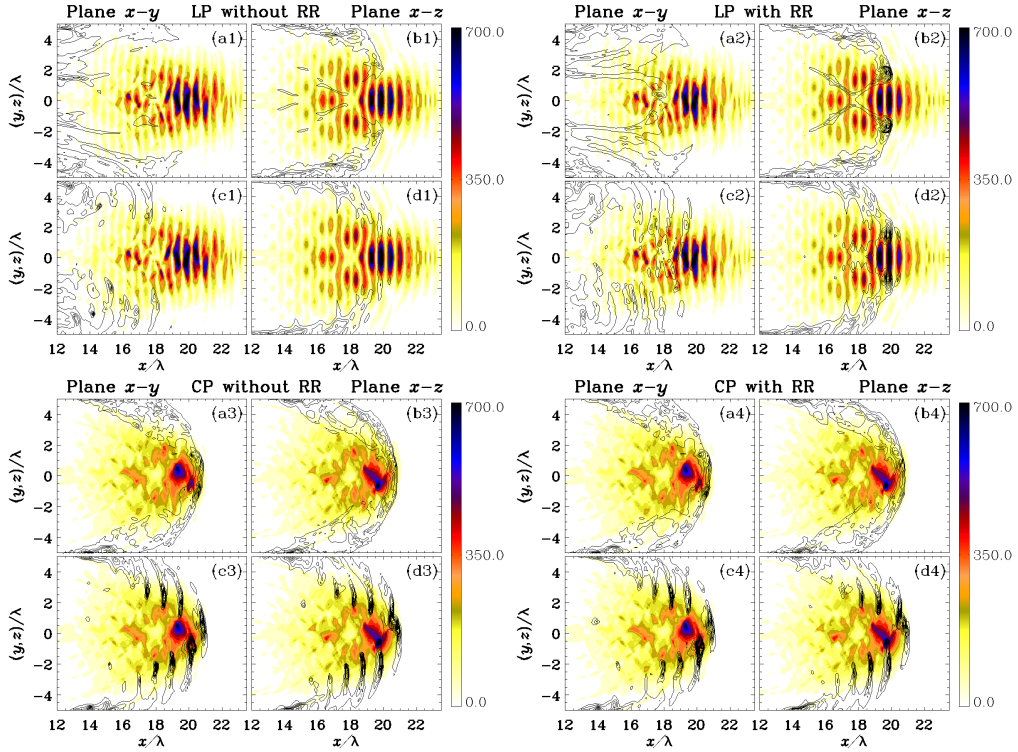

Figure 5.14: 2D sections of the laser pulse-foil interaction at $t = 20\,T$. Each frame reports the color contours of $\sqrt{\mathbf{E}^2 + \mathbf{B}^2}$ (normalized units) in the $x-y$ plane at $z = 0$ (a1-3 and c1-3) and in the $x-z$ plane at $y = 0$ (b1-3 and d1-3). Black contours of the *ion* density are superimposed for LP without (a1,b1) and with (a2,b2) RR and for CP without RR (a3,b3). Black contours of the *electron* density are superimposed for LP without (c1,d1) and with (c2,d2) RR and for CP without RR (c3,d3). The CP case with RR is almost identical to the CP case without RR and it is not reported.

The focusing effect is significantly stronger in 3D where the energy density at the focus is more than tripled (doubled) for linear (circular) polarization compared to the analogous 2D case (compare Fig. 5.14 with Fig. 5.10). This effect may explain the higher peak energy on axis observed in 3D, Fig. 5.11 d) with respect to the 2D case, Fig. 5.11 a).

Conclusions

In this thesis, we have provided a simple and suitable approximation of the Landau-Lifshitz equation for the radiation reaction force and we have developed a simple numerical approach to insert the radiation reaction force into existing Particle-In-Cell (PIC) codes while keeping the standard numerical solver for the Lorentz force unchanged. Our numerical approach was tested comparing the numerical prediction with the exact analytical solution for a monochromatic plane wave and with a fourth-order Runge-Kutta method with very good agreement. Inclusion of radiation reaction effects in PIC simulations via our numerical approach yielded a less than 10% increase in computational time, which is essential in order to perform large scale multi-dimensional simulations with limited computing power. Then, radiation reaction effects on the electron dynamics in the interaction of an ultra-intense laser pulse with a thin plasma foil were studied using multi-dimensional PIC simulations. To our knowledge, these are the first 2D and 3D PIC simulations of ion acceleration with radiation reaction effects included.

We summarize the results of our simulations as follows. In one-dimensional simulations, we checked radiation reaction effects for three different intensities: $I = 2.3 \times 10^{23}\,\mathrm{W\,cm^{-2}}$, $I = 5.5 \times 10^{23}\,\mathrm{W\,cm^{-2}}$ and $I = 10^{24}\,\mathrm{W\,cm^{-2}}$ comparing the results for circular and linear polarization of the laser pulse.

For circular polarization, we found that radiation reaction effects are not relevant even at intensity of $I = 10^{24}\,\mathrm{W\,cm^{-2}}$ provided that the laser pulse does not break through the foil. For laser and plasma parameters such that the laser pulse breaks through the foil the inclusion of radiation reaction effects leads to an increase of the ion energy. This may be explained recalling that the radiation reaction force mainly operates on high-energy electrons

counter-propagating with the laser field therefore reducing the dispersion of the foil which is mainly driven by the expansion of hot electrons. This leads to a longer and more efficient radiation pressure acceleration stage with a beneficial effect on the ion spectrum. However, the ion energy increase in the transparency regime is not very significant with respect to the case with the same laser parameters but a thicker target, for which the breakthrough of the laser pulse does not occur and radiation reaction effects are negligible.

For linear polarization radiation reaction effects are significant, leading to some tens of per cent of energy loss by incoherent emission of radiation and to a similar percentage of reduction of the peak ion energy. This may be explained noticing that part of the laser pulse energy is converted into high-energy photons that escape from the system freely reducing the energy available for ion acceleration. However, the quality of the ion spectrum is improved since the spread in the ion spectrum is reduced due to the strong cooling of hot electrons by the radiation reaction force.

Then, polarization and radiation reaction effects on ion acceleration in the radiation pressure dominant regime were studied with three-dimensional particle-in-cell simulations confirming the trends for radiation reaction effects observed in 1D simulations. In particular, the strong dependence of radiation reaction effects on the laser pulse polarization is observed also in three-dimensional simulations. However, three-dimensional simulations showed new qualitative features compared to lower dimensional simulations. In the linear polarization case strong anisotropies are observed, the most energetic ions are grouped into two off-axis clumps in the plane perpendicular to the propagation direction and radiation reaction effects significantly affect the energy spectrum. On the contrary, for circular polarization the ion spatial distribution follows the spatial intensity distribution of the impinging laser pulse with the most energetic ions on the symmetry axis and almost no radiation reaction effects. In both cases, we found that the deformation of the initially flat plasma foil due to the transverse inhomogeneity of the intensity leads to the self-formation of a quasi-parabolic shell that focuses the impinging laser pulse up to energy and momentum densities nearly one order of magnitude higher than the initial peak values. These may also explain the higher ion energies achieved in 3D simulations compared to lower dimensional

simulations even though the fraction of accelerated ions is reduced. These findings may be of relevance for the design of future experiments on laser acceleration of ions up to relativistic (GeV) energy.

Finally, a generalized relativistic kinetic equation including radiation reaction effects has been discussed and we have shown that the radiation reaction force leads to a contraction of the available phase space volume. This prediction is in agreement with the results of our PIC simulations where we observed that radiation reaction effects lead both to an increased spatial bunching of electrons and ions and to a significant cooling of hot electrons.

Outlook

Future studies of relevant laser-plasma interaction regimes where radiation reaction effects may play a crucial role include: the role of radiation reaction on electron acceleration in the interaction with an underdense plasma where a noticeable fraction of ultra-relativistic electrons move into superintense laser fields, high-harmonic generation in the interaction of an ultra-intense laser pulse obliquely incident on a solid-density plasma slab where radiation reaction effects may strongly affect the electron dynamics at the front surface (where harmonics are generated) and collective non-linear Thomson scattering where a large number of electrons can be accelerated with a first laser pulse and then interact with a second counter-propagating laser pulse therefore maximizing the strength of the radiation reaction force and yielding an ultra-bright gamma-ray flash.

Above all, the main issue that has to be studied in depth is the role and the onset of quantum effects in the electron dynamics. Quantum effects include the role of spin degrees of freedom as we have discussed in section 1.2.1 and especially the transition from the continuum classical emission of radiation to the stochastic emission of photons with energies comparable with the electron rest energy in the instantaneous rest frame of the electron. This issue is indeed almost completely unexplored and partial results exist only for simple cases such as single photon emission from a single electron in a constant and uniform external magnetic field [67], or in constant and uniform crossed fields [66] or in a plane wave field [66]. We remark that at ultra-high

laser pulse intensities (normalized laser amplitude $a_0 \gg 1$) the external field must be included in the quantum description exactly i.e. perturbation theory is used to deal with the photon emission but cannot be used to deal with the external field making the issue quantum effects very hard to be dealt with for arbitrary external fields.

Furthermore, it has been shown recently that single photon emission *does not* account for "quantum radiation reaction" effects which amount to *multiple* photon emissions [18]. More precisely, it has been shown that the classical limit of a single photon emission from an electron in an external plane wave reproduces the result for the classical emission spectrum but without "classical radiation reaction" effects i.e. using the Lorentz force alone instead of the Lorentz and radiation reaction force to deduce the motion and the emission spectrum. Quantum radiation reaction effects have been therefore identified with multiple photon emissions and it has been shown by numerical integration that this multiple photon emission may lead to a significant deviation from the quantum prediction of the emission spectrum in the single photon emission approximation [18]. This suggests that even the few analytical results for the special cases mentioned above should be considered with caution.

Appendix A

Comparison of particle pushers

In this chapter, three leap-frog particle pushers for the Lorentz force are briefly discussed and compared from the point of view of both the numerical accuracy and the computational performance.

The Lorentz equations of motion for a particle of mass m and charge q are

$$\frac{d\mathbf{u}}{dt} = \frac{q}{m}\left(\mathbf{E} + \frac{\mathbf{u}}{\gamma c} \times \mathbf{B}\right) \tag{A.1}$$

$$\frac{d\mathbf{x}}{dt} = \frac{\mathbf{u}}{\gamma} \tag{A.2}$$

where $\mathbf{u} \equiv \gamma\mathbf{v}$ and $\gamma = \sqrt{1 + (\mathbf{u}/c)^2}$. The corresponding leap-frog equations are

$$\frac{\mathbf{u}^{n+1/2} - \mathbf{u}^{n-1/2}}{\Delta t} = \frac{q}{m}\left(\mathbf{E}^n + \frac{\bar{\mathbf{v}}^n}{c} \times \mathbf{B}^n\right) \tag{A.3}$$

$$\frac{\mathbf{x}^{n+1} - \mathbf{x}^n}{\Delta t} = \frac{\mathbf{u}^{n+1/2}}{\gamma^{n+1/2}} \tag{A.4}$$

where $\gamma^{n+1/2} = \sqrt{1 + (\mathbf{u}^{n+1/2}/c)^2}$. In the Boris approach (see Ref. [65])

$$\bar{\mathbf{v}}^n = \frac{\mathbf{u}^{n+1/2} + \mathbf{u}^{n-1/2}}{2\gamma^n} \tag{A.5}$$

and introducing the auxiliary vectors

$$\mathbf{u}^- = \mathbf{u}^{n-1/2} + \frac{q\Delta t\mathbf{E}^n}{2m} \tag{A.6}$$

$$\mathbf{u}^+ = \mathbf{u}^{n+1/2} - \frac{q\Delta t\mathbf{E}^n}{2m} \tag{A.7}$$

and substituting Eqs. (A.6, A.7) into Eq. (A.3) with the Boris choice for $\bar{\mathbf{v}}^n$ in Eq. (A.5), we get

$$\frac{\mathbf{u}^+ - \mathbf{u}^-}{\Delta t} = \frac{q}{2\gamma^n mc}\left(\mathbf{u}^+ + \mathbf{u}^-\right) \times \mathbf{B}^n \,. \tag{A.8}$$

Taking the scalar product of Eq. (A.8) with $(\mathbf{u}^+ + \mathbf{u}^-)$ we get $(\mathbf{u}^+)^2 = (\mathbf{u}^-)^2$ and therefore $\gamma^n = \sqrt{1 + (\mathbf{u}^-/c)^2} = \sqrt{1 + (\mathbf{u}^+/c)^2}$. Since we start with $u^{n-1/2}$ then $\gamma^n = \sqrt{1 + (\mathbf{u}^-/c)^2}$ is used in practice.

Eq. (A.8) results in a rotation about an axis parallel to $\mathbf{B}$ through an angle $\theta = -2\arctan(q\Delta t|\mathbf{B}^n|/2\gamma^n mc)$ and can be performed with the usual Boris' rotation (see Ref. [65] for details). In summary, a single Boris step-advance consists of the following sub-steps:

Step 1: Start with $\mathbf{u}^{n-1/2}$, half boost by the electric field

$$\mathbf{u}^- = \mathbf{u}^{n-1/2} + \frac{q\Delta t\mathbf{E}^n}{2m} \tag{A.9}$$

Step 2: Full rotation by the magnetic field

$$\gamma^n = \sqrt{1 + (\mathbf{u}^-)^2} \tag{A.10}$$

$$\mathbf{t} = \frac{q\mathbf{B}^n\Delta t}{2\gamma^n mc} \tag{A.11}$$

$$\mathbf{s} = \frac{2\mathbf{t}}{1 + \mathbf{t}^2} \tag{A.12}$$

then

$$\mathbf{u}' = \mathbf{u}^- + \mathbf{u}^- \times \mathbf{t} \tag{A.13}$$

$$\mathbf{u}^+ = \mathbf{u}^- + \mathbf{u}' \times \mathbf{s} \tag{A.14}$$

Step 3: Half boost by the electric field

$$\mathbf{u}^{n+1/2} = \mathbf{u}^+ + q\mathbf{E}^n\frac{\Delta t}{2} \tag{A.15}$$

Another possible approach is to algebraically solve Eq. (A.8). In fact, since $\gamma^n = \sqrt{1 + (\mathbf{u}^-/c)^2}$ is a known given quantity, we have to solve a linear system of algebraic equations Eq. (A.8) in the unknown $\mathbf{u}^+$. Recasting Eq. (A.8) as

$$\mathbf{u}^+ = \mathbf{u}' + (\mathbf{u}^+ \times \mathbf{t}) \tag{A.16}$$

where $\mathbf{t} = q\Delta t\mathbf{B}^n/2\gamma^n mc$ and $\mathbf{u}' = \mathbf{u}^- + \mathbf{u}^- \times \mathbf{t}$, then the solution of Eq. (A.16) is

$$\mathbf{u}^+ = s\left[\mathbf{u}' + (\mathbf{u}' \cdot \mathbf{t})\mathbf{t} + (\mathbf{u}' \times \mathbf{t})\right] = s\left[\mathbf{u}' + (\mathbf{u}^- \cdot \mathbf{t})\mathbf{t} + (\mathbf{u}' \times \mathbf{t})\right] \tag{A.17}$$

where $s = 1/(1+\mathbf{t}^2)$ and Eq. (A.17) replaces the step 2 of the Boris approach.

Another pusher has been proposed by Vay in Ref. [68] where the following velocity average

$$\bar{\mathbf{v}}^n = \frac{\mathbf{v}^{n+1/2} + \mathbf{v}^{n-1/2}}{2} = \frac{1}{2}\left(\frac{\mathbf{u}^{n+1/2}}{\gamma^{n+1/2}} + \frac{\mathbf{u}^{n-1/2}}{\gamma^{n-1/2}}\right) \tag{A.18}$$

substitutes the Boris velocity average in Eq. (A.5). Then, Eq. (A.3) with the velocity average in Eq. (A.18) is algebraically solved using $\gamma^{n+1/2} = \sqrt{1 + (\mathbf{u}^{n+1/2}/c)^2}$ as a known given quantity. Finally, $\gamma^{n+1/2}$ is deduced solving a fourth-order algebraic equation obtained[1] from $\gamma^2 = 1 + (\mathbf{u}/c)^2$ (see Ref. [68] for details).

We report the steps of the Vay approach:

Step 1: Get $\mathbf{u}^n$ from $\mathbf{u}^{n-1/2}$ using

$$\mathbf{u}^n = \mathbf{u}^{n-1/2} + \frac{q\Delta t}{2m}\left(\mathbf{E}^n + \frac{\mathbf{u}^{n-1/2}}{\gamma^{n-1/2}} \times \mathbf{B}^n\right) \tag{A.19}$$

Step 2: Get $\mathbf{u}^{n+1/2}$ from $\mathbf{u}^n$ using

$$\gamma^{n+1/2} = \sqrt{\frac{\sigma + \sqrt{\sigma^2 + 4(\vec{\tau}^2 + u*^2)}}{2}} \tag{A.20}$$

and

$$\mathbf{u}^{n+1/2} = s[\mathbf{u}' + (\mathbf{u}' \cdot \mathbf{t})\mathbf{t} + \mathbf{u}' \times \mathbf{t}] \tag{A.21}$$

where $\vec{\tau} = (q\Delta t/2m)\mathbf{B}^n$, $u* = \mathbf{u}' \cdot \vec{\tau}/c$, $\sigma = \gamma'^2 - \vec{\tau}^2$, $\gamma' = \sqrt{1 + \mathbf{u}'^2/c^2}$, $\mathbf{t} = \vec{\tau}/\gamma^{n+1/2}$, $s = 1/(1 + \mathbf{t}^2)$, and $\mathbf{u}' = \mathbf{u}^n + (q\Delta t/2m)\mathbf{E}^n$.

Finally, in every pusher the position is advanced according to

$$\mathbf{x}^{n+1} = \mathbf{x}^n + \frac{\mathbf{p}^{n+1/2}}{\gamma^{n+1/2}}\Delta t\ . \tag{A.22}$$

[1] Actually, the scalar product of the previously found solution with a suitable known quantity is taken, however this is conceptually the same approach.

We remark that the Vay pusher is comparatively much more complex and computationally expensive than the previously discussed pushers since more quantities have to be computed and in particular multiple square roots have to be computed for a single step-advance (see e.g. Eq. (A.20) and the computation of γ'). Furthermore, comparing the numerical prediction for an electron in a monochromatic plane wave using the *same* physical and numerical parameters, we have found that the Boris pusher and our modified pusher lead to nearly the same results while the Vay pusher leads to larger deviations from the analytical prediction.

Fig. A.1 shows the trajectory of an electron in a monochromatic plane wave in the "average rest frame" computed with a fourth-order Runge-Kutta method (black curve) and with the previously discussed leap-frog methods (red curve). In these simulations, the normalized laser intensity is $a_0 = 100$, the polarization parameter is $\delta = 0$ (see Eq. (2.16)) and the initial momentum is $p_{x_0} = -35.35\, mc$. It is apparent that the Vay method yields the largest deviations from the expected "figure of eight" although the simulations last the same time and have the same time-step $\Delta t = \omega^{-1}/100$.

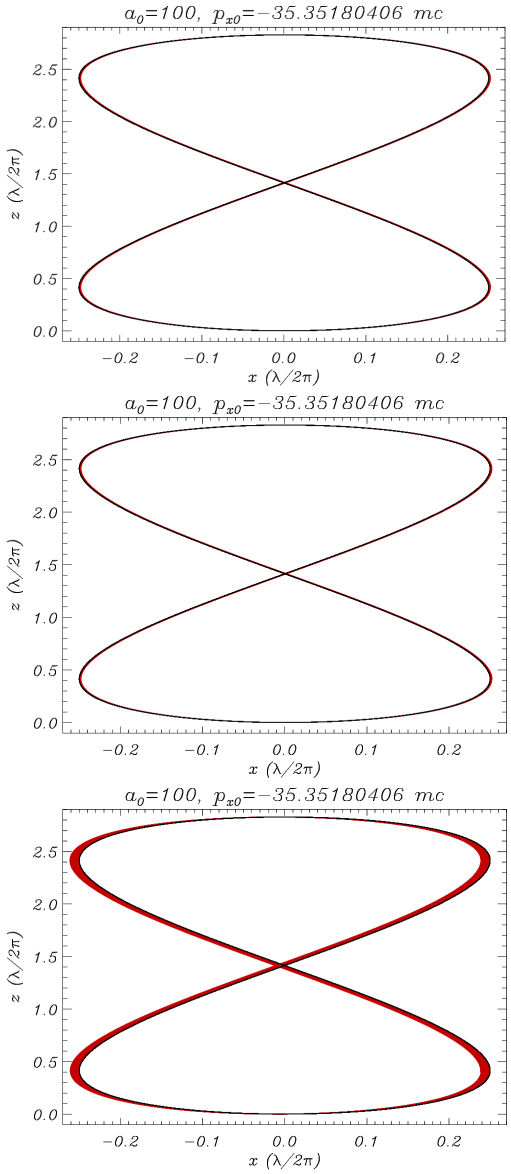

Figure A.1: First row: fourth-order Runge-Kutta prediction (black) and Boris pusher prediction (red). Second row: fourth-order Runge-Kutta prediction (black) and our modified pusher prediction (red). Third row: fourth-order Runge-Kutta prediction (black) and Vay pusher prediction (red).

Appendix B

Mathematical proofs

B.1 Contraction of the phase space: proof of the inequality

In this section we prove that for any $\mathbf{E}$ and $\mathbf{B}$ in the real domain and for any $\mathbf{v}$ such that $1 > |\mathbf{v}| \geq 0$ then

$$4\gamma \left[(\mathbf{v} \times \mathbf{E})^2 + (\mathbf{v} \times \mathbf{B})^2 - 2\mathbf{v} \cdot (\mathbf{E} \times \mathbf{B}) \right] + 2 \left[\frac{\mathbf{E}^2 + \mathbf{B}^2}{\gamma} \right] \geq 0 \,. \tag{B.1}$$

It is always possible to decompose the electromagnetic fields in the following way

$$\mathbf{E} = \mathbf{E}_\perp + \mathbf{E}_\parallel \qquad \mathbf{B} = \mathbf{B}_\perp + \mathbf{B}_\parallel \tag{B.2}$$

i.e. the field can be written as a superposition of the component perpendicular to $\mathbf{v}$ and of the component parallel to $\mathbf{v}$. It immediately follows that

$$\left[\frac{\mathbf{E}^2 + \mathbf{B}^2}{\gamma} \right] = \left[\frac{\mathbf{E}_\perp^2 + \mathbf{B}_\perp^2}{\gamma} \right] + \left[\frac{\mathbf{E}_\parallel^2 + \mathbf{B}_\parallel^2}{\gamma} \right] . \tag{B.3}$$

If

$$4\gamma \left[(\mathbf{v} \times \mathbf{E})^2 + (\mathbf{v} \times \mathbf{B})^2 - 2\mathbf{v} \cdot (\mathbf{E} \times \mathbf{B}) \right] + 2 \left[\frac{\mathbf{E}_\perp^2 + \mathbf{B}_\perp^2}{\gamma} \right] \geq 0 \tag{B.4}$$

then Eq. (B.1) is fulfilled i.e. Eq. (B.4) is a sufficient condition for the validity of Eq. (B.1). From our previous definitions we have

$$4\gamma \left[(\mathbf{v} \times \mathbf{E})^2 + (\mathbf{v} \times \mathbf{B})^2 - 2\mathbf{v} \cdot (\mathbf{E} \times \mathbf{B}) \right] =$$

$$= 4\gamma \left[\mathbf{v}^2\mathbf{E}_\perp^2 + \mathbf{v}^2\mathbf{B}_\perp^2 \mp 2|\mathbf{v}||\mathbf{E}_\perp||\mathbf{B}_\perp|\sin(\phi)\right] \tag{B.5}$$

where $\sin(\phi)$ with $\phi \in [0, \pi]$ is the angle included between $\mathbf{E}_\perp$ and $\mathbf{B}_\perp$ which lie in the plane perpendicular to $\mathbf{v}$ and we used the identity

$$\begin{aligned}\mathbf{v}\cdot(\mathbf{E}\times\mathbf{B}) &= \mathbf{v}\cdot\left[(\mathbf{E}_\perp+\mathbf{E}_\parallel)\times(\mathbf{B}_\perp+\mathbf{B}_\parallel)\right] = \mathbf{v}\cdot(\mathbf{E}_\perp\times\mathbf{B}_\perp) = \\ &= \pm|\mathbf{v}|\,|\mathbf{E}_\perp\times\mathbf{B}_\perp| = \pm|\mathbf{v}||\mathbf{E}_\perp||\mathbf{B}_\perp|\sin(\phi)\end{aligned} \tag{B.6}$$

which follows from the distributive property and from $\left(\mathbf{E}_\parallel \times \mathbf{B}_\parallel\right) = 0$ from the definition (B.2), $\mathbf{v}\cdot\left(\mathbf{E}_\parallel\times\mathbf{B}_\perp\right) = \mathbf{B}_\perp\cdot\left(\mathbf{v}\times\mathbf{E}_\parallel\right) = 0$ from the definition (B.2) and the same $\mathbf{v}\cdot\left(\mathbf{E}_\perp\times\mathbf{B}_\parallel\right) = -\mathbf{E}_\perp\cdot\left(\mathbf{v}\times\mathbf{B}_\parallel\right) = 0$ from the definition (B.2).

Using Eq. (B.5) we have that Eq. (B.4) becomes

$$4\gamma\left[\mathbf{v}^2\mathbf{E}_\perp^2 + \mathbf{v}^2\mathbf{B}_\perp^2 \mp 2|\mathbf{v}||\mathbf{E}_\perp||\mathbf{B}_\perp|\sin(\phi)\right] + 2\left[\frac{\mathbf{E}_\perp^2+\mathbf{B}_\perp^2}{\gamma}\right] \geq 0 \tag{B.7}$$

Each term of Eq. (B.7) is positive except when $(\mathbf{E}_\perp \times \mathbf{B}_\perp)$ is parallel to $\mathbf{v}$. In this last case we have a negative sign term $-2|\mathbf{v}||\mathbf{E}_\perp||\mathbf{B}_\perp|\sin(\phi)$. It is clear that $-2|\mathbf{v}||\mathbf{E}_\perp||\mathbf{B}_\perp|\sin(\phi) \geq -2|\mathbf{v}||\mathbf{E}_\perp||\mathbf{B}_\perp|$ and therefore in order to prove Eq. (B.7) it is sufficient to prove

$$4\gamma\left[\mathbf{v}^2\mathbf{E}_\perp^2 + \mathbf{v}^2\mathbf{B}_\perp^2 - 2|\mathbf{v}||\mathbf{E}_\perp||\mathbf{B}_\perp|\right] + 2\left[\frac{\mathbf{E}_\perp^2+\mathbf{B}_\perp^2}{\gamma}\right] \geq 0 \tag{B.8}$$

If $\mathbf{v} = 0$ the inequality (B.8) is fulfilled so we have to prove Eq. (B.8) when $1 > |\mathbf{v}| > 0$. Dividing Eq. (B.8) by 4γ

$$\left[\mathbf{v}^2(\mathbf{E}_\perp^2+\mathbf{B}_\perp^2) - 2|\mathbf{v}||\mathbf{E}_\perp||\mathbf{B}_\perp|\right] + \left[\frac{\mathbf{E}_\perp^2+\mathbf{B}_\perp^2}{2\gamma^2}\right] \geq 0 \tag{B.9}$$

and using the identity $\mathbf{v}^2 = 1 - 1/\gamma^2$ then Eq. (B.9) becomes

$$(\mathbf{E}_\perp^2+\mathbf{B}_\perp^2)\left[1-\frac{1}{2\gamma^2}\right] \geq 2|\mathbf{v}||\mathbf{E}_\perp||\mathbf{B}_\perp|\,. \tag{B.10}$$

We already showed that if $|\mathbf{v}| = 0$ then Eq. (B.8) is fulfilled, the same is true for $|\mathbf{E}| = 0$ or $|\mathbf{B}| = 0$. We can therefore assume that $|\mathbf{v}| > 0$ and $|\mathbf{E}| > 0$ and $|\mathbf{B}| > 0$ and rewrite Eq. (B.10) as

$$\frac{1}{|\mathbf{v}|}\left[1-\frac{1}{2\gamma^2}\right] \geq \frac{2|\mathbf{E}_\perp||\mathbf{B}_\perp|}{(\mathbf{E}_\perp^2+\mathbf{B}_\perp^2)} \tag{B.11}$$

It is straightforward to prove that

$$1 \geq \frac{2|\mathbf{E}_\perp||\mathbf{B}_\perp|}{(\mathbf{E}_\perp^2 + \mathbf{B}_\perp^2)}$$

since $(|\mathbf{E}_\perp| - |\mathbf{B}_\perp|)^2 \geq 0$. In order to prove Eq. (B.11) it is therefore sufficient to prove that

$$\frac{1}{|\mathbf{v}|}\left[1 - \frac{1}{2\gamma^2}\right] = \frac{1}{|\mathbf{v}|}\left[\frac{1}{2} + \frac{\gamma^2 - 1}{2\gamma^2}\right] \geq 1\,. \tag{B.12}$$

Using

$$\gamma^2 - 1 = \frac{\mathbf{v}^2}{1 - \mathbf{v}^2}$$

then Eq. (B.12) becomes

$$\frac{1}{2|\mathbf{v}|}\left[1 + \frac{\mathbf{v}^2}{\gamma^2(1 - \mathbf{v}^2)}\right] = \left[\frac{1}{2|\mathbf{v}|} + \frac{|\mathbf{v}|}{2}\right] \geq 1 \tag{B.13}$$

The function

$$\left[\frac{1}{2|\mathbf{v}|} + \frac{|\mathbf{v}|}{2}\right] \tag{B.14}$$

is regular in the domain $1 > |\mathbf{v}| > 0$. It is straightforward to prove that

$$\left[\frac{1}{2|\mathbf{v}|} + \frac{|\mathbf{v}|}{2}\right] \to +\infty \quad \text{for} \quad |\mathbf{v}| \to 0^+$$

$$\left[\frac{1}{2|\mathbf{v}|} + \frac{|\mathbf{v}|}{2}\right] \to +1 \quad \text{for} \quad |\mathbf{v}| \to 1$$

Calculating the derivative

$$\frac{d}{d|\mathbf{v}|}\left[\frac{1}{2|\mathbf{v}|} + \frac{|\mathbf{v}|}{2}\right] = \frac{|\mathbf{v}|^2 - 1}{2|\mathbf{v}|^2} \leq 0 \quad \text{in the domain} \quad 1 > |\mathbf{v}| > 0$$

it follows that the function (B.14) is monotonically decreasing and the lower bound is +1, hence Eq. (B.13) is fulfilled. Q.E.D.

B.2 Evolution of the phase space volume

In this section we deduce the equation that provides the temporal evolution of an infinitesimal volume of a $6n$-dimensional phase-space where n is the number of particles.

Temporal evolution can be considered as a coordinate transformation in the phase space and is described by the equations of motion that we assume to be (normalizing momenta in units of mc and velocities in units of c):

$$\dot{\mathbf{q}}_l(t) = \mathbf{p}_l(t)/\sqrt{1+\mathbf{p}_l^2(t)} \tag{B.15}$$

$$\dot{\mathbf{p}}_l(t) = \mathbf{F}(\mathbf{q}_l, \mathbf{p}_l, t) \qquad l = 1, \ldots, n \tag{B.16}$$

where $\dot{\mathbf{q}}_l(t)$ depends only on $\mathbf{p}_l(t)$ and does not depend on $\mathbf{q}_l(t)$. We mention that in Hamiltonian mechanics $\dot{\mathbf{q}}_l(t)$ may be a function of both the canonical momentum $\mathbf{P}_l(t)$ and the canonical coordinate $\mathbf{q}_l(t)$. For instance, in non-relativistic mechanics the equation $\dot{\mathbf{q}}(t) = \frac{\partial H}{\partial \mathbf{P}}$ for an electron in an external electromagnetic field becomes

$$\dot{\mathbf{q}}(t) = \mathbf{P}(t) - \frac{e}{mc}\mathbf{A}(\mathbf{q}, t) \tag{B.17}$$

The infinitesimal volume element at $t = 0$

$$dx_0 = d\mathbf{q}_1(0) \ldots d\mathbf{q}_n(0)\, d\mathbf{p}_1(0) \ldots d\mathbf{p}_n(0) \tag{B.18}$$

evolves in the infinitesimal volume at time t

$$dx_t = d\mathbf{q}_1(t) \ldots d\mathbf{q}_n(t)\, d\mathbf{p}_1(t) \ldots d\mathbf{p}_n(t)\,. \tag{B.19}$$

The relationship between the two volumes is given by the modulus of the Jacobian

$$dx_t = |J| dx_0 \tag{B.20}$$

with

$$J \equiv \det(M) \tag{B.21}$$

where

$$M_{ij} = \frac{\partial x_t^i}{\partial x_0^j} \tag{B.22}$$

From Eq.(B.20) or equivalently from Eq.(B.22) it follows that $J = 1$ at $t = 0$, which provides the initial condition.

Taking the time derivative of J and using Jacobi's formula for the derivative of a determinant we get

$$\frac{dJ}{dt} = \mathrm{tr}\left(\mathrm{adj}(M)\frac{dM}{dt}\right) \tag{B.23}$$

where adj(M) is the classical adjoint (or "adjugate") of M i.e. the transposed of the cofactor matrix of M.

Assuming $J(0) = 1$ then M is invertible at least in a neighborhood of $t = 0$ and from the Cramer rule and Laplace expansion for the determinant

$$M^{-1} = \frac{\text{adj}(M)}{\det(M)} = J^{-1}\text{adj}(M) \tag{B.24}$$

Substituting Eq. (B.24) in Eq. (B.23) and using the linearity of the trace we have

$$\frac{dJ}{dt} = J \,\text{tr}\left(M^{-1}\frac{dM}{dt}\right) \tag{B.25}$$

and recalling that

$$M^{-1}_{ij} = \frac{\partial x^i_0}{\partial x^j_t} \tag{B.26}$$

and

$$\frac{dM_{ij}}{dt} = \frac{\partial \dot{x}^i_t}{\partial x^j_0} \tag{B.27}$$

we get

$$\text{tr}\left(M^{-1}\frac{dM}{dt}\right) = \sum_{i,j=1}^{6n} M^{-1}_{ij}\frac{dM_{j,i}}{dt} = \sum_{i,j=1}^{6n}\frac{\partial x^i_0}{\partial x^j_t}\frac{\partial \dot{x}^j_t}{\partial x^i_0} = \sum_{j=1}^{6n}\frac{\partial \dot{x}^j_t}{\partial x^j_t} = \nabla_{x_t}\cdot\dot{x}_t \tag{B.28}$$

that is a divergence in the $6n$-dimensional phase-space. Eq. (B.25) therefore becomes

$$\frac{dJ}{dt} = J\,\nabla_{x_t}\cdot\dot{x}_t \tag{B.29}$$

or equivalently in terms of $q(t)$ and $p(t)$

$$\nabla_{x_t}\cdot\dot{x}_t = \sum_{i=1}^{3n}\frac{\partial \dot{q}_i}{\partial q_i} + \sum_{i=1}^{3n}\frac{\partial \dot{p}_i}{\partial p_i} = \sum_{l=1}^{n}\nabla_{\mathbf{q}_l}\cdot\dot{\mathbf{q}}_l + \sum_{l=1}^{n}\nabla_{\mathbf{p}_l}\cdot\dot{\mathbf{p}}_l \tag{B.30}$$

For an Hamiltonian system

$$\dot{\mathbf{q}}_l(t) = \frac{\partial H}{\partial \mathbf{P}_l} \tag{B.31}$$

$$\dot{\mathbf{P}}_l(t) = -\frac{\partial H}{\partial \mathbf{q}_l} \qquad l = 1,\ldots,n \tag{B.32}$$

then

$$\sum_{i=1}^{3n} \frac{\partial \dot{q}_i}{\partial q_i} + \sum_{i=1}^{3n} \frac{\partial \dot{P}_i}{\partial P_i} = \sum_{i=1}^{3n} \frac{\partial^2 H}{\partial q_i \partial P_i} - \sum_{i=1}^{3n} \frac{\partial^2 H}{\partial P_i \partial q_i} = 0 \tag{B.33}$$

and the phase-space volume is conserved.

In our case, from Eqs. (B.15, B.16) and from Eq. (B.29) we have

$$\frac{dJ}{dt} = J \sum_{l=1}^{n} \nabla_{\mathbf{p}_l} \cdot \mathbf{F}(\mathbf{q}_l, \mathbf{p}_l, t)\,, \qquad J(0) = 1 \tag{B.34}$$

since $\nabla_{\mathbf{q}_l} \cdot \dot{\mathbf{q}}_l = 0$ because $\dot{\mathbf{q}}_l$ depends only on $\mathbf{p}_l$. Q.E.D.

B.3 The PIC method with RR

In this section we prove that the standard particle-in-cell (PIC) approach holds even when $\nabla_{\mathbf{p}} \cdot \mathbf{F} \neq 0$ where $\mathbf{F} = \mathbf{F}(\mathbf{x}, \mathbf{p}, t)$ is the total force.

In order to keep the notation as simple as possible we use the dimensionless quantities introduced in Eq. (2.11). The relativistic distribution function $f = f(\mathbf{x}, \mathbf{p}, t)$ evolves according to the collisionless transport equation

$$\frac{\partial f}{\partial t} + \nabla_{\mathbf{x}} \cdot (f\,\mathbf{v}) + \nabla_{\mathbf{p}} \cdot (f\,\mathbf{F}) = 0\,, \tag{B.35}$$

where $\mathbf{x}$ are the spatial coordinates, $\mathbf{v} = \mathbf{p}/\gamma(\mathbf{p})$ is the three-dimensional velocity and $\gamma = \sqrt{1 + \mathbf{p}^2}$ is the relativistic factor.

In the PIC approach a discrete representation of the distribution function is assumed

$$f(\mathbf{x}, \mathbf{p}, t) = f_0 \sum_{i=1}^{N} g[\mathbf{x} - \mathbf{x}_i(t)] \delta[\mathbf{p} - \mathbf{p}_i(t)] \tag{B.36}$$

where N is the number of computational particles or quasi-particles that provide a representation of the distribution function f, the constant f_0 is a proper normalization factor, $\mathbf{x}_i(t)$ and $\mathbf{p}_i(t)$ are the quasi-particle trajectories in the phase-space, $g[\mathbf{x} - \mathbf{x}_i(t)]$ is the spatial 'shape' of the quasi-particle while $\delta[\mathbf{p} - \mathbf{p}_i(t)]$ it the Dirac delta. The typical choice is therefore to have a point-like 'shape' in the momentum space and an extended 'shape' in the real space. In principle, the choice $g[\mathbf{x} - \mathbf{x}_i(t)] = \delta[\mathbf{x} - \mathbf{x}_i(t)]$ is also possible although not convenient in practice since it would lead to an increased

'numerical noise' in the current and in the fields (when the current is inserted in Maxwell's equations). In fact, Maxwell's equations are solved with an 'Eulerian' approach i.e. on a grid or 'mesh' with a well defined spatial and temporal step so that when a point-like particle cross from a cell to another cell of the mesh it yields a sudden jump in the current. This issue is not present for momentum coordinates since a 'Lagrangian' approach is used for the evolution of the computational particles and the momentum space is continuous (i.e. no grid is used for momentum space).

The discrete representation (B.36) is a simple way to switch from an Eulerian description to a Lagrangian description where we follow the trajectories of the quasi-particles in the phase-space. Hence, in this description the unknown quantities are the Lagrangian coordinates $\mathbf{x}_i(t)$ and $\mathbf{p}_i(t)$ and their temporal evolution has to be deduced substituting Eq. (B.36) into Eq. (B.35). Taking the partial time derivative of f

$$\begin{aligned}\partial_t f &= -f_0 \sum_{i=1}^{N} \Big\{ \delta[\mathbf{p}-\mathbf{p}_i(t)]\dot{\mathbf{x}}_i(t)\cdot\nabla_{\mathbf{x}} g[\mathbf{x}-\mathbf{x}_i(t)] \\ &\quad + g[\mathbf{x}-\mathbf{x}_i(t)]\dot{\mathbf{p}}_i(t)\cdot\nabla_{\mathbf{p}}\delta[\mathbf{p}-\mathbf{p}_i(t)]\Big\} \\ &= -f_0 \sum_{i=1}^{N} \Big\{ \nabla_{\mathbf{x}}\cdot\Big(\dot{\mathbf{x}}_i(t) g[\mathbf{x}-\mathbf{x}_i(t)]\delta[\mathbf{p}-\mathbf{p}_i(t)]\Big) \\ &\quad + \nabla_{\mathbf{p}}\cdot\Big(\dot{\mathbf{p}}_i(t) g[\mathbf{x}-\mathbf{x}_i(t)]\delta[\mathbf{p}-\mathbf{p}_i(t)]\Big)\Big\} \end{aligned} \tag{B.37}$$

and Eq. (B.35) becomes

$$\begin{aligned}&\sum_{i=1}^{N}\Big\{\nabla_{\mathbf{x}}\cdot\Big[\Big(\frac{\mathbf{p}}{\gamma(\mathbf{p})}-\dot{\mathbf{x}}_i(t)\Big)g[\mathbf{x}-\mathbf{x}_i(t)]\delta[\mathbf{p}-\mathbf{p}_i(t)]\Big] + \\ &+\nabla_{\mathbf{p}}\cdot\Big[\Big(\mathbf{F}(\mathbf{x},\mathbf{p},t)-\dot{\mathbf{p}}_i(t)\Big)g[\mathbf{x}-\mathbf{x}_i(t)]\delta[\mathbf{p}-\mathbf{p}_i(t)]\Big]\Big\} = 0 \end{aligned} \tag{B.38}$$

Integrating Eq. (B.38) in momentum space $d\mathbf{p}$, using the divergence theorem and recalling that the flux of $\Big[\Big(\mathbf{F}(\mathbf{x},\mathbf{p},t)-\dot{\mathbf{p}}_i(t)\Big)g[\mathbf{x}-\mathbf{x}_i(t)]\delta[\mathbf{p}-\mathbf{p}_i(t)]\Big]$ is zero for $|\mathbf{p}|\to\infty$ then

$$\sum_{i=1}^{N}\nabla_{\mathbf{x}}\cdot\Big[\Big(\frac{\mathbf{p}_i(t)}{\gamma(\mathbf{p}_i(t))}-\dot{\mathbf{x}}_i(t)\Big)g[\mathbf{x}-\mathbf{x}_i(t)]\Big] =$$

$$= \sum_{i=1}^{N} \left[\Big(\frac{\mathbf{p}_i(t)}{\gamma(\mathbf{p}_i(t))} - \dot{\mathbf{x}}_i(t) \Big) \right] \cdot \nabla_{\mathbf{x}} g[\mathbf{x} - \mathbf{x}_i(t)] = 0 \tag{B.39}$$

Since $\nabla_{\mathbf{x}} g \neq 0$, the solution of Eq. (B.39) is:

$$\dot{\mathbf{x}}_i(t) = \frac{\mathbf{p}_i(t)}{\gamma(\mathbf{p}_i(t))} \tag{B.40}$$

because coordinates corresponding to a different index i are independent. Integrating Eq. (B.38) in space $d\mathbf{x}$, using the divergence theorem and recalling that the flux of $\left[\Big(\mathbf{p}/\gamma(\mathbf{p}) - \dot{\mathbf{x}}_i(t) \Big) g[\mathbf{x} - \mathbf{x}_i(t)] \delta[\mathbf{p} - \mathbf{p}_i(t)] \right]$ is zero for $|\mathbf{x}| \to \infty$ then

$$\begin{aligned}
&\sum_{i=1}^{N} \nabla_{\mathbf{p}} \cdot \left[\int \Big(\mathbf{F}(\mathbf{x}, \mathbf{p}, t) - \dot{\mathbf{p}}_i(t) \Big) g[\mathbf{x} - \mathbf{x}_i(t)] \delta[\mathbf{p} - \mathbf{p}_i(t)] \, d\mathbf{x} \right] = \\
&= \sum_{i=1}^{N} \nabla_{\mathbf{p}} \cdot \left[\int \mathbf{F}(\mathbf{x}, \mathbf{p}, t) g[\mathbf{x} - \mathbf{x}_i(t)] \delta[\mathbf{p} - \mathbf{p}_i(t)] \, d\mathbf{x} - \dot{\mathbf{p}}_i(t) \delta[\mathbf{p} - \mathbf{p}_i(t)] \right] = \\
&= \sum_{i=1}^{N} \left[\int \mathbf{F}(\mathbf{x}, \mathbf{p}_i(t), t) g[\mathbf{x} - \mathbf{x}_i(t)] \, d\mathbf{x} - \dot{\mathbf{p}}_i(t) \right] \cdot \nabla_{\mathbf{p}} \delta[\mathbf{p} - \mathbf{p}_i(t)] = 0
\end{aligned} \tag{B.41}$$

where we have assumed that $\int g[\mathbf{x} - \mathbf{x}_i(t)] \, d\mathbf{x} = 1$ and we have used the following result for a distribution

$$\nabla_{\mathbf{p}} \cdot \Big[\mathbf{F}(\mathbf{x}, \mathbf{p}, t) \delta[\mathbf{p} - \mathbf{p}_i(t)] \Big] = \mathbf{F}(\mathbf{x}, \mathbf{p}_i(t), t) \cdot \nabla_{\mathbf{p}} \delta[\mathbf{p} - \mathbf{p}_i(t)] \tag{B.42}$$

The solution of Eq. (B.41) is

$$\dot{\mathbf{p}}_i(t) = \int \mathbf{F}(\mathbf{x}, \mathbf{p}_i(t), t) g[\mathbf{x} - \mathbf{x}_i(t)] \, d\mathbf{x} \tag{B.43}$$

because coordinates corresponding to a different index i are independent. The problem of solving the kinetic equation for the distribution function f is therefore reduced to the problem of solving a system of $2N$ ordinary differential equations i.e. Eqs. (B.40, B.43) for the computational particles. Q.E.D.

Bibliography

[1] V. Yanovsky, V. Chvykov, G. Kalinchenko, P. Rousseau, T. Planchon, T. Matsuoka, A. Maksimchuk, J. Nees, G. Cheriaux, G. Mourou, and K. Krushelnick, "Ultra-high intensity- 300-TW laser at 0.1 Hz repetition rate", Opt. Express **16**, 2109-2114 (2008).

[2] See the ELI homepage at http://www.extreme-light-infrastructure.eu/

[3] See the HiPER homepage at http://www.hiper-laser.org/

[4] M. Marklund and P. K. Shukla, "Nonlinear collective effects in photon-photon and photon-plasma interactions", Rev. Mod. Phys. **78**, 591-640 (2006).

[5] G. A. Mourou, T. Tajima, and S. V. Bulanov, "Optics in the relativistic regime", Rev. Mod. Phys. **78**, 309-371 (2006).

[6] T. Tajima, D. Habs, X. Yan, "Laser Acceleration of Ions for Radiation Therapy", Rev. Accel. Sci. and Tech. Vol.**2**, 201-228 (2009).

[7] U. Teubner, P. Gibbon, "High-order harmonics from laser-irradiated plasma surfaces", Rev. Mod. Phys. **81**, 445-479 (2009).

[8] A. Macchi, M. Borghesi, M. Passoni, "Ion Acceleration by Superintense Laser Pulses: from Classic Problems to Advanced Applications", Rev. Mod. Phys., *submitted* (2011).

[9] S. V. Bulanov, T. Zh. Esirkepov, D. Habs, F. Pegoraro, T. Tajima, "Relativistic laser-matter interaction and relativistic laboratory astrophysics", Eur. Phys. J. D **55**, 483-507 (2009).

[10] J. Koga, T. Zh. Esirkepov, S. V. Bulanov, "Nonlinear Thomson scattering in the strong radiation damping regime", Phys. Plasmas **12**, 093106 (2005).

[11] M. Tamburini, F. Pegoraro, A. Di Piazza, C. H. Keitel and A Macchi, "Radiation reaction effects on radiation pressure acceleration", New J. Phys., **12** 123005 (2010).

[12] M. Tamburini, F. Pegoraro, A. Di Piazza, C. H. Keitel, T. V. Liseykina, A. Macchi, "Radiation reaction effects on electron nonlinear dynamics and ion acceleration in laser-solid interaction", Nucl. Instr. Meth. Phys. Res. A **653** 181-185 (2011).

[13] M. Tamburini, T. V. Liseykina, F. Pegoraro and A. Macchi, "Radiation Pressure Dominant Acceleration: Polarization and Radiation Reaction Effects in Three Dimensional Particle-In-Cell Simulations", *submitted*, (2011); arXiv:1108.2372v2.

[14] N. V. Elkina, A. M. Fedotov, I. Yu. Kostyukov, M. V. Legkov, N. B. Narozhny, E. N. Nerush, and H. Ruhl, "QED cascades induced by circularly polarized laser fields", Phys. Rev. ST Accel. Beams **14**, 054401 (2011).

[15] Y. Hadad, L. Labun, J. Rafelski, N. Elkina, C. Klier, H. Ruhl, "Effects of radiation reaction in relativistic laser acceleration", Phys. Rev. D **82**, 096012 (2010).

[16] M. W. Walser, C. H. Keitel, "Geometric and Algebraic Approach to Classical Dynamics of a Particle with Spin", Lett. Math. Phys. **55**, 63-70 (2001).

[17] A. Di Piazza, K. Z. Hatsagortsyan, C. H. Keitel, "Strong Signatures of Radiation Reaction below the Radiation-Dominated Regime", Phys. Rev. Lett. **102**, 254802 (2009).

[18] A. Di Piazza, K. Z. Hatsagortsyan, C. H. Keitel, "Quantum Radiation Reaction Effects in Multiphoton Compton Scattering", Phys. Rev. Lett. **105**, 220403 (2010).

[19] T. Esirkepov, M. Borghesi, S. V. Bulanov, G. Mourou, T. Tajima, "Highly Efficient Relativistic-Ion Generation in the Laser-Piston Regime", Phys. Rev. Lett. **92**, 175003 (2004).

[20] I. V. Sokolov, N. M. Naumova, J. A. Nees, G. A. Mourou, V. P. Yanovsky, "Dynamics of emitting electrons in strong laser fields", Phys. Plasmas **16**, 093115 (2009).

[21] I. V. Sokolov, N. M. Naumova, J. A. Nees, "Numerical modeling of radiation-dominated and quantum-electrodynamically strong regimes of laser-plasma interaction", Phys. Plasmas **18**, 093109 (2011).

[22] P. Gibbon, *Short pulse laser interaction with matter: an introduction*, (Imperial College Press, 2005), Par. 3.4.

[23] N. Naumova, T. Schlegel, V. T. Tikhonchuk, C. Labaune, I. V. Sokolov and G. Mourou, "Ponderomotive ion acceleration in dense plasmas at super-high laser intensities", Eur. Phys. J. D **55**, 393-398 (2009).

[24] A. Zhidkov, J. Koga, A. Sasaki, M. Uesaka, "Radiation Damping Effects on the Interaction of Ultraintense Laser Pulses with an Overdense Plasma", Phys. Rev Lett. **88**, 185002 (2002).

[25] M. Chen, A. Pukhov, T. P. Yu, Z. M. Sheng, "Radiation reaction effects on ion acceleration in laser foil interaction", Plasma Phys. Control. Fusion **53** 014004 (2011).

[26] N. Naumova, T. Schlegel, V. T. Tikhonchuk, C. Labaune, I. V. Sokolov, G. Mourou, "Hole Boring in a DT Pellet and Fast-Ion Ignition with Ultraintense Laser Pulses", Phys. Rev. Lett. **102**, 025002 (2009).

[27] T. Schlegel, N. Naumova, V. T. Tikhonchuk, C. Labaune, I. V. Sokolov and G. Mourou, "Relativistic laser piston model: Ponderomotive ion acceleration in dense plasmas using ultraintense laser pulses", Phys. Plasmas **16**, 083103 (2009).

[28] N. P. Klepikov, "Radiation damping forces and radiation from charged particles", Sov. Phys. Usp. **28**, 506-520 (1985).

[29] H. Spohn, *Dynamics of charged particles and their radiation field*, (Cambridge University Press, Cambridge, 2004).

[30] F. Rohrlich, *Classical Charged Particles*, Third Edition (World Scientific, Singapore, 2007).

[31] F. Rohrlich, "The correct equation of motion of a classical point charge", Phys. Lett. A **283**, 276-278 (2001).

[32] F. Rohrlich, "Dynamics of a charged particle", Phys. Rev. E **77**, 046609 (2008).

[33] G. W. Ford, R. F. O'Connell, "Radiation reaction in electrodynamics and the elimination of runaway solutions", Phys. Lett. A **157**, 217-220 (1991).

[34] G. W. Ford, R. F. O'Connell, "Relativistic form of radiation reaction", Phys. Lett. A **174**, 182-184 (1993).

[35] H. Spohn, "The critical manifold of the Lorentz-Dirac equation", Europhys. Lett. **50**, 287-292 (2000).

[36] S. E. Gralla, A. I. Harte, R. M. Wald, "Rigorous derivation of electromagnetic self-force", Phys. Rev. D **80**, 024031 (2009).

[37] L. D. Landau, E. M. Lifshitz, *The Classical Theory of Fields*, second edition (Elsevier, Oxford, 1975), Par. 74-76.

[38] S. G. Rajeev, "Exact solution of the Landau-Lifshitz equations for a radiating charged particle in the Coulomb potential", Ann. Phys. **323**, 2654-2661 (2008).

[39] A. Di Piazza, "Exact solution of the Landau-Lifshitz equation in a plane wave", Lett. Math. Phys. **83**, 305-313 (2008).

[40] R. Hakim, A. Mangeney, "Relativistic Kinetic Equations Including Radiation Effects. I. Vlasov Approximation", J. Math. Phys. **9**, 116-130 (1968).

[41] R. Hakim, A. Mangeney, "Collective Oscillations of a Relativistic Radiating Electron Plasma", Phys. Fluids **14**, 2751-2761 (1971).

[42] R. D. Hazeltine, S. M. Mahajan, "Radiation reaction in fusion plasmas", Phys. Rev. E **70**, 046407 (2004).

[43] V. I. Berezhiani, R. D. Hazeltine, S. M. Mahajan, "Radiation reaction and relativistic hydrodynamics", Phys. Rev. E **69**, 056406 (2004).

[44] R. D. Hazeltine, S. M. Mahajan, "Closed fluid description of relativistic, magnetized plasma interacting with radiation field", Phys. Rev. E **70**, 036404 (2004).

[45] V. I. Berezhiani, S. M. Mahajan, Z. Yoshida, "Plasma acceleration and cooling by strong laser field due to the action of radiation reaction force", Phys. Rev. E **78**, 066403 (2008).

[46] L. S. Kuz'menkov, "The Bogolyubov hierarchy of equations for relativistic systems. Radiation damping of waves in a plasma", Dokl. Akad. Nauk. SSSR **241**, 322-325 (1978), [Sov. Phys. Dokl. **23**, 469-471 (1978)].

[47] M. Kunze, A. Rendall, "The Vlasov-Poisson system with radiation damping", Ann. H. Poincaré **2**, 857-886.

[48] F. Rohrlich, "The dynamics of a charged sphere and the electron", Am. J. Phys. **65**, 1051-1057 (1997).

[49] F. Pegoraro, S. V. Bulanov, "Photon Bubbles and Ion Acceleration in a Plasma Dominated by the Radiation Pressure of an Electromagnetic Pulse", Phys. Rev. Lett. **99**, 065002 (2007).

[50] S. V. Bulanov, E. Y. Echkina, T. Zh. Esirkepov, I. N. Inovenkov, M. Kando, F. Pegoraro, G. Korn, "Unlimited Ion Acceleration by Radiation Pressure", Phys. Rev. Lett. **104**, 135003 (2010).

[51] E. J. Moniz, D. H. Sharp, "Absence of runaways and divergent self-mass in nonrelativistic quantum electrodynamics", Phys. Rev. D **10**, 1133-1136 (1974).

[52] E. J. Moniz, D. H. Sharp, "Radiation reaction in nonrelativistic quantum electrodynamics", Phys. Rev. D **15**, 2850-2865 (1977).

[53] J. D. Jackson, *Classical Electrodynamics*, third edition, (John Wiley & Sons, New York, 1999).

[54] A. Macchi, F. Cattani, T. V. Liseykina, F. Cornolti, "Laser Acceleration of Ion Bunches at the Front Surface of Overdense Plasmas", Phys. Rev. Lett. **94**, 165003 (2005).

[55] A. Macchi, T. V. Liseikina, S. Tuveri, S. Veghini, "Theory and simulation of ion acceleration with circularly polarized laser pulses", C. R. Physique **10**, 207-215 (2009).

[56] A. Macchi, S. Veghini, T. V. Liseykina, F. Pegoraro, "Radiation pressure acceleration of ultrathin foils", New J. Phys. **12**, 045013 (2010).

[57] A. Macchi, Silvia Veghini, Francesco Pegoraro, "Light Sail Acceleration Reexamined", Phys. Rev. Lett. **103**, 085003 (2009).

[58] X. Zhang, B. Shen, X. Li, Z. Jin, F. Wang, M. Wen, "Efficient GeV ion generation by ultraintense circularly polarized laser pulse", Phys. Plasmas **14**, 123108 (2007).

[59] A. P. L. Robinson, M. Zepf, S. Kar, R. G. Evans, C. Bellei, "Radiation pressure acceleration of thin foils with circularly polarized laser pulses", New J. Phys. **10**, 013021 (2008).

[60] O. Klimo, J. Psikal, J. Limpouch, V. T. Tikhonchuk, "Monoenergetic ion beams from ultrathin foils irradiated by ultrahigh-contrast circularly polarized laser pulses", Phys. Rev. ST Accel. Beams **11**, 031301 (2008).

[61] L. Yin, B. J. Albright, K. J. Bowers, D. Jung, J. C. Fernandez, B. M. Hegelich, "Three-Dimensional Dynamics of Breakout Afterburner Ion Acceleration Using High-Contrast Short-Pulse Laser and Nanoscale Targets", Phys. Rev. Lett. **107**, 045003 (2011).

[62] C. J. Eliezer, "On the Classical Theory of Particles", Proc. Royal Soc. London Ser. A **194**, 543-555 (1948), Eq. (52).

[63] M. Ribaric, L. Sustersic, "Qualitative properties of an equation of motion of a classical point charge", Phys. Lett. A **295**, 318-319 (2002).

[64] W. E. Baylis, J. Huschilt, "Energy balance with the Landau-Lifshitz equation", Phys. Lett. A **301**, 7-12 (2002).

[65] C. K. Birdsall, A. B. Langdon, *Plasma Physics Via Computer Simulation*, (Institute of Physics, Bristol, 1991).

[66] V. I. Ritus, "Quantum effects of the interaction of elementary particles with an intense electromagnetic field", J. Sov. Laser Res. **6**, 497-617 (1985).

[67] V. B. Berestetskii, E. M. Lifshitz, L. P. Pitaevskii, *Quantum Electrodynamics*, 2nd Ed., Pergamon Press, 1982.

[68] J.-L. Vay, "Simulation of beams or plasmas crossing at relativistic velocity", Phys. Plasmas **15**, 056701 (2008).

HPC-Europa2 project, publications, talks and schools

HPC-Europa2 project

Title: **UMKAupgrade** Abstract appl. **711**

- Objectives:

  One of the main research activities of both our group and of the host institution is to investigate the strongly non-linear dynamics of super-intense laser-plasma interactions with multi-dimensional particle-in-cell simulations (PIC). To this aim, we already performed multi-D PIC simulations of laser-foil interaction at ultra-high intensities using the FORTRAN77 based PIC code "UMKA" which was developed by one of the members of the host institution (T. Liseykina). However, this code needed to be improved in order to make it more suitable for larger high resolution simulations. In particular, a more efficient I/O management and load balancing strategy had to be developed in order to enhance the efficiency and flexibility of the code e.g. allowing a restart with a different number of computational elements and to make the data portable on different platforms.

  The objectives of this project were therefore twofold: the first was to improve the existing PIC code "UMKA", in particular the I/O management by implementing the HDF5 library and performing tests of scalability; the second was to strengthen our collaboration with the host institution by starting up a joint project of code upgrade and de-

velopment, which may eventually allow to present a large joint project to be performed in one of the European supercomputing facilities.

- Achievements:

  The code improvement were performed on the 2D version of the particle-in-cell code "UMKA". In particular:

  1. A new procedure that performs an automatic backup of data forcing a checkpoint before reaching the wall-clock time or when some processing element is overloaded was introduced to avoid crash with loss of data and waste of computational resources.
  2. The whole I/O management is performed using the HDF5 library. A single file is generated for each checkpoint instead of a file for each processing element for each checkpoint. This assures efficient parallel I/O and data portability. Moreover, there is no longer need to restart with the same number of processing elements.
  3. A dynamic domain management and a simple load balancing strategy were developed and implemented in the code at the checkpoint level. It is possible to restart from checkpoint with a different number of processing elements. The domain for the fields as well as the number of particles managed by each processing element is assigned at restart in order to have an initial load balanced set-up.

  Several other improvements and optimizations are left for future work continuing our joint project of code development in collaboration with the host institution. In particular, the new dynamic domain management implemented in the code allows to introduce a simple dynamic load balancing strategy at run-time. Furthermore, communication and memory management may be improved, the code should be fully ported from FORTRAN77 to FORTRAN90.

Other research projects and grants

- February 2011 - August 2011: research grant from CNR-INO, "Teoria e simulazione Particle-In-Cell dell'accelerazione di ioni in regimi di intensità estreme" in the framework of the project SULDIS - "Superintense Laser-Driven Ion Sources".

- July 2010 - July 2011: ISCRA-CINECA "Class A" Supercomputing Project TOFUSEX - Towards Full-Scale Simulations of Laser-Plasma Interaction Experiments, as a staff member of the local research unity of Pisa. Principal investigator Dr. Andrea Macchi (CNR-INO Pisa, Italy).

Publications in peer reviewed journals

1. M. Tamburini, T. V. Liseykina, F. Pegoraro and A. Macchi, "Radiation pressure dominant acceleration: polarization and radiation reaction effects in three dimensional particle-in-cell simulations", *submitted*, arXiv:1108.2372v2 (2011).

2. M. Tamburini, F. Pegoraro, A. Di Piazza, C. H. Keitel, T. V. Liseykina, A. Macchi, "Radiation reaction effects on electron nonlinear dynamics and ion acceleration in laser-solid interaction", *Nuclear Instruments and Methods in Physics Research A* **653** 181-185 (2011).

3. M. Tamburini, F. Pegoraro, A. Di Piazza, C. H. Keitel and A. Macchi, "Radiation reaction effects on radiation pressure acceleration", *New Journal of Physics* **12**, 123005 (2010).

Conference Proceedings

1. A. Macchi, M. Tamburini, F. Pegoraro, T. V. Liseykina, "Radiation friction modeling in superintense laser-plasma interactions", Harnessing Relativistic Plasma Waves as Novel Radiation Sources from Tera-

hertz to X-Rays and Beyond II. Proceedings SPIE 8075, 807509 (2011); doi:10.1117/12.889127

2. A. Macchi, M. Tamburini, S. Veghini, F. Pegoraro, A. Di Piazza, C. H. Keitel, "Radiation pressure and radiation reaction effects in laser-solid interaction", LAT 2010: International Conference on Lasers, Applications, and Technologies, Proceedings SPIE 7994, 799421 (2010); doi:10.1117/12.881906

Talks and Seminars

- Seminar, Institute of Physics, University of Rostock, Germany, 1st July 2011. "Radiation Reaction Effects in Superintense Laser-Plasma Interaction".
- Invited talk (as a substitute for A. Macchi), SPIE International Symposium, 18th - 21st April 2011, Prague. "Radiation Friction Modeling in Superintense Laser-Plasma Interactions".
- Talk, DPG Conference, Kiel, Germany, 28th-31st March 2011. "Radiation Reaction Effects on Ion Acceleration in Laser-Solid Interaction".
- Seminar, LULI, École Polytechnique, Palaiseau Cedex, France, 2nd March 2011. "Radiation Reaction Effects in Laser-Plasma Interaction at Extreme Intensities".
- Talk, Fourth International Conference on Superstrong Fields in Plasmas, Varenna, Italy, 3rd-9th October 2010. "Radiation Reaction Effects on Electron Nonlinear Dynamics and Ion Acceleration in Laser-solid Interaction".

Poster contributions

- 37th EPS Conference on Plasma Physics, 21st - 25th June 2010, Dublin, Ireland. "Radiation Reaction Effects in Relativistic Laser-Produced Plasmas".

- SILMI Workshop, Frontiers in Intense Laser-Matter Interaction Theory, Garching, Germany, 1st-3rd March 2010. "A Study of Radiation Reaction Effects in Superintense Laser-Plasma Interaction".

Schools and courses

- Course on: Standard formats for scientific data (HDF5 library), CINECA supercomputing facility, Bologna, Italy, 2nd - 3rd December 2010, practice on CINECA HPC systems.
- 19th Summer School of Parallel Computing, 5-16 July 2010, CINECA, Italy. Topics: parallel architectures, models of parallel programming, parallel algorithms, programming environments, code optimization techniques, practice on CINECA HPC systems.
- 46th International School of Quantum Electronics: "Atoms and Plasmas in Super-Intense Laser Fields", 10th - 17th July 2009, Erice, Italy.

Acknowledgments

I want to thank my supervisors Dr. Andrea Macchi for the valuable advice and the many opportunities to gain experience during these three years and Prof. Francesco Pegoraro for the amusing and sometimes 'colorful' discussions.

I want to thank Dr. Tatiana Liseykina and Prof. Dieter Bauer for their friendly hospitality during my HPC-Europa2 visit.

I want to thank my parents and my grandparents for their love and support in my life.

I want to thank my beloved Piera, many things would not be possible for me without her love and her support.

Last but not least, I want to thank God for everything.